Phase formation in a nanosize silicon oxide film on the surface of aluminum oxide

V. V. Gusarov, A. A. Malkov, Zh. N. Ishutina, and A. A. Malygin

St. Petersburg State Technological Institute (Technical University)
(Submitted June 9, 1997)
Pis'ma Zh. Tekh. Fiz. **24**, 3–8 (January 12, 1998)

Phase formation has been studied in a nanosize composition of aluminum oxide and silicon dioxide. The temperature ranges for an intensive solid-phase reaction have been determined. A mechanism is proposed for phase formation in nanosize film compositions. © *1998 American Institute of Physics.* [S1063-7850(98)00101-3]

Many mechanical, electromagnetic, physicochemical, and other properties of materials undergo appreciable changes when the characteristic dimensions of objects are reduced to the nanometer scale.[1] It is therefore interesting to study synthesis processes and characteristics of phase transformations in nanosize film compositions.

Here we consider the interaction between aluminum oxide (γ-modification) and silicon dioxide. The latter was deposited on the surface of aluminum oxide particles by molecular stratification, which was first proposed in Ref. 2 and described in detail in Refs. 3 and 4. Note that in the foreign literature, following on from the work of Suntola and his group,[5,6] this method has been widely used under the term atomic layer epitaxy (ALE). In this case, as was noted by the authors of this terminology, the term ''epitaxy'' is not used in the normal concept adopted in the scientific literature, i.e., not as the term introduced by L. Royter, 1928: ''to denote the combined orientation of crystals of different types when one crystal is oriented as a function of the other crystal on which it grows.'' [7] Rather its use is based on the literal meaning of the word epitaxy, from the Greek ''epi'' meaning ''on'' and ''taxis'' meaning ''arrangement.'' In this sense the use of the term ''molecular stratification'' has undoubted advantages because of its lack of ambiguity.

The initial components were the γ modification of aluminum oxide with a specific surface area of 200 ± 5 m^2/g and a cation impurity content no higher than 0.005 wt. %, and amorphous silicon dioxide with a specific surface area of 155 ± 5 m^2 g. The thickness of the silicon oxide layers synthesized on the surface of the aluminum oxide by molecular stratification was $\sim$2 nm (the layer thickness was estimated using information on the thickness of the elemental oxide layer as a function of the number of molecular stratification cycles taken from the literature, see Refs. 8 and 9, for example). The average effective size of the γ-Al_2O_3 particles was $\sim$5 nm (calculated using data on the specific surface area of aluminum oxide).

Phase formation in these compositions was investigated in an ''isothermal annealing-quenching'' regime (highly accurate temperature control, with the fluctuations during annealing not exceeding ±5 K, was achieved by positioning the sample directly on a PR30/6 thermocouple, by using thin samples of $\sim$1 mm, and by using a high-precision VRT-2 thermocouple regulator) and under conditions of temperature rise at a constant rate (7.5 K/min). In the first case, the phase transformations in the system were recorded by quantitative x-ray phase analysis using a DRON-3.0 x-ray diffractometer and in the second case, they were recorded using the results of a differential thermal analysis (Q-1500D drift indicator, Hungary) with x-ray phase monitoring of the state of the system at points corresponding to the beginning and end of the thermal conversion effect. The results are plotted in Figs. 1 and 2.

An analysis of these results reveals the following distin-

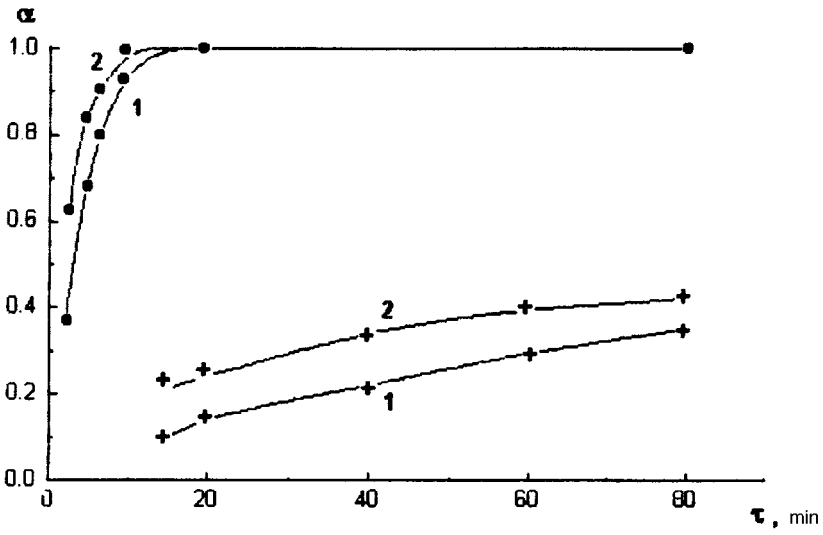

FIG. 1. Kinetics of mullite formation. Notation: α—degree of conversion, τ—time, min, *1*—$T=1573$ K, *2*—$T=1623$ K; at $T=1523$ K no traces of mullite are observed; ●—phase formation in nanosize film composition (described in text), +—phase formation in oxide mixture, given for comparison.

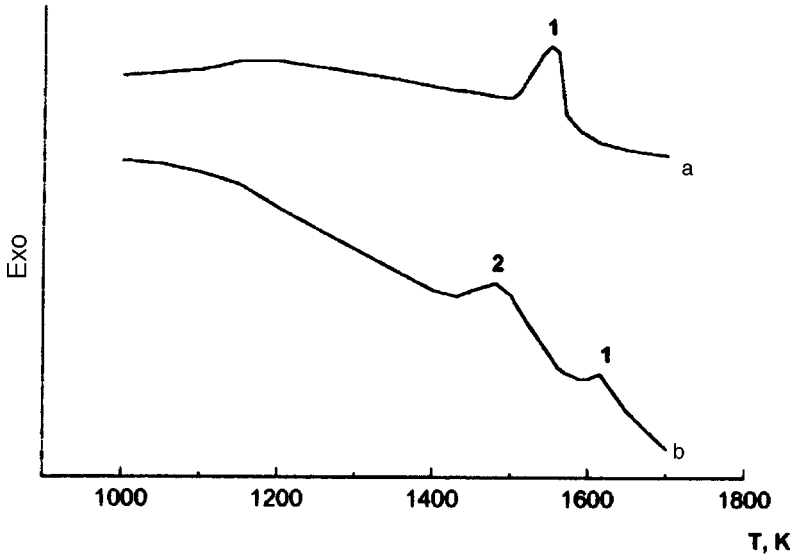

FIG. 2. Thermograms of samples. Notation: *1*—$3Al_2O_3+2SiO_2 \rightarrow Al_6Si_2O_{13}$; *2*—$\gamma$-$Al_2O_3 \rightarrow \alpha$-$Al_2O_3$; a—nanosize film composition (described in text); b—mixture of aluminum and silicon oxides given for comparison.

guishing features of the phase formation process in nanosize layers. At temperatures below a certain critical value $T_k \approx 1523$ K, almost no phase changes are observed in the system. At $T > T_k$ a chemical reaction is detected between the aluminum and silicon oxides to form mullite ($Al_6Si_2O_{13}$). The reaction takes place at a rate tens and hundreds of times higher than the rates typical of solid-phase chemical reactions (Fig. 1), although the range of temperatures studied is substantially lower than the melting point of the contacting phases and the eutectic temperature. However, it should be noted that there is a good correlation between T_k and the melting point of the two-dimensional nonautonomous phase ($T_{m2n} \approx 1500-1550$ K (Ref. 10)). Here we use the terminology adopted in the classical thermodynamic studies of Defay, Prigogine, and Rusanov[11–13] whereby bulk phases are taken to be autonomous and phases formed in the contact zone between the solid regions of the bulk phases, particularly surface phases, are taken to be nonautonomous.

Another characteristic feature of the phase formation in this composition is that the kinetics of the process does not exhibit any appreciable temperature dependence for $T > T_k$ (Fig. 1). This behavior is evidenced by the extremely low activation energies, which are also not typical of solid-phase reactions[14] and are generally observed when reagents interact in the liquid phase in the presence of nucleating centers.[15]

These results suggest that the following mechanism may be responsible for phase formation in a nanosize film composition. Interaction between the components in the system is only activated after melting of the two-dimensional nonautonomous phase, $T > T_{m2n}$, formed by contact between the autonomous phases of the reagents. Since the equilibrium thickness of the liquid two-dimensional nonautonomous phase at $T \approx T_{m2n}$ is comparable with the thickness of the reagent layer in the nanosize film composition (see Refs. 10 and 16, for example), it is substantially easier for reagents to be transported to the reaction zone (the diffusion coefficient in the liquid phase is generally four orders of magnitude higher than that in the solid phase of the same composition[17]). Note that in this sense, being a solid-phase process in terms of the classification characteristics:[14] the reagents and products are solids, such a chemical reaction in a nanosize system may be considered to be liquid-phase to a certain extent.

CONCLUSIONS

As a result of the presence of nucleating centers (γ-Al_2O_3 is the closest structural analog of mullite[7]), the relatively high transport velocity ($T > T_{m2n}$), and the short path length of the reagents in the reaction zone (~ 1 nm), the rate of the relaxation process in this nanosize composition is one or two orders of magnitude higher than that for a solid-phase reaction in a similar mixed composition.

This work was supported by the Russian Fund for Fundamental Research, Grant No. 96-01-00074.

[1] R. Birringer and H. Gleiter, in *Encyclopedia of Materials Science and Engineering*, Vol. 1 (Pergamon Press, Oxford, 1988), p. 3339.
[2] S. I. Kol'tsov, Abstracts of Papers presented at Scientific-Technical Conference [in Russian], Goskhimizdat, Leningrad (1963).
[3] S. I. Kol'tsov, Zh. Prikl. Khim. **42**, 1023 (1969).
[4] A. A. Malygin, A. A. Malkov, and S. D. Dubrovenskii, in *Adsorption on New and Modified Inorganic Sorbents*, Vol. 99, edited by A. Dabrowski and V. A. Tertykh (Elsevier, Amsterdam, 1996), p. 213.
[5] T. Suntola and J. Antson, U.S. Patent No. 4,058,430 (1977).
[6] *Atomic Layer Epitaxy*, edited by T. Suntola and M. Simpson (Blackie, Glasgow, 1990).
[7] *Encyclopedia of Earth Sciences*, Vol. IV B. *The Encyclopedia of Mineralogy*, edited by K. Frye (Hutchinson Rose, Stroudsberg, PA, 1981).
[8] V. V. Fromov, *Introduction to Ellipsometry* [in Russian], Leningrad University Press, Leningrad (1986), p. 163.
[9] S. B. Desu, Mater. Sci. Eng. B **13**, 299 (1992).
[10] V. V. Gusarov and I. Yu. Popov, Nuovo Cimento D **18**, 799 (1996).
[11] R. Defay, *Étude Thermodinamique de la Tension Superficielle* (Gauntier-Vellarg, Paris, 1934).
[12] R. Defay and I. Prigogine, *Tension Superficielle et Adsorption* (Editions Desoer, Liege, 1951).
[13] A. I. Rusanov, *Phase Equilibria and Surface Phenomena* [in Russian], Khimiya, Leningrad (1967).

[14] Yu. D. Tret'yakov, *Solid-Phase Reactions* [in Russian], Khimiya,Moscow (1978).
[15] M. Vollmer, *Kinetik der Phasenbildung* (Steinkopff, Dresden, 1939; Nauka, Moscow, 1986).
[16] J. G. Dash, Contemp. Phys. **30**, 89 (1989).
[17] I. Kaur and W. Gust, *Fundamentals of Grain and Interphase Boundary Diffusion* (Ziegler Press, Stuttgart, 1989), p. 324.

Translated by R. M. Durham

Electron-stimulated condensation of carbon dioxide at a electronegative impurity

E. M. Abornev, V. P. Zhukovskaya, O. A. Nerushev, S. A. Novopashin, A. L. Perepelkin, and V. V. Radchenko

Institute of Heat Physics, Siberian Branch of the Russian Academy of Sciences, Novosibirsk
(Submitted July 31, 1997)
Pis'ma Zh. Tekh. Fiz. **24**, 21–25 (January 12, 1998)

An experimental investigation has been made of the influence of electrons and electronegative impurities on the condensation process observed when CO_2, whose molecules possess no electron affinity, expands into a vacuum.
[S1063-7850(98)00401-7]

Adiabatic cooling accompanying the free expansion of a gas into a vacuum leads to cooling of this gas below the saturation temperature. However, the formation of a condensed phase (clusters) in the stream may not be observed if the number of collisions following the establishment of saturation conditions is insufficient for the formation of critical-size clusters. The limiting stage for homogeneous condensation is the formation of small clusters.[1] The artificial introduction of nuclei into the stream may produce a condensation process under conditions where no homogeneous condensation occurs. These condensation nuclei may be charged particles (condensation at charges was first observed by Wilson[2]). From the thermodynamics point of view,[3] this phenomenon occurs because the free energy of a charged cluster has a minimum for a certain size. For saturation conditions, the radius of an equilibrium cluster with charge e is:

$$r=\{(e/16\pi\alpha)(\epsilon-1)/\epsilon\}^{1/3}, \quad (1)$$

where ϵ is the permittivity of the condensed phase and α is the surface tension. Condensation accompanying the expansion of a stream to which free charges had been added was observed at ions formed as a result of the positive energy of affinity between neutrals and charged particles: the proton affinity of water molecules,[4,5] and the electron affinity of chlorine atoms.[6] An estimate of the equilibrium CO_2 cluster using formula (1) gives a value of the order of 10^2 molecules.

Here we study the influence of electrons and electronegative impurities on the condensation process observed when CO_2, whose molecules possess no electron affinity,[7] expand into a vacuum. The experiments were carried out using a low-pressure gasdynamic system. Inside the vacuum chamber a gas source—an acoustic nozzle (2 mm diameter) with a thermally stabilized forechamber—was located on a three-axis stage. The flow parameters were determined by measuring the pressure and temperature in the forechamber. The gas temperature in the forechamber was monitored with a thermocouple and was 295 K in all the experiments described below. A thermionic electron emission source was located in the nozzle forechamber to generate charged clusters. The electron emitter was a lanthanum hexaboride pellet. Under operating conditions the emitter is heated by passing a current through a tungsten filament clamped to it. The temperature of the pellet was varied between room temperature and 800 K. Thermal decoupling from a molybdenum thin-walled holder, a ceramic insert, and additional liquid nitrogen cool-

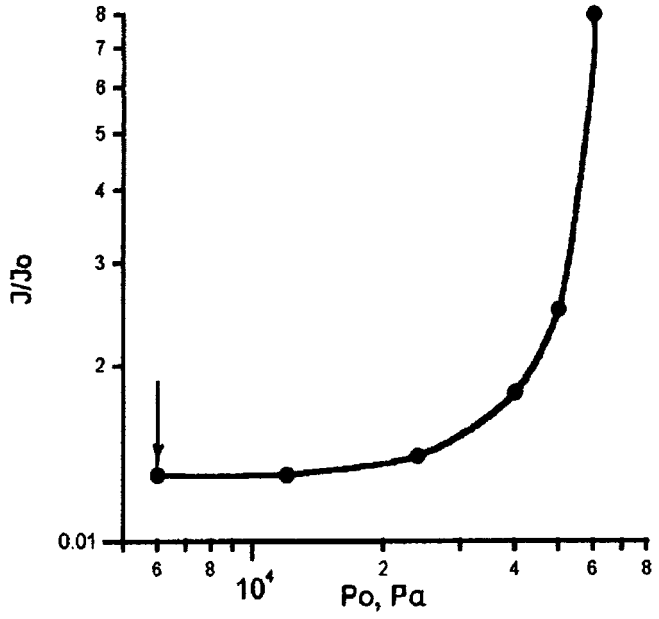

FIG. 1. Intensity of scattered light versus initial pressure.

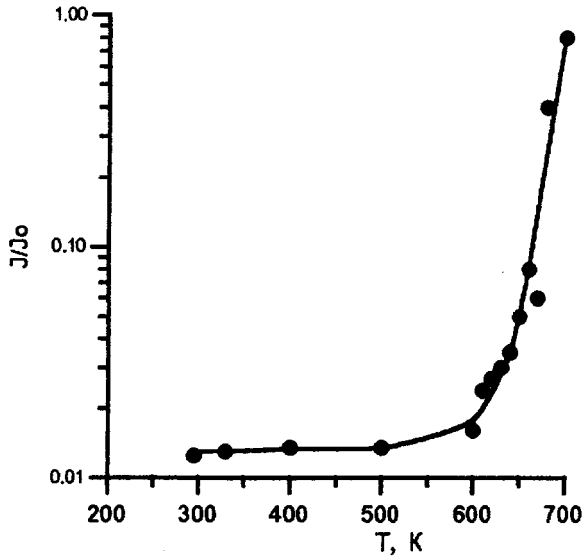

FIG. 2. Intensity of scattered light versus temperature of electron emitter.

ing of the gas in the forechamber were used to achieve thermal conditions. A method based on Rayleigh light scattering was used for diagnostics.[8,9] The scattered radiation intensity J for a condensed-phase stream is given by:

$$J = AI_0 \sum N_i i^2, \tag{2}$$

where I_0 is the intensity of the reference radiation, N_i is the concentration of clusters containing i molecules, and A is a geometric factor which is determined from calibration experiments using a gas of known concentration.

Figure 1 gives the scattered light intensity as a function of the initial pressure. The measurements were made on the axis of the stream 6 mm from the exit cross section. The intensity was normalized to the scattering intensity J_0 corresponding to the gas concentration in the nozzle forechamber. The horizontal section corresponds to expansion of the gas without condensation, while the increase in signal indicates the formation of clusters in the stream. The introduction of free electrons when the lanthanum hexaboride pellet was heated to the maximum emitter temperature did not lead to any significant change in the dependence plotted in Fig. 1. This result indicates that negative CO_2 cluster ions do not form under these experimental conditions, evidently because the CO_2 molecules do not possess electron affinity. An electronegative impurity gas was introduced into the nozzle forechamber in order to observe charge-stimulated condensation of CO_2. For this purpose, F-4 Teflon was placed near the heater element, which resulted in the formation of gas-phase electronegative fluorine and fluorocarbon radicals. Figure 2 gives the experimental dependence of the light scattering in the stream as a function of the pellet temperature. The measurements were made at the same distance from the nozzle edge as for the data plotted in Fig. 1. The pressure in the forechamber is 6×10^3 Pa. Under these conditions, no homogeneous condensation is observed (this pressure is indicated by the arrow in Fig. 1). As the temperature increases above 600 K, the intensity of the scattered signal increases by two orders of magnitude. Control experiments in which the lanthanum hexaboride pellet was replaced with copper indicated that the observed stimulated condensation effect is caused by the presence of both electrons and electronegative impurities.

To sum up, two main results have been obtained.

1. The introduction of free electrons in the forechamber does not influence the condensation of CO_2 as it expands in a supersonic stream.

2. Electron-stimulated condensation of CO_2 is observed at electronegative impurities.

To conclude, we note that charge-stimulated processes can be used to obtain cluster streams with a narrow size distribution function which is important for studying the properties of clusters of a particular size and also for various technological applications.

This work was partially financed by the Russian Fund for Fundamental Research, Grant No. 96-02-19045.

[1] D. Colomb, R. E. Good, A. B. Balley *et al.*, J. Chem. Phys. **57**, 3844 (1972).
[2] C. T. R. Wilson, Philos. Trans. R. Soc. London, Ser. A **189**, 265 (1897).
[3] Yu. V. Rumer and M. Sh. Ryvkin, *Thermodynamics, Statistical Physics, and Kinetics* [in Russian], Nauka, Moscow (1977).
[4] J. Q. Searcy and J. B. Fenn, J. Chem. Phys. **61**, 5282 (1974).
[5] R. J. Benhler and L. Friedman, J. Chem. Phys. **77**, 2549 (1982).
[6] H. Haberland, H. Langosch, H.-G. Schindler, and D. R. Worsnop, *Book of Abstracts of the Sixth International Symposium on Molecular Beams*, Freiburg, 1983, pp. 123–125.
[7] B. M. Smirnov, *Complex Ions* [in Russian], Nauka, Moscow (1983).
[8] S. A. Novopashin, A. L. Perepelkin, and V. N. Yarygin, Prib. Tekh. Eksp. No. **5**, 158 (1986).
[9] E. M. Abornev, O. A. Nerushev, S. A. Novopashin *et al.*, Pis'ma Zh. Tekh. Fiz. **22**(21), 84 (1996) [Tech. Phys. Lett. **22**, 900 (1996)].

Translated by R. M. Durham

Direct observation of a plastic deformation autowave in a zirconium alloy

V. I. Danilov, S. Yu. Zavodchikov, S. A. Barannikova, I. Yu. Zykov, and L. B. Zuev

Institute of Physics of Strength of Materials and Materials Science, Siberian Branch of the Russian Academy of Sciences, Tomsk

(Submitted June 2, 1997)
Pis'ma Zh. Tekh. Fiz. **24**, 26–30 (January 12, 1998)

An analysis is made of the evolution of local deformations during the elongation of samples of fine-grained zirconium alloy. It is established that the deformation distribution patterns exhibit ordered behavior where the types of ordering are closely related to the stages of the deformation curve. The results are compared with similar data from studies of the deformation fields of single-crystal and polycrystalline materials with different types of crystal structures and deformation micromechanisms. It is noted that all these similar results, including those of the present study, may be interpreted using autowave representations. © *1998 American Institute of Physics.* [S1063-7850(98)00501-1]

The localization of plastic deformation is a serious problem which can only be solved by a comprehensive analysis of the physics of the process. The view has long been held that localization is the final stage of the deformation process and at the initial stages the plastic flow evolves as a macroscopically uniform process. Current thinking, that macroscopic localization of deformation begins to be observed from the yield point onward and exists in some form at all stages of flow, has evolved from specific studies of macrolocalization using increasingly accurate methods. For instance, generalizing the results of studies of single crystals and polycrystals of metals and alloys,[1–5] made using speckle interferometry, has revealed the existence of three types of deformation localization characteristics, which correspond to quite specific stages of plastic deformation. It was found that the area of fluidity corresponds to the propagation of a solitary localized deformation front, the linear hardening stage corresponds to a traveling deformation wave, and the parabolic hardening stage corresponds to a steady-state system of localized flow zones. All these characteristics were interpreted in Refs. 2 and 3 as different variants of autowave processes, by analogy with those well-studied for other types of systems, as in Ref. 6, for example. The evolution of the distribution patterns of local deformations has been studied most comprehensively for single-crystal samples. A traveling plastic deformation autowave was observed in single crystals of a Cu–10% Ni–6% Sn copper-nickel alloy[3,5] and in Kh18N12AM2 austenitic steel containing more than 0.35% nitrogen.[7] Such a comprehensive range of macrolocalization patterns has not been obtained for polycrystalline materials although specific types of characteristic distributions have been identified.[1]

We studied the polycrystalline alloy Zr–1.3% Sn–1% Nb–0.4% Fe designed for the fabrication of fuel element tubes for nuclear reactors. At room temperature this alloy is a solid solution of hexagonal close-packed α-zirconium containing a small amount (less than 1 wt. %) of intermetallides and oxides. The grain size of the matrix and the inclusions was around 5 μm and <0.3 μm, respectively. Samples having a working section of $40\times6\times2$ mm, cut from a tubular

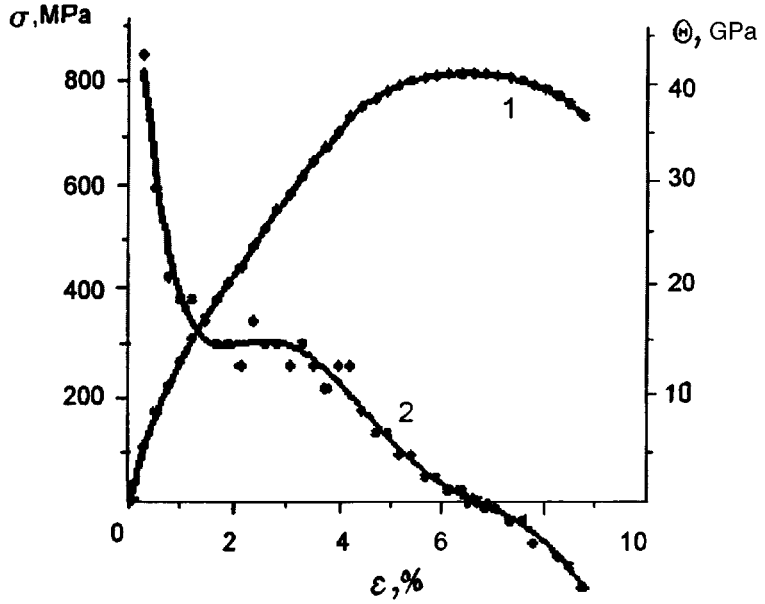

FIG. 1. Stress-strain diagram (*1*) and hardening coefficient versus strain (*2*) for elongation of zirconium alloy.

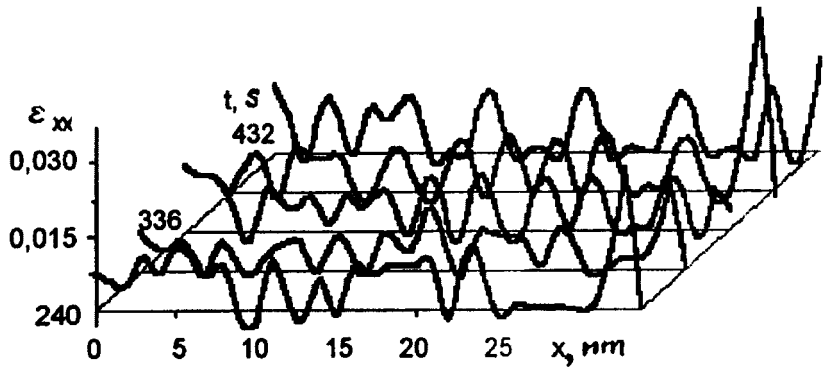

FIG. 2. Space-time distribution of local elongations at the linear deformation stage of a zirconium alloy.

blank, were elongated using an Instron-1185 testing machine at a rate of 3.5×10^{-5} s^{-1} at 300 K. Speckle interferometry[1] was used to record the fields of the displacement vectors from the yield point as far as rupture at 50 s intervals (at intervals of 0.2% total strain). Numerical differentiation with respect to the coordinates was then used to calculate the distributions of the longitudinal, transverse, shear, and rotational components of the plastic distortion tensor for all points on the observable surface of the sample.

Figure 1 gives the deformation curve $\sigma(\varepsilon)$ of this alloy and its deformation hardening coefficient $d\sigma/d\varepsilon=\theta(\varepsilon)$ as a function of increasing deformation. An analysis of the curve $\theta(\varepsilon)$ reveals a linear hardening stage ($\theta=$const) for integrated strains in the range 1.6–2.8%.

The distribution of the components of the distortion tensor (the local elongation ε_{xx} is shown and the other components behave similarly) at this deformation stage is shown in Fig. 2. Six or seven equidistant local elongation peaks can be identified. The spatial period (wavelength) of the process shown in Fig. 2, $\lambda\approx5.5\pm1$ mm, did not vary over the entire linear hardening stage. The set of localized deformation maxima moved synchronously along the sample at a constant velocity $\nu\approx3.5\times10^{-5}$ m/s. These data show that, under these conditions, the plastic deformation is a wave process with the period $\tau=\lambda/\nu\approx1/6\times10^{2}$ s.

A further increase in deformation destroyed the regularity of the observed pattern. Following the transition to parabolic hardening, the sample exhibited three broad steady-state zones of deformation localization. Then, immediately before rupture, a fixed local maximum of ε_{xx} was formed. Its position precisely indicated the point at which a stable macroscopic neck preceding the viscous rupture of the sample subsequently appeared and evolved. This evolution of the distributions of the plastic distortion tensor components is fairly universal and can frequently by identified in many materials.[1–5]

The observed plastic deformation fronts are inclined at the angle $\alpha\approx\pi/4$ to the elongation axis of the sample, which is clearly determined by the orientation of the areas of maximum tangential stresses under elongation, similar to the Chernov–Lüders band.[8] It can be seen that for a sample of width $d=6$ mm and distributions with the spatial period $\lambda\approx5.5\pm1$ mm, as for a Cu-based alloy,[5] the geometric condition $\lambda=d/\tan\alpha$ is satisfied. However, it is important to note that in Ref. 5 the position of the plastic flow fronts was defined by the maximum Schmidt factor for glide planes oriented differently relative to the axis of elongation of the single-crystal samples.

Thus, these results confirm our previous conclusions that the types of local deformation distributions observed during loading of materials and the evolution of these distributions do not depend directly on the size of the objects and their internal structure but are determined by the behavior of the coefficient of deformation hardening as the overall deformation level increases.[2] In addition to the external similarity between the effects, it is significant that the wavelength $\lambda\approx5.5\pm1$ mm observed for a Zr alloy is similar to those identified in single crystals of Cu-based alloy[5] and in austenitic steel.[7] This behavior suggests that the deformation localization parameters are not determined directly by processes which take place very differently at the microscopic (dislocation) level in single crystals and polycrystals,[8] but are governed by the larger-scale (mesoscopic)[9] characteristics of the plastic flow. It may be asserted that regardless of whether the material is single-crystal or polycrystalline, the same stages of the $\sigma(\varepsilon)$ diagram correspond to the same types of fields of the distortion tensor components, which provides further confirmation that these phenomena[3] may be correctly assigned to a fairly universal class of autowave processes.

[1] K. V. Frolov, V. E. Panin, L. B. Zuev *et al.*, Izv. Vyssh. Uchebn. Zaved. Fiz. No. **2**, 19 (1990).
[2] V. I. Danilov, Author's Abstract of Doctoral Thesis [in Russian], Institute of Physics of Strength of Materials and Materials Science, Siberian Branch of the Russian Academy of Sciences, Tomsk (1995).
[3] L. B. Zuev, V. I. Danilov, and V. V. Gorbatenko, Zh. Tekh. Fiz. **65**(5), 91 (1995) [Tech. Phys. **40**, 456 (1995)].
[4] L. B. Zuev, N. V. Kartashova, V. I. Danilov *et al.*, Zh. Tekh. Fiz. **66**(11), 190 (1996) [Tech. Phys. **41**, 1189 (1996)].
[5] V. I. Danilov, N. V. Kartashova, L. B. Zuev *et al.*, Fiz. Met. Metalloved. **78**, 141 (1994).
[6] V. A. Vasil'ev, Yu. M. Romanovskiĭ, and V. G. Yakhno, *Autowave Processes* [in Russian], Nauka, Moscow (1987).
[7] L. B. Zuev, V. I. Danilov, and S. A. Barannikova, *Proceedings of the Conference on Nitrogen Steels*, Gliwice, Poland, 1966, p. 293.
[8] D. McLean, *Mechanical Properties of Metals* [Russ. transl., Metallurgiya, Moscow, 1965].
[9] *Physical Mesomechanics and Computer-Aided Design of Materials*, edited by V. E. Panin [in Russian], Nauka, Novosibirsk (1995).

Translated by R. M. Durham

Modeling of explosive acoustic emission accompanying martensitic transformations in alloys

V. A. Plotnikov

Altaĭ State University, Barnaul
(Submitted July 17, 1997)
Pis'ma Zh. Tekh. Fiz. **24**, 31–38 (January 12, 1998)

The acoustic emission accompanying the stimulation of macroexplosive martensitic transformation kinetics in Ti–51.0 at. % Ni alloy has been confirmed. The macroexplosive kinetics were stimulated both by repeated cycling and by incomplete quasicycling of martensitic transformations. © *1998 American Institute of Physics.* [S1063-7850(98)00601-6]

1. The asymmetry of the acoustic emission accompanying martensitic transformations in Ti–51.0 at. % Ni alloy, compared with other Ti-Ni alloys with a lower nickel content, may be described as anomalous.[1] This asymmetry is anomalous because the acoustic emission intensity for the reverse martensitic transformation is much higher (two orders of magnitude) than that for the direct transformation. This type of asymmetry is characteristic of Au–Cd, Cu–Al–Ni, and other alloys.[2] In our previous studies we have shown that in alloys susceptible to phase hardening, the emission energy for the direct transformation is substantially higher than that for the reverse process and the main mechanism responsible for the production of acoustic emission involves the plastic relaxation of stresses generated during the motion of the interphase boundary.[1,3] The emission mechanism has not been clarified for alloys in which no phase hardening takes place and the kinetics of the martensitic transformation involves slow growth and contraction of the martensitic crystal. The emission mechanism for the reverse transformation is not fully understood. To solve this problem, we produced special experimental scenarios which can accurately reproduce the dynamic mechanism of acoustic emission.

2. The experimental results obtained by recording the acoustic emission over a complete martensitic transformation cycle (a direct transformation during cooling and a reverse transformation during heating) are plotted in Fig. 1 in the form of acoustic curves giving the acoustic emission intensity as a function of the process time. Also plotted are the heating and cooling curves which can be used to correlate the emission interval with the temperature interval.

Figure 1a shows a typical acoustic curve characterizing a martensitic transformation in Ti–51.0 at. %Ni alloy after repeated cycling. The curve is highly asymmetric: the emission energy for the reverse transformation is much higher than that for the direct process.

The implementation of an incomplete (nested) quasicycle of martensitic transformation involving incomplete heating, i.e., where the reverse martensitic transformation does not go to completion, reverses the asymmetry of the emission. This is indicated by the curve plotted in Fig. 1b which shows that cooling beyond the incomplete quasicycle leads to emission in the direct martensitic transformation whose energy is substantially higher than that for the reverse transformation. A subsequent complete cycle of martensitic transformation restores the initial asymmetry of the emission (Fig. 1b).

3. In a Ti–51.0 at. %Ni alloy a thermoelastic reversible martensitic transformation takes place at a temperature between -100 °C and $+20$ °C (Ref. 4). When the alloy is cooled to $+20$ °C, a $B2 \rightarrow R \rightarrow B19'$ direct martensitic transformation takes place: the temperature for formation of the rhombohedral R phase is $T_R = -25$ °C, and the critical $R \rightarrow B19'$ transformation temperatures are $M_s = -55$ °C and $M_f = -90$ °C. Heating between -50 °C and room temperature is accompanied by a $B19' \rightarrow R \rightarrow B2$ reverse martensitic transformation.

Unlike other Ti–Ni alloys, in Ti–51.0 at. %Ni alloy the temperature ranges for the existence of the rhombohedral phase R and the monoclinic $B19'$ phases are separate. The $B2 \rightarrow R$ transformation is similar to a second-order phase transition and, in accordance with Refs. 5 and 6, is caused by reduced stability of the {110} atomic planes to shift in the ⟨100⟩ direction and localized superpositions of atomic displacements such as {110} ⟨110⟩ and {112} ⟨111⟩.

Aging strongly influence the martensitic transformation characteristics in nonstoichiometric Ti–Ni alloys.[7,8] Holding the 51.0 at. % Ni alloy briefly at 523 and 773 K changes the transformation sequence: whereas after quenching from 1073 K, the sequence is $B2 \rightarrow B19'$, after aging this becomes $B2 \rightarrow R$ or $B2 \rightarrow R \rightarrow R + B19' \rightarrow B19'$. Data obtained by electron microscopy and x-ray structural analysis indicate that this behavior is caused by the formation of nickel-enriched concentration inhomogeneities and by localized precipitation of the Ti_3Ni_4 phase.

4. The explosive acoustic emission accompanying a martensitic transformation in Ti–51.0 at. % Ni alloy was modeled in two ways: 1) by repeated cycling of the martensitic transformation; 2) by replacing complete cycling of the martensitic transformation with incomplete quasicycling.

By analogy with the explosive kinetics of a direct martensitic transformation, for a nested quasicycle,[9] we shall describe the ''provoked'' acoustic emission as explosive. That is to say the situation shown in Fig. 1b is caused by a change of the cycling regime and by the appearance of an explosive section on the kinetic curve on transition from incomplete (nested) quasicycling to complete cycling. A diagram (martensitic curve) of these cycles constructed using x-ray data is shown in Fig. 2a.

The appearance of a macroexplosive section on the ki-

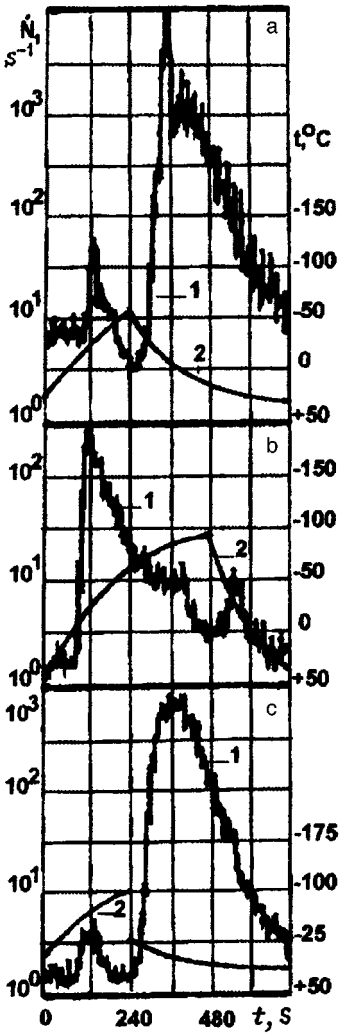

FIG. 1. Fragments of acoustic curves (*1*) obtained for different martensitic transformation scenarios: a—after repeated cycles of martensitic transformation; b—after an incomplete quasicycle of martensitic transformation; c—in the next complete cycle of martensitic transformation after an incomplete quasicycle. Temperature curve (*2*).

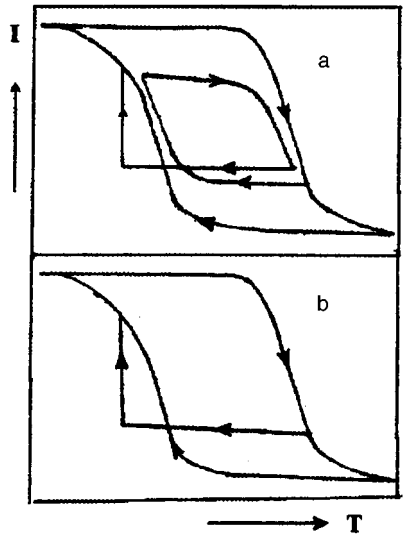

FIG. 2. Diagram of incomplete quasicycles of martensitic transformation (a) and diagram showing experimental situation with an incomplete quasicycle to model explosive acoustic emission (b). Here I is the x-ray line intensity and T is the temperature.

netic (Fig. 2a) curve is deduced from the quasiequilibrium description of the martensitic transformation and the thermodynamic analysis of acoustic emission.[9,10]

The condition for the quasiequilibrium state has the form

$$g(T,Y)=g_{\mathrm{ch}}(T)+g_{\mathrm{nch}}(T,Y), \tag{1}$$

where $g_{\mathrm{ch}}(T)=-(\partial f_{\mathrm{ch}}/\partial Y)$ and $g_{\mathrm{nch}}(T,Y)=-(\partial f_{\mathrm{nch}}/\partial Y)$ are the chemical and nonchemical contributions to the driving force of the martensitic transformation $g(T,Y)$, T and Y are the temperature and fraction of the martensitic phase, respectively. On the graph of g_{ch}, $(-g_{\mathrm{nch}})$ versus Y, this equation uniquely describes a quasiequilibrium-state line, consisting of stable sections where the condition $g_{\mathrm{ch}}+g_{\mathrm{nch}}=0$ is satisfied, and unstable sections corresponding to above-barrier microexplosions of the athermal martensitic transformation process, where the condition $g_{\mathrm{ch}}+g_{\mathrm{nch}}=g_D$ is satisfied. Here g_D is the dissipative contribution to the quasiequilibrium state equation (the equation of balance of the driving forces). Changing the cycling regime leads to the appearance of nonmonotonicity on the curve $f_{\mathrm{nch}}(Y)$ of the Gibbs molar potential, and discontinuity of the first derivative. The jump in $g_{\mathrm{nch}}(Y)$ at the instant when the cycling regime changes is equal to g_D within experimental error or more accurately, to the increment g_D of the acoustic contribution.[10]

5. In our experiments, when the reverse martensitic transformation is not completed as shown in Fig. 2b, a substantial amount of the nonchemical (mainly elastic) energy accumulated in the previous direct transformation is stored in the structure of the alloy. Thus, the direct transformation following an incomplete reverse transformation takes place in a matrix with a higher level of internal stresses, causing the microkinetics of slow growth of the martensitic crystal to be replaced by a microexplosive process already accompanied by induced explosive acoustic emission.

This conclusion agrees with other data. It has been shown that under the application of an external load, the kinetics of both direct and reverse martensitic transformations resemble an explosive process.[11] Moreover, when the external stress is removed, the martensitic transformation cycles are accompanied by a spontaneous return of deformation[12] which is caused by changes in the kinetics of the reverse martensitic transformation under the action of an orienting stress and by conservation of the conditions for the formation of orienting internal stresses in the absence of external stress.

Internal stresses appear when self-accommodating groups of martensitic crystals are formed. The last plate in an ensemble of crystals accumulates the highest possible elastic stresses. This last plate is the first to disappear when the sign of the external action is reversed,[13] which suggests that the elastic energy accumulated in the course of a direct martensitic transformation contributes to the driving force of the reverse martensitic transformation. At the same time, the first martensitic plate will be the last to disappear under condi-

tions of minimum (or even zero) elastic energy at temperature A_f (Ref. 14).

During martensitic transformation cycles in nonstoichiometric alloys orienting internal stresses may be produced as a result of the formation of concentration inhomogeneities and particles of a different phase. This situation is particularly typical of the Ti–51.0 at. % Ni alloy in which a martensitic transformation is accompanied by a high reaction energy, which may increase the local diffusion mobility of the atoms. The first martensitic transformation cycle promotes the formation of a spatial inhomogeneity configuration and subsequent cycles merely intensify this effect. In addition, the trajectory of the next martensitic transformation cycle must repeat the previous one. Thus, the transition of the system to a state with an explosive reverse martensitic transformation is a natural consequence of the evolution of the structure.

Under the action of orienting internal stresses, the appearance and particularly the disappearance of martensitic crystals will obey microexplosive kinetics. The experimentally observed motion of the interphase boundary in Cu–Al–Ni alloys is close to explosive (in the form of the propagation of the Lüders band). The return motion of the interphase boundary under these conditions is more explosive[15] since a preferentially oriented martensitic structure forms under the action of the external stress, resulting in the buildup of internal stresses and return motion of the boundary under the action of these stresses.

6. It has been shown that the structure of the acoustic curve for the reverse martensitic transformation in the form of two intensity peaks with well-defined asymmetry in favor of the reverse transformation is consistent with a two-stage reverse martensitic transformation process $B19' \rightarrow R$ and $R \rightarrow B2$ and with microexplosive kinetics for disappearance of the martensitic crystal, i.e., the $B19' \rightarrow R$ and $R \rightarrow B2$ transformations are accompanied by induced explosive acoustic emission.

The restoration of the initial asymmetry of the acoustic emission in the martensitic transformation cycle immediately following the incomplete quasicycle (Fig. 1b) indicates that the elastic energy plays a major role in the driving force for the martensitic transformation. Elastic energy of any type acts as a parameter of state influencing the phase equilibrium,[10] i.e., an excess nonchemical driving force in relation to the chemical driving force changes the microkinetics of the martensitic transformation to microexplosive.

The existence of explosive emission kinetics and its dependence on the incomplete quasicycles indicates that both the $B19' \rightarrow R$ and the $R \rightarrow B2$ and $B2 \rightarrow R$ and $R \rightarrow B19'$ transformations exhibit microexplosive kinetics. It should be noted that the microkinetics must be understood not only as the spontaneous formation of a martensitic crystal of finite size but also as a sequence of spontaneous displacements (jumps) of the interphase boundary. The only difference is in the scale of the jumps.

To conclude, in alloys not susceptible to phase hardening, of which Ti–51.0 at. % Ni is one, a martensitic transformation is accompanied by explosive acoustic emission which indicates that the appearance and disappearance of the martensitic crystals obeys microexplosive kinetics. The macroscopic kinetic effect consists in the spontaneous and correlated formation of numerous martensitic crystals. The mechanism for the formation of emission caused by this kinetics will be described as dynamic. Acoustic emission during heating is produced for both $B19' \rightarrow R$ and $R \rightarrow B2$ transformations. A change in the cycling regime and cooling beyond the limit of an incomplete quasicycle leads to a single explosive acoustic emission process during a direct martensitic transformation.

[1] V. A. Plotnikov, L. A. Monasevich, V. É. Gyunter, and Yu. I. Paskal', Dokl. Akad. Nauk SSSR **290**, 110 (1986) [Sov. Phys. Dokl. **31**, 755 (1986)].
[2] J. Barom and M. Rosen, Acta Metall. **30**, 655 (1982).
[3] V. A. Plotnikov, L. A. Monasevich, and Yu. I. Paskal', Fiz. Met. Metalloved. **61**, 769 (1986).
[4] B. D. Chernov, Yu. I. Paskal', V. É. Gyunter, L. A. Monasevich, and E. M. Savitskiĭ, Dokl. Akad. Nauk SSSR **247**, 854 (1979) [Sov. Phys. Dokl. **24**, 664 (1979)].
[5] V. G. Pushin, V. V. Kondrat'ev, and V. N. Khanin, Izv. Vyssh. Uchebn. Zaved. Fiz. **5**, 5 (1985).
[6] R. J. Wasilewski, Trans. Metall. Soc. AIME **223**, 1691 (1965).
[7] A, I, Lotkov and V. N. Grishkov, Izv. Vyssh. Uchebn. Zaved. Fiz. **5**, 68 (1985).
[8] V. I. Zel'dovich, V. G. Pushin, V. N. Khanin *et al.*, Proceedings of the All-Union Conference on Martensitic Transformations in Solids, Kiev, 1982 [in Russian], pp. 330–333.
[9] Yu. I. Paskal' and L. A. Monasevich, Deposited paper No. 1667–80 [in Russian], VINITI (1981).
[10] Yu. I. Paskal', V. A. Plotnikov, and L. A. Monasevich, Deposited paper No. 5161–V89 [in Russian], VINITI (1989).
[11] Yu. I. Paskal', V. Ya. Erofeev, and L. A. Monasevich, Metallofizika **6**(6), 36 (1984).
[12] S. L. Kuz'min, V. A. Likhachev, S. R. Shimanskiĭ, and A. I. Chernyshenko, Fiz. Met. Metalloved. **57**, 612 (1984).
[13] D. Perkins *et al.*, in *Shape-Memory Effects in Alloys, Proceedings of the International Symposium, Toronto*, edited by J. Perkins (Plenum Press, New York, 1975; Metallurgiya, Moscow, 1979).
[14] V. Owen, in *Shape-Memory Effects in Alloys, Proceedings of the International Symposium, Toronto*, edited by J. Perkins (Plenum Press, New York, 1975; Metallurgiya, Moscow, 1979).
[15] K. Shimuzu and K. Otsuka, in *Shape-Memory Effects in Alloys, Proceedings of the International Symposium, Toronto*, edited by J. Perkins (Plenum Press, New York, 1975; Metallurgiya, Moscow, 1979).

Translated by R. M. Durham

Theoretical description of high-temperature implantation of silicon carbide with N^+ and Al^+ ions

D. V. Kulikov, Yu. V. Trushin, R. A. Yankov, J. Pezoldt, and W. Skorupa

A. F. Ioffe Physicotechnical Institute, Russian Academy of Sciences, St. Petersburg; Rossendorf Research Center, Dresden, Germany; Ilmenau Technical University, Ilmenau, Germany
(Submitted August 28, 1997)
Pis'ma Zh. Tekh. Fiz. **24**, 39–43 (January 12, 1998)

A theoretical analysis is made of the evolution of the defect structure in silicon carbide (6H–SiC) implanted with N^+ and Al^+ ions of various energies. Satisfactory agreement was achieved between the calculated defect distributions and the experimental data. The following kinetic parameters of silicon carbide were estimated numerically: the migration energy of interstitial silicon atoms and the recombination parameters of vacancies and interstitial sites in the carbon and silicon subsystems. © *1998 American Institute of Physics.*
[S1063-7850(98)00701-0]

The quasibinary system $(SiC)_{1-x}(AlN)_x$ is of considerable interest for the development of optoelectronic and high-temperature devices and is currently perhaps the most promising material for these applications. One method of preparing this solid solution involves ion implantation of silicon carbide. In Ref. 1 we reported experimental investigations of the structure of $(SiC)_{1-x}(AlN)_x$ samples obtained by ion beam synthesis. Each sample was bombarded by ions in the following sequence: first by 65 keV nitrogen ions at a dose of 5×10^{16} cm^{-2}, then by 120 keV nitrogen ions at 1.3×10^{17} cm^{-2}. This was followed by 100 keV aluminum ions at a dose of 5×10^{16} cm^{-2} and 160 keV aluminum ions at 1.3×10^{17} cm^{-2}. The substrate temperature was 200, 400, 600, and 800 °C, respectively. After implantation the samples were investigated by Rutherford backscattering spectroscopy with channeling (RBS/C) using a 1.4 meV He^+ ion beam, and the RBS spectra were processed using a specially developed computer program capable of giving the depth distribution of the structural defects (see Refs. 2 and 3). The TRIRS and DYTRIRS codes[4–6] were used to calculate the ballistic distributions of the implanted ions and defects. The ballistic distributions of the N^+ and Al^+ (DYTRIRS) (see curve labeled ''ions N^+ and Al^+'' in Fig. 1 and Fig. 1a, curve *1* from Ref. 3) and the total defect distributions (Fig. 1a, curve *2*, from Ref. 3) were obtained in Refs. 2 and 3.

In accordance with Fig. 1a from Ref. 3 and Ref. 2, we select two large regions in terms of depth: $r<120$ nm and $r>120$ nm, to simplify the description of the physical changes. This division was introduced for the following reasons. First, in the region $r>120$ nm the defect distributions after irradiation at 400, 600, and 800 °C exhibit almost the same behavior: for $120<r<270$ nm the dependence on r may be neglected and for $r>270$ nm the concentration of RBS scattering centers is almost the same for samples irradiated at different temperatures. Second, in the region $r<120$ nm all three irradiated samples behave differently, as is reflected in the defect distributions.

We propose the following model[1)] to describe the processes taking place when SiC is irradiated by Al^+ and N^+ ions at temperature of 400 and 600 °C in the region $r>120$ nm.

1. The Al^+ and N^+ ions interact with the SiC crystal lattice to form interstitial sites (i) and vacancies (v) in both subsystems of the material (carbon—C and silicon—S) (the relative concentrations are $C_{iC}(r,t)$, $C_{vC}(r,t)$, $C_{iS}(r,t)$, and $C_{vS}(r,t)$, respectively).

2. The implanted Al^+ ions occupy vacancies in the silicon sublattice[7] while the N^+ ions occupy vacancies in the carbon sublattice[8] (the relative total concentration of both ions is $C(r,t)$).

3. During the irradiation process interstitial carbon (iC) and silicon (iS) atoms may diffuse and recombine with their vacancies (vC and vS).

4. The vacancies and implanted ions are assumed to be fixed because a) the vacancies have a high migration activation energy (see Ref. 9) and b) a comparison of the N^+ ion doping profiles in SiC calculated using DYTRIRS (Refs. 1–3) and those obtained experimentally (see Fig. 1b in Ref. 3) reveals that these ions do not diffuse at the temperatures used (we assume that this also applies to Al^+ ions).

5. Carbon (iC) and silicon (iS) interstitial sites form complexes consisting of two carbon or silicon interstitial sites (the relative concentrations are $C_{2C}(r,t)$ and $C_{2S}(r,t)$).

On the basis of assumptions (1)–(5), we write a system of rate equations for these concentrations of point defects which depend on the depth r and time t:

$$\frac{\partial C_{iC}(r,t)}{\partial t}=g_{iC}(r,t)-D_{iC}\Delta C_{iC}(r,t)-\mu_C D_{iC}C_{iC}(r,t)C_{vC}(r,t)-\alpha_{iC}D_{iC}C_{iC}^2(r,t), \quad (1)$$

$$\frac{\partial C_{vC}(r,t)}{\partial t}=g_{vC}(r,t)-g_N(r,t)-\mu_C D_{iC}C_{iC}(r,t)C_{vC}(r,t), \quad (2)$$

$$\frac{\partial C_{iS}(r,t)}{\partial t}=g_{iS}(r,t)-D_{iS}\Delta C_{iS}(r,t)-\mu_S D_{iS}C_{iS}(r,t)C_{vS}(r,t)-\alpha_{iS}D_{iS}C_{iS}^2(r,t), \quad (3)$$

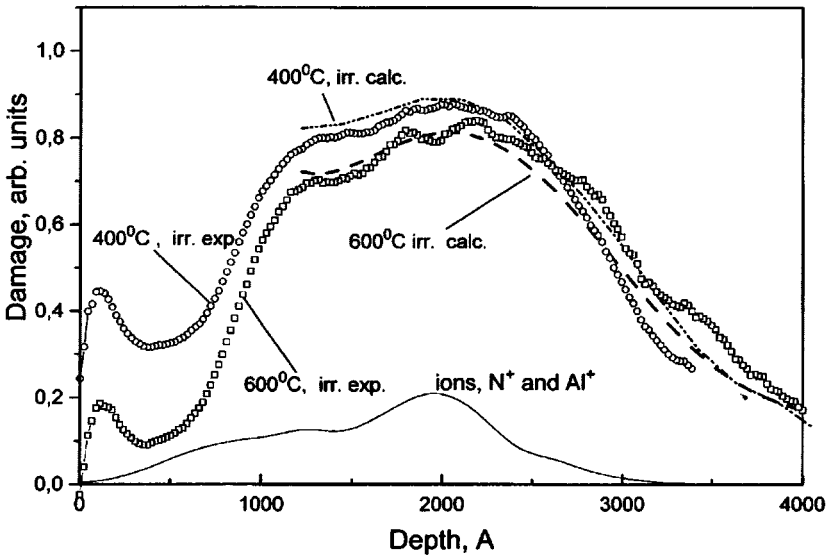

FIG. 1. Comparison between experimental RBS profiles of defect doping[3] (irr. exp.) and calculated total defect distributions (irr. calc.) (allowing for diffusion processes) in SiC samples irradiated at 400 and 600 °C. The curve labeled ''ions N^+ and Al^+'' gives the total ballistic ion doping profile in SiC calculated using the DYTRIRS code.[2,3]

$$\frac{\partial C_{v\mathrm{S}}(r,t)}{\partial t} = g_{v\mathrm{S}}(r,t) - g_{\mathrm{Al}}(r,t) - \mu_{\mathrm{S}} D_{i\mathrm{S}} C_{i\mathrm{S}}(r,t) C_{v\mathrm{S}}(r,t), \tag{4}$$

$$\frac{\partial C_{2\mathrm{C}}(r,t)}{\partial t} = \alpha_{i\mathrm{C}} D_{i\mathrm{C}} C_{i\mathrm{C}}^2(r,t), \tag{5}$$

$$\frac{\partial C_{2\mathrm{S}}(r,t)}{\partial t} = \alpha_{i\mathrm{S}} D_{i\mathrm{S}} C_{i\mathrm{S}}^2(r,t), \tag{6}$$

$$\frac{\partial C(r,t)}{\partial t} = g_{\mathrm{N,Al}}(r,t). \tag{7}$$

Here $g_l(r,t)$ is the rate of generation of the appropriate defects ($l = i\mathrm{C}$, $i\mathrm{S}$, $v\mathrm{C}$, $v\mathrm{S}$, Al, N) under irradiation $g_1(r,t) = JP_1(r)$, where $J = 6.24\ \mathrm{cm^2 \cdot s^{-1}}$ (Refs. 1–3) is the flux density of the incident ions, $P_1(r)$ are the depth distributions of defects 1 generated by a single incident ion, determined by TRIRS calculations[3] (the total profiles for all defects allowing for dose and neglecting recombination are plotted in Fig. 1a, curve *2* in Ref. 3); μ_λ is the recombination parameter of vacancies and interstitial sites in the $\lambda = C$, S subsystem; $D_j = D_{0j} \exp(-\varepsilon_j^m/kT)$ and ε_j^m are the diffusion coefficient and migration activation energy of interstitial carbon or silicon atoms ($j = i\mathrm{C}$, $i\mathrm{S}$), $\varepsilon_{i\mathrm{C}}^m = 1.47$ eV (Ref. 9), and since the value of $\varepsilon_{i\mathrm{S}}^m$ is not known from the literature, it was varied during the calculations; $D_{0j} = 10^{-3}\ \mathrm{cm^2 \cdot s^{-1}}$, and $\alpha_j \approx 4\pi a$ ($j = i\mathrm{C}$, $i\mathrm{S}$) is the complex formation parameter of the appropriate defects, where $a \approx 2$ Å is the average interatomic spacing in SiC.

Since the initial samples (before irradiation) are assumed to contain no defects, the initial conditions for the concentrations will be $C_l(r,t)|_{t=0} = 0$, where $l = i\mathrm{C}$, $i\mathrm{S}$, $v\mathrm{C}$, $v\mathrm{S}$, Al, and N.

The boundary conditions for the mobile defects $j = i\mathrm{C}$, $i\mathrm{S}$ are as follows:

1) $\partial C_j(r,t)/\partial r|_{r=120\ \mathrm{nm}} = 0$, i.e., it is assumed that there is no flux of diffusing defects at the boundary $r = 120$ nm. This condition is chosen because the concentration profiles at irradiation temperatures of 400, 600, and 800 °C for $r < 120$ nm suggest that they are mainly determined by recombination of vacancies and interstitial sites. This is evidenced by the concentration minimum at 800 °C which is equal to the concentration of implanted ions (see Fig. 1a in Ref. 3). Assuming that defects from deeper layers of the material may diffuse into this region, the concentration of intrinsic defects would not reach zero.

2) $C_j(r,t)|_{r=\infty} = 0$—the concentrations of defects $j = i\mathrm{C}$, $i\mathrm{S}$ are zero an infinite depth.

The system (1)–(7) describing the evolution of defects in SiC irradiated at 400 and 600 °C was solved numerically on an IBM PC using the MGEAR program.[10]

The calculated distributions of these defect concentrations after irradiation at 400 and 600 °C are plotted in Fig. 1, where they are compared with the profiles calculated from the RBS data (see Ref. 3). It can be seen that the theoretical results agree satisfactorily with the experimental data. Some difference between the calculated and experimental results is observed for $120\ \mathrm{nm} < r < 200\ \mathrm{nm}$, possibly because processes typical of the surface region ($r < 120$ nm), which we are not considering, begin to play an important role in this zone.

Some of the kinetic parameters used in Eqs. (1)–(7) were varied in the calculations. The best agreement between the calculated and experimental profiles was obtained for the following values of these parameters:

—migration activation energy of interstitial silicon atoms $\varepsilon_{i\mathrm{S}}^m \approx 1.55$ eV,

—recombination parameters for C and Si $\mu_{\mathrm{C}} \approx 4\pi \cdot 10^{-12}$ cm and $\mu_{\mathrm{S}} \approx 4\pi \cdot 10^{-10}$ cm.

It was also found in the course of the calculations that the constraint $C_k(r,t) < 0.2$ ($k = 2\mathrm{C}$, $2\mathrm{S}$) must be imposed on the complex concentration.

To sum up, we have proposed a physical model for the evolution of the defect structure in 6H–SiC implanted with N^+ and Al^+ ions for defect doping depths $r > 120$ nm and defect distributions in the material were calculated for $r > 120$ nm. Satisfactory agreement was achieved between the calculated and experimental results. Some kinetic param-

eters of silicon carbide were estimated numerically in the course of the calculations.

This work was supported by the Russian Fund for Fundamental Research, Grant No. 97-02-18110 and by a maintenance grant for leading scientific schools in the Russian Federation No. 96-15-96348.

[1)]We shall not analyze the sample irradiated at 800 °C because, when examined by transmission electron microscopy (TEM), this sample revealed a particular microstructure different to the samples irradiated at other temperatures and not as yet identified.

[1] R. A. Yankov, N. Hatzopoulos, W. Fukarek, M. Voelskow, V. Hera, J. Pezoldt, and W. Skorupa, Mater. Res. Soc. Symp. Proc. **438**, 271 (1997).
[2] V. S. Kharlamov, D. V. Kulikov, Yu. V. Truschin, D. N. Tsigankov, R. A. Yankov, M. Voelskow, W. Skorupa, and J. Pezoldt, Program and Abstracts of the International Workshop on New Approaches to High-Tech Materials '97 (Nondestructive Testing and Computer Simulations in Materials Science and Engineering), St. Petersburg, 1997, pp. 2–13.
[3] R. A. Yankov, M. Voelskow, W. Kreissig, D. V. Kulikov, J. Pezoldt, V. Skorupa, Yu. V. Trushin, V. S. Kharlamov, and D. N. Tsigankov, Pis'ma Zh. Tekh. Fiz. **23**(6), 6 (1997) [Tech. Phys. Lett. **23**, (1997)].
[4] B. J. Ber, A. V. Merkulov, V. S. Kharlamov, Yu. V. Trushin, and E. E. Zhurkin, Zh. Tekh. Fiz. **66**(3), 54 (1996) [Tech. Phys. **41**, 261 (1996)].
[5] Yu. V. Trushin, B. J. Ber, V. S. Kharlamov, and E. E. Zhurkin, J. Nucl. Mater. **233/237**, 991 (1996).
[6] B. J. Ber, V. S. Kharlamov, Yu. V. Trushin, A. V. Merkulov, and E. E. Zhurkin, Proceedings of the Tenth International Conference on Ion Beam Modification of Materials, Albuquerque, NM, 1996, Paper Tu29.
[7] W. J. Choyke and G. Pens, MRS Bull. March 1997, p. 25.
[8] F. Tsvetkov, S. T. Allen, H. C. Kong, and C. H. Carter, Jr., Proceedings of the Sixth International Conference on Silicon Carbide and Related Materials, edited by S. Nashikama, S. Yoshida, and H. Harima (Institute of Physics Conference Series, No. 142, AIP Press, 1996), p. 17.
[9] H. Huang and N. Ghoniem, J. Nucl. Mater. **212–215**, 148 (1994).
[10] D. V. Kulikov, R. A. Suris, and Yu. V. Trushin, Supercond. Sci. Technol. **8**, 303 (1995).

Translated by R. M. Durham

Efficient x-ray converters

V. I. Bespalov, V. V. Ryzhov, and I. Yu. Turchanovskiĭ

Tomsk Polytechnic University, Institute of High-Current Electronics, Siberian Branch of the Russian Academy of Sciences, Tomsk

(Submitted June 23, 1997)
Pis'ma Zh. Tekh. Fiz. **24**, 45–48 (January 12, 1998)

The Monte Carlo method is used to investigate the efficiency of conversion of the energy of low-energy electrons into x-ray radiation energy and it is shown that the characteristic radiation makes an important contribution to the energy absorbed by thin films undergoing radiation treatment. Selecting the converter material and thickness on the basis of the calculations can increase by a factor of 2–5 the radiation energy absorbed in thin films of semiconductor materials. © *1998 American Institute of Physics.* [S1063-7850(98)00801-5]

The laws governing the generation of bremsstrahlung observed when high-energy electrons are stopped in a target have been comprehensively studied experimentally and theoretically.[1,2] High-Z materials (tungsten and tantalum) are usually used at these energies to give the maximum bremsstrahlung yield. However, when low-energy electrons are stopped, an appreciable fraction of the energy may be emitted in the form of characteristic radiation which is generated as a result of the photoabsorption of secondary photons and by electron impact ionization of the inner atomic shells. Since the cross section of the second process increases with decreasing Z, x-ray radiation may be generated highly efficiently in low-Z materials.

This factor must be taken into account in the radiation treatment of thin films and foils, whose efficiency is governed not only by the total radiation energy, but also by its spectral composition. In order to optimize the irradiation conditions and select efficient x-ray converters for the processing of thin films, we used a program which simulates the evolution of the electron-photon cascade in the converter, and the absorption of radiation by the film material using the Monte Carlo method. A variant of the program[3] which allows for the generation of characteristic radiation as a result of ionization of the K-shell by bremsstrahlung quanta and electrons, was developed to calculate the spectral distribution of the radiation behind the converter. The cross section for electron impact K ionization was taken from Ref. 4.

In order to study the optimum conditions for radiation treatment of thin films, we calculated the absorbed energy in thin films of semiconductor materials for converters with different atomic numbers $Z=29$, 42, 57, and 73. The initial electron energy varied between 50 and 500 keV. The converter thickness was optimized for the total yield of radiation energy and a graphite plate of suitable thickness was positioned behind the converter to absorb the outgoing electrons.

The important role of the characteristic radiation behind converters with different atomic numbers Z can be deduced from the data presented in Table I. It can be seen that up to initial electron energies $E_0=100$ keV, the total yield of x-ray radiation energy behind copper converters is higher than that behind tantalum converters. In this case, the contribution of the characteristic radiation exceeds 50% for copper whereas it is an order of magnitude lower for tantalum.

The results of the calculations for silicon films exposed to x-ray radiation from electrons having an initial energy of 500 keV are plotted in Fig. 1. The calculations showed that the choice of converter material depends on the foil thickness and on the initial electron energy. For example, for $E_0=500$ keV copper converters should be used to process thin silicon films ($d<100$ μm) whereas molybdenum con-

TABLE I. Energy of outgoing photons behind a converter of optimum thickness (keV) and fraction of characteristic radiation (%) (The results are normalized to a single incident electron).

E_0, keV	Cu	Mo	La	Ta
50	0.098	0.0608	0.0516	0.060
	69	40	16	0
100	0.235	0.224	0.221	2.43
	54	34	16	5
500	2.26	3.10	4.08	5.08
	5	8	9	8

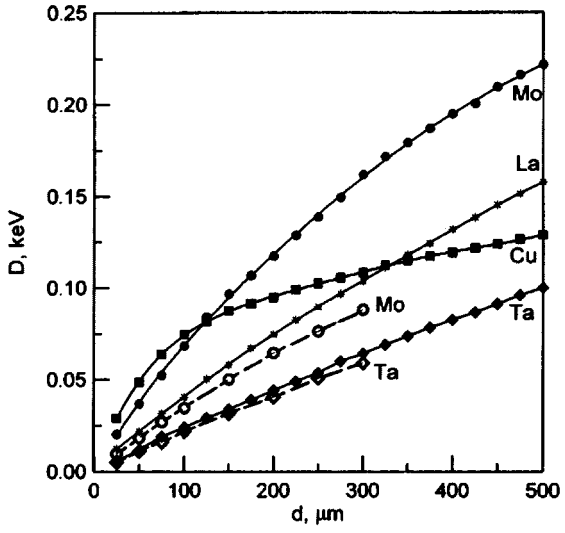

FIG. 1. Energy of x-ray radiation absorbed in a layer of silicon as a function of its thickness and the converter material for an initial electron energy $E_0=500$ keV. The solid curves give the calculations for unprotected films and the dashed curves gives those for films coated with a 500 μm thick layer of SiO_2 (the results of the calculations are normalized to a single incident electron).

verters are most efficient for thick films ($100<d<500$ μm). The figure shows that the energy absorbed by a silicon film is approximately twice that for conventional tantalum converters. The calculations indicate that for lower initial electron energies copper converters are the most efficient, giving a five-sixfold improvement in absorbed energy compared with tantalum converters for $E_0=100$ keV.

The coatings frequently used to protect semiconductor films, such as the active elements of solar cells, play a significant role in redistribution of the absorbed energy. In Fig. 1 the dashed curves give the results of calculations of the energy absorbed by a silicon film coated with a 500 μm thick SiO_2 layer. This figure shows that molybdenum foils should be used as converters in experiments to study the action of x-ray radiation on elements of solar cells. These converters are 1.3–2 times more efficient that conventional tantalum converters.

The calculations have shown that molybdenum converters should only be used for the treatment of very thin germanium films ($d<20$ μm) and lanthanum converters are more efficient for films of moderate thickness ($20<d<200$ μm).

[1] J. A. Halbleib, G. J. Lockwood, and G. H. Miller, IEEE Trans. Nucl. Sci. **NS-23**, 1881 (1976).
[2] V. V. Ryzhov and A. A. Sapozhnikov, Proceedings of the Ninth International Conference on High-Power Particle Beams, ''Beams-92'', Washington, DC, 1992, Vol. 2, pp. 1199–1204.
[3] V. I. Bespalov, S. D. Korovin, V. V. Ryzhov, and I. Yu. Turchanovsky, Proceedings of the Tenth International Pulsed Power Conference, Albuquerque, NM, 1995, Vol. 1, pp. 75–79.
[4] H. Kolbenstvedt, J. Appl. Phys. **38**, 4785 (1967).

Translated by R. M. Durham

Low-threshold quantum-dot injection heterolaser emitting at 1.84 μm

V. M. Ustinov, A. R. Kovsh, A. E. Zhukov, A. Yu. Egorov, N. N. Ledentsov,
A. V. Lunev, Yu. M. Shernyakov, M. V. Maksimov, A. F. Tsatsul'nikov, B. V. Volovik,
P. S. Kop'ev, and Zh. I. Alferov

A. F. Ioffe Physicotechnical Institute, Russian Academy of Sciences, St. Petersburg
(Submitted August 12, 1997)
Pis'ma Zh. Tekh. Fiz. **24**, 49–54 (January 12, 1998)

The use of InAs quantum dots in an InGaAs matrix lattice-matched with an InP substrate can appreciably increase the emission wavelength of quantum-dot lasers. Lasing via quantum-dot states at the 1.84 μm wavelength (77 K) was obtained for the first time at a threshold current density of 64 A/cm^2. © *1998 American Institute of Physics.* [S1063-7850(98)00901-X]

The use of zero-dimensional objects—quantum dots—can substantially enhance the characteristics of semiconductor lasers.[1] The spontaneous transformation of an elastically strained layer into an array of three-dimensional islands[2,3] was used to develop arrays of quantum dots in the active region of an injection laser.[4] It was observed that these lasers exhibit a low threshold current density (25 A/cm^2 at 77 K, 65 A/cm^2 at 300 K) (Ref. 5) and the threshold current possesses enhanced temperature stability (characteristic temperature $T_0 > 400$ K) compared with quantum-well lasers, as has been predicted theoretically.[1] In addition, cw lasing was achieved via the ground state of (In, Ga)As quantum dots at room temperature.[5,6]

It has now been shown that the emission wavelength of InGaAs quantum dots grown on GaAs substrates has a long-wavelength limit of 1.27–1.3 μm (Refs. 7 and 8) and lasing has been observed in the spectral range 0.9–1.1 μm. However, for many practical applications, especially in fiber-optic communication systems and monitoring of environmental pollution, the emission wavelength must be increased to the middle infrared.

We have already shown that progress in this wavelength range may be achieved by using arrays of InAs quantum islands in a $In_{0.53}Ga_{0.47}As$ matrix grown on an InP (100) substrate.[9] The longer emission wavelength compared with (In, Ga)As quantum dots in a GaAs matrix is mainly attributed to the use of a narrower-gap matrix. The longest wavelength reported was 1.944 μm (77 K).

Here, we report for the first time the attainment of 1.84 μm lasing via the state of InAs quantum dots in an (In, Ga)As matrix lattice-matched with InP.

The laser structure shown schematically in Fig. 1 was grown by molecular-beam epitaxy with a solid-state As_4 source in a Riber 32P machine. A 0.6 μm thick $In_{0.53}Ga_{0.47}As$ waveguide layer was grown directly on a n^+-InP (100) substrate which served as the lower emitter. At the center of the waveguide layer there were three layers of InAs quantum dots separated by 5 nm thick $In_{0.53}Ga_{0.47}As$ spacer layers. The effective thickness of the deposited InAs in each cycle was 7 ML. The upper emitter was formed by a 1.5 μm p^+-layer of $In_{0.52}Al_{0.48}As$. The structure finished with a 0.6 μm thick p^+ contact layer of $In_{0.53}Ga_{0.47}As$. Beryllium was used as the p-type dopant. The entire structure was grown at 500 °C, and the growth rate was 10 nm/min for the InGa(Al)As layers and 5 nm/min for the deposition of InAs in the active region. The structure was grown under arsenic enrichment conditions.

Stripe lasers 100 μm wide were formed in a ''shallow mesa'' geometry. The ohmic contacts with the p^+-layer were made of Ti/AuZn/Ni/Au alloys and those with the n^+-InP substrate were made of Au:Te/Ni/Au. The p^+-InGaAs contact layer outside the stripe was etched with an Ar (600 eV) ion beam. The mesastructure was passivated chemically and was protected with a 0.2 μm thick Al_2O_3 layer by reactive magnetron sputtering. The electroluminescence was measured in the pulsed mode at 77 K at a frequency of 5 kHz and a pulse length of 1 μs. Structures with the upper contact layer removed were used to study the photoluminescence, which was excited by a semiconductor GaAs laser and recorded with a cooled InSb photodiode. The excitation power was 100 W/cm^2.

A transition from two-dimensional to three-dimensional InAs growth was observed directly during the growth process from the streaky reflection high-energy electron diffraction (RHEED) pattern. Transmission electron microscopy data[9,10] confirm that three-dimensional strained islands are formed in the active region. The average base diameter of the islands is approximately 50 nm with a height of approximately 4–5 nm.

The threshold current density in a 1.25 nm long stripe laser was 64 A/cm^2, which is comparable with the best threshold current densities of lasers whose active region is formed by InGaAs quantum dots grown on GaAs substrates. The lasing wavelength was 1.84 μm, which substantially exceeds the wavelengths achieved previously in lasers whose active region is formed by quantum dots in a (Al, Ga)As matrix on GaAs substrates.

Figure 2 shows electroluminescence spectra at pump current densities of 13 and 70 A/cm^2, which corresponds to 0.2 and 1.1 J_{th}. For comparison Fig. 2 also shows the photoluminescence spectrum for a low level of excitation ($\sim$100 W/cm^2). We showed in Ref. 9 that this photoluminescence line is attributable to radiative recombination of nonequilibrium carriers via quantum-dot states. The line profile is determined by the size spread of the islands. A comparison between the photoluminescence and electroluminescence spectra indicates that the lasing line falls within the luminescence band of the quantum dots. Thus, lasing takes

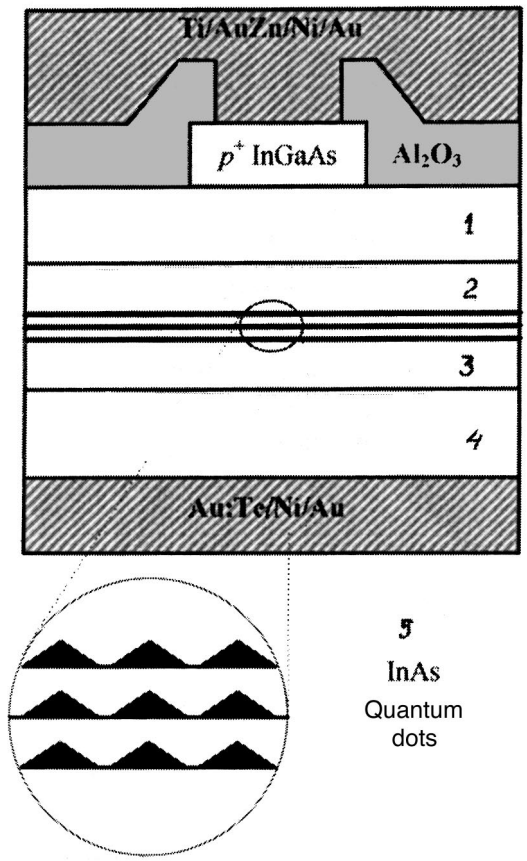

FIG. 1. Schematic of laser structure with active region formed by InAs quantum dots in an InGaAs matrix grown in an InP substrate. *1*—*p*-*n*-AlAs upper emitter, *2*,*3*—InGaAs waveguide, *4*—n^+InP(100) substrate, lower emitter, and *5*—InAs quantum dots.

place via quantum dot states. The position of the lasing line at the short-wavelength side of the photoluminescence spectrum indicates that islands having smaller dimensions than the average size of the island ensemble and therefore having a lower carrier localization energy participate in the lasing process.

To sum up, low-threshold (64 A/cm^2) lasing at 1.84 μm has been obtained for the first time in quantum-dot structures.

This work was supported by the Russian Fund for Fundamental Research (Project No. 96-02-17824).

[1] Y. Arakawa and H. Sakaki, Appl. Phys. Lett. **40**, 939 (1982).
[2] L. Goldstein, F. Glas, J. Y. Marzin, M. N. Charasse, and G. Le Roux, Appl. Phys. Lett. **47**, 1099 (1985).

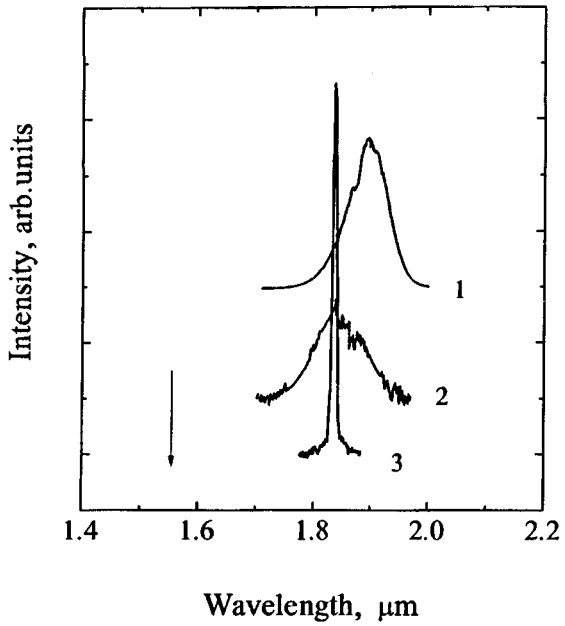

FIG. 2. Photoluminescence (curve *1*) and electroluminescence spectra (curves *2* and *3*) of laser structure. The pump current density is 13 and 70 A/cm^2 (curves *2* and *3*, respectively). The arrow indicates the edge luminescence of the InGaAs matrix.

[3] P. M. Petroff and S. P. Den Baars, Superlattices Microstruct. **15**, 15 (1994).
[4] N. Kirstaedter, N. N. Ledentsov, M. Grundmann, D. Bimberg, V. M. Ustinov, S. S. Ruvimov, M. V. Maximov, P. S. Kop'ev, Zh. I. Alferov, U. Richter, P. Werner, U. Gösele, and J. Heydenreich, Electron. Lett. **30**, 1416 (1994).
[5] V. M. Ustinov, A. Yu. Egorov, A. R. Kovsh, A. E. Zhokov, N. N. Ledentsov, M. V. Maksimov, A. F. Tsatsul'nikov, N. Yu. Gordeev, S. V. Zaitsev, Yu. M. Shernyakov, N. A. Bert, P. S. Kop'ev, Zh. I. Alferov, N. N. Ledentsov, J. Bohrer, D. Bimberg, A. O. Kosogov, P. Werner and U. Gosele, J. Cryst. Growth **175**, (1997).
[6] Yu. M. Shernyakov, A. Yu. Egorov, A. E. Zhukov, S. V. Zaĭtsev, A. R. Kovsh, I. L. Krestnikov, A. V. Lunev, N. N. Ledentsov, M. V. Maksimov, A. V. Sakharov, V. M. Ustinov, Chzhao Chzhen', P. S. Kop'ev, Zh. I. Alferov, and D. Bimberg, Pis'ma Zh. Tekh. Fiz. **23**(4), 51 (1997) [Tech. Phys. Lett. **23**, 149 (1997)].
[7] A. Yu. Egorov, A. E. Zhukov, P. S. Kop'ev, N. N. Ledentsov, M. V. Maksimov, V. M. Ustinov, A. F. Tsatsul'nikov, Zh. I. Alferov, D. L. Fedorov, and D. Bimberg, Fiz. Tekh. Poluprovodn. **30**, 1345 (1996) [Semiconductors **30**, 707 (1996)].
[8] R. P. Mirin, J. P. Ibbetson, K. Nishi, A. C. Gossard, and J. E. Bowers, Appl. Phys. Lett. **67**, 3795 (1995).
[9] V. M. Ustinov, A. E. Zhukov, A. F. Tsatsul'nikov, A. Yu. Egorov, A. R. Kovsh, M. V. Maksimov, A. A. Suvorova, N. A. Bert, and P. S. Kop'ev, Fiz. Tekh. Poluprovodn, in press (1997).
[10] V. M. Ustinov, E. R. Weber, S. Ruvimov, Z. Liliental-Weber, A. E. Zhukov, A. Yu. Egorov, A. R. Kovsh, A. F. Tsatsul'nikov, and P. S. Kop'ev, Appl. Phys. Lett. , in press (1997).

Translated by R. M. Durham

Influence of low-temperature annealing on the properties of $Y_1Ba_2Cu_3O_{7-\delta}$ thin films

Yu. N. Drozdov, S. A. Pavlov, and A. E. Parafin

Institute of Physics of Microstructures, Russian Academy of Sciences, Nizhniĭ Novgorod
(Submitted May 23, 1997)
Pis'ma Zh. Tekh. Fiz. **24**, 55–58 (January 12, 1998)

The influence of annealing at 180 °C on the structure, critical temperature, and electrical resistivity of $Y_1Ba_2Cu_3O_{7-\delta}$ thin films has been investigated. It is shown that films grown at reduced temperatures are sensitive to this annealing, which can substantially alter these film parameters. © *1998 American Institute of Physics.* [S1063-7850(98)01001-5]

For a long time after the discovery of $Y_1Ba_2Cu_3O_{7-\delta}$ (YBCO), it was assumed that the maximum superconducting transition temperature (T_c) is achieved for $\delta=0$, i.e., for complete oxidation. More detailed studies of YBCO at low δ have shown that there is an optimum value $\delta\simeq 0.1$ for which T_c has a maximum, and in the range $\delta<0.1$ YBCO is ''over-oxidized'' and T_c is several degrees below its maximum.[1]

Gavaler *et al.*[2] studied the influence of oxygen content on the properties of YBCO thin films and they showed that, as in bulk samples, maximum T_c is achieved for a certain optimum oxygen content. The oxygen content was controlled by low-temperature annealing. In this context, an annealing temperature T_a around 400 °C, which is substantially lower than the growth temperatures (600–700 °C), is taken to be ''low.''

Our investigations have shown that epitaxial layers of YBCO may be sensitive to annealing above $T_a<200$ °C. Moreover, by using such low temperatures, we were able to make a detailed study of the changes in T_c, the electrical resistivity, and the lattice period ''c'' as a function of the annealing time.

The films were prepared by sputtering a YBCO ceramic target with excimer laser radiation ($\lambda=248$ nm, $\tau=27$ ns). The pulse energy density was 10 J/cm^2 and the repetition frequency was 50 Hz. The growth rate under these conditions was 0.01 nm per pulse. The films were deposited on single-crystal $NdGaO_3$ substrates at a growth temperature $T_d\simeq 620$ °C. The film thickness was 100 nm. The film formation process concluded with natural cooling to room temperature at an oxygen pressure of 100 kPa for 30 min.

The resistivity of the film was measured by a four-probe method, for which silver contacts were deposited on the film by thermal evaporation to provide a stable low contact resistance. The temperature T_c was determined from the point of zero resistance of the film. The structure was analyzed and the lattice c period was measured by an x-ray diffraction technique using a DRON-4 diffractometer.

The films were annealed at 180 °C in an oxygen atmosphere at a pressure of 10 Pa in 10–20 min steps . The film parameters were determined after each step. Figure 1 shows the change in the critical temperature T_c and the lattice c period as a function of the resistivity ρ_{100} measured at 100 K. The value of ρ_{100} increased monotonically so that the points on the graph have a sequence of annealing cycles.

It can be seen that T_c increased at the initial annealing stage, by 5 K after two steps, and then decreased to the boiling point of nitrogen after seven steps. The lattice c period increased linearly. The temperature T_c has a parabolic dependence on ρ_{100} similar to the data for YBCO single crystals.[1]

We analyzed these data using empirical relations linking the lattice c period to the concentration p of conduction holes in the Cu–O plane per Cu atom:[3,4]

$$p=0.187-0.21\delta, \tag{1}$$

$$c=1.2771-0.01557x, \tag{2}$$

where $x=7-\delta$.

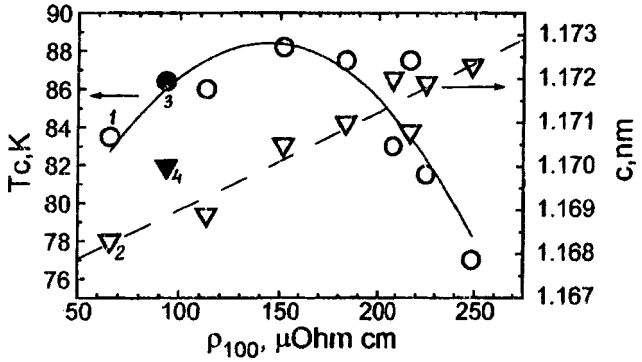

FIG. 1. Critical temperature T_c (*1*) and lattice c period (*2*) as a function of the resistivity ρ_{100} of a YBCO film during annealing at 180 °C and an oxygen pressure of 10 Pa. Also T_c (*3*) and c (*4*) after annealing at 550 °C and an oxygen pressure of 100 kPa.

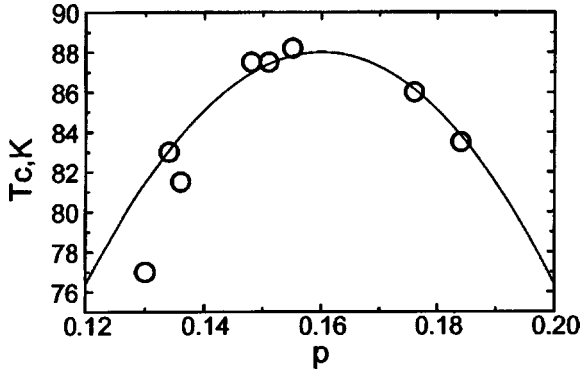

FIG. 2. Critical temperature T_c versus concentration p of conduction holes in Cu–O plane per Cu atom. The solid curve gives the dependence (3) for $T_{cmax}=88$ K.

 1063-7850/98/010024-02$15.00

The p values calculated from formulas (1) and (2) can be used to compare our experimental data with the universal dependence of the reduced critical temperature $T_c/T_{c\max}$ on the concentration of conduction holes for high-temperature superconducting cuprates:[3]

$$T_c/T_{c\max}=1-82.6(p-0.16)^2. \quad (3)$$

The results are plotted in Fig. 2. The solid curve gives the dependence (3), where $T_{c\max}=88$ K. It can be seen that the experimental points are a good fit to the universal curve. It can thus be assumed that the formulas (1) and (2) obtained for bulk samples are also valid for our films and the observed changes in T_c and the lattice c period during annealing are caused by a reduction in the oxygen content in the YBCO structure.

It is interesting to note that increasing the oxygen pressure to 100 kPa during annealing did not alter the curves plotted in Fig. 1, although the changes took place over a longer time compared with the annealing at 10 Pa.

The changes in the film were reversible: we could transfer the film from a final state with $T_c<77$ K to a state close to the initial one (see Fig. 1) by annealing at 550 °C in an oxygen atmosphere at a pressure of 100 kPa for 25 min. This result confirms the role of oxygen in the observed processes.

It should be noted that our films obtained at growth temperatures $T_d\simeq 700$ °C, as in Ref. 2, do not exhibit any ''overoxidized'' state with reduced T_c. This behavior evidently arises because the hole concentration and related T_c are determined not only by the oxygen content but also by other factors.

This work was supported by the Russian Fund for Fundamental Research (Grant 9602-16993), the Integral Project 95043 of the Superconductivity Section of the State Program ''Current Trends in the Physics of Condensed Media,'' and by INTAS Grant 943912.

[1] H. Claus, U. Gebhard, J. Linker *et al.*, J. Phys. C **3&4**, 271 (1992).
[2] J. R. Gavaler, J. Talvaccio, R. W. Weinert *et al.*, IEEE Trans. Appl. Supercond. **5**, 1173 (1995).
[3] J. R. Tallon, C. Bernhard, and H. Shaked, Phys. Rev. B **51**, 12911 (1995).
[4] M. Ohkubo, T. Kachi, T. Hioki *et al.*, Appl. Phys. Lett. **55**, 899 (1989).

Translated by R. M. Durham

Transport of electronic excitation energy in solid-state glassy phosphors activated with europium (III) and copper (II)

I. M. Batyaev and A. M. Tinus

A. I. Gertsen Russian State Pedagogical University, St. Petersburg
(Submitted June 26, 1997)
Pis'ma Zh. Tekh. Fiz. **24**, 59–61 (January 12, 1998)

A phosphor based on potassium aluminosilicophosphate glass activated with europium (III) and copper (II) has been synthesized. It has been shown that the europium luminescence is quenched by copper ions in the glass. © *1998 American Institute of Physics.*
[S1063-7850(98)01101-X]

Reports of the production of new lasing crystals are not halting development work to improve the base materials of laser glasses. Despite the wide range of laser glasses of varying composition, the development and study of new glass-forming materials with specific physicochemical and spectral luminescence properties is still topical. The problem of improving the energy efficiency of solid-state phosphors has attracted particular attention. One method of solving this problem involves using nonradiative energy transport by introducing various sensitizers into the matrix.[1–3] However, as well as sensitizers, there are also luminescence quenching agents whose presence completely or partially suppresses the luminescence of the required ion. It is therefore important to identify these quenching agents in order to avoid combining these with a luminescence activator.

Here we investigate the interaction between Eu^{3+} and Cu^{2+} in potassium aluminosilicophosphate glass. Trivalent europium is first, a luminescence activator for which lasing has been achieved[4–7] and second, is widely used as an optical probe to study the structure of many materials.[8]

Silicon oxide, potassium metaphosphate, and aluminum were used to prepare the charge. Europium was introduced in the form of the oxide Eu_2O_3 and copper was introduced as the oxide CuO. The concentration of activator ions was 5 wt. % for europium and 0.1 wt. % for copper.

The electronic absorption spectra were recorded using an SF-20 spectrophotometer. The luminescence spectra were recorded with an SDL-1 spectrometer using an FEU-62 photomultiplier. The luminescence was excited by an LGI-21 nitrogen laser ($\lambda_B = 337$ nm).

Figure 1 shows that the bands in the luminescence spectrum of europium (curve *A*) and the absorption band of copper (curve *B*) are superposed, which suggests that the luminescence of the europium (III) ions may be quenched by the copper (II) ions. This conclusion was confirmed by studying the luminescence spectra and the decay kinetics of the europium luminescence in glass doped only with Eu^+ ions and in glass doped with both Eu^{3+} and Cu^{2+} ions.

In the luminescence spectrum of the glass coactivated with both Eu^{3+} and Cu^{2+} ions the relative intensity of the europium luminescence band is reduced approximately 1.5 times.

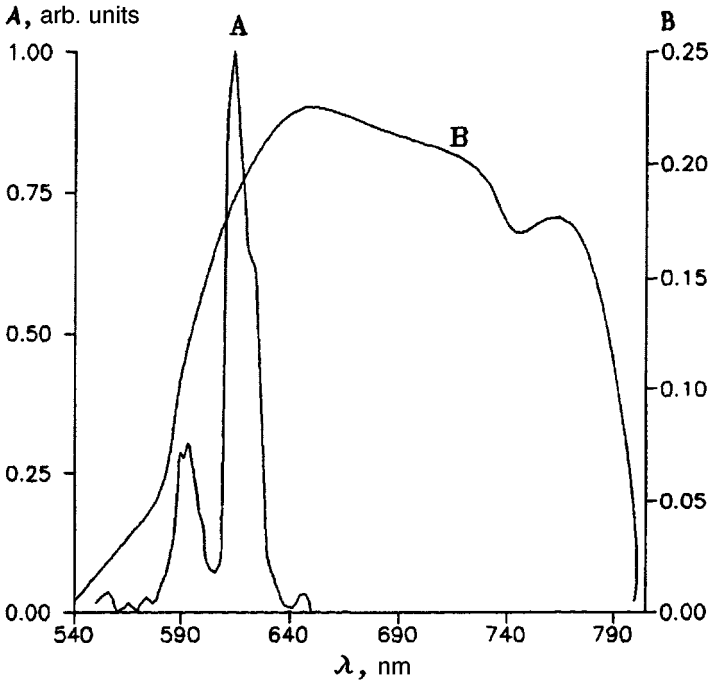

FIG. 1. Luminescence spectrum (*A*) of potassium aluminosilicophosphate activated with Eu^{3+} and absorption spectrum (*B*) of potassium aluminosilicophosphate activated with Cu^{2+}.

An analysis of the luminescence decay kinetics revealed that the average excited-state lifetime of the Eu^{3+} ions was reduced from 2.5 to 38.5 μs in the presence of Cu^{2+} ions.

To sum up, the interaction between Eu^{3+} and Cu^{2+} has been investigated for the first time in glasses and is observed as quenching of the europium (III) ion luminescence in the presence of copper (II) ions.

[1] V. L. Ermolaev, E. N. Bodunov, E. B. Sveshnikova, and T. A. Shakhverdov, *Nonradiative Transport of Electronic Excitation Energy* [in Russian], Nauka, Moscow (1977).

[2] V. M. Agranovich and M. D. Galanin, *Electronic Excitation Energy Transfer in Condensed Matter* (North-Holland, Amsterdam, 1982) [Russ. original, Nauka, Moscow, 1978].

[3] N. E. Alekseev, V. P. Gapontsev, M. E. Zhabotinskiĭ, B. V. Kravchenko, and Yu. P. Rudnitskiĭ, *Laser Phosphate Glasses* [in Russian], Nauka, Moscow (1980).

[4] N. C. Chang, J. Appl. Phys. **34**, 3500 (1963).

[5] A. Lempicki and H. Samelson, Phys. Lett. **4**, 133 (1963).

[6] I. M. Batyaev, Usp. Khim. **40**, 1333 (1971).

[7] *Laser Handbook*, edited by A. M. Prokhorov [Russ. transl. with changes and additions, Sovet-skoe Radio, Moscow, 1978].

[8] V. F. Zolin and L. G. Koreneva, *Rare-Earth Probes in Chemistry and Biology* [in Russian], Moscow (1980).

Translated by R. M. Durham

Use of AL307 light-emitting diodes as photodetectors for diagnostics of femtosecond light pulses

V. I. Baraulya, S. M. Kobtsev, and A. V. Korablev

Novosibirsk State University
(Submitted June 24, 1997)
Pis'ma Zh. Tekh. Fiz. **24**, 62–65 (January 12, 1998)

A nonlinear electrical response has been observed for the first time from AL307 light-emitting diodes exposed to femtosecond light pulses. When used in an unconventional fashion as unbiased photodiodes, these AL307 light-emitting diodes give an electrical response proportional to the square of the recorded radiation intensity of ultrashort light pulses. Autocorrelation functions are given for femtosecond pulses obtained using AL307 light-emitting diodes in the autocorrelator instead of the conventional photodetector and nonlinear crystal system.
 [S1063-7850(98)01201-4]

An AlGaAs light-emitting diode (LED) used as an unbiased photodiode to record optical radiation, may give a nonlinear electrical response proportional to the square of the incident radiation intensity. This effect was first demonstrated in Ref. 1 when an RS Components LED, having a radiation peak at 660 nm (Catalog No. 564-015) was exposed to 80 fs and 1 ps light pulses from a Ti:sapphire laser. It was assumed that the nonlinear electrical response of these photodiodes was either caused by direct two-photon absorption of radiation in the diode or by second harmonic generation in GaAs.

We observed a similar effect with Russian AL307 LEDs having radiation peaks at 666 nm (AL307BM) and at 666 and 566 nm (AL307EM). Here we report results of a direct experimental comparison between the characteristics of AL307 and 564-015 LEDs when used as photodetectors for the diagnostics of ultrashort light pulses.

For the experiments we used the FEMTIS femtosecond Ti:sapphire laser (pulse length 110–130 fs, pulse repetition frequency 108 MHz, and average radiation power up to 500 mW in the 780 nm range) and an FS-PS scanning autocorrelator with the data recorded by computer (the apparatus was built in the Laser Technology Department of Novosibirsk State University[2]). The LEDs being studied were used in the autocorrelator, replacing the conventional nonlinear crystal and photodetector system. The FS-PS autocorrelator was based on a Michelson interferometer, and a variable time delay of the pulses in one of the interferometer arms was provided by a pair of parallel mirrors which could be tilted by an angle up to $\pm 4°$. The range and scanning frequency of the autocorrelator are 0.02–30 ps and 0.01–20 Hz, respectively, with 15 fs time resolution.

Figure 1 gives interference autocorrelation functions obtained using a nonlinear BBO crystal (100 μm thick) and a Burr-Brown OPT-301 photodetector (a), the RS Components LED (b), and the Russian LEDs Al307–AL307BM (c), and AL307EM (d).

The LEDs were used in two modes.

1. In the usual form, where radiation was fed into the diode along the axis of symmetry of the polymethylmethacrylate package across the spherical surface, with the radiation prefocused by a spherical lens of 35 mm focal length.

2. With the upper part of the package removed, where radiation could be fed into the diode through a flat transparent (or colored for the AL307 diodes) polymethylmethacrylate surface positioned around 1 mm from the diode. In this case, the radiation was focused using lenses of 35 and 15 mm focal length.

The nonlinear electrical response was recorded for all the LEDs in both modes, but in mode 2 this response was slightly higher than that in mode 1 (for the same incident radiation powers). In our view, this behavior is attributable to the better focusing of the radiation. The load resistance of these photodetectors was set at 680 kΩ, and the output signal began to fall off appreciably and become distorted when the autocorrelator scanning frequencies exceeded 10–15 Hz. Note that with a load resistance of 680 kΩ for the RS Components LEDs in mode 2, we obtained output signal amplitudes three times higher than those in Ref. 1—150 mV when the radiation power incident on the photodetector was 7 mW. When the load resistance was increased, the amplitudes of the output signals increased but the response time of the photodetectors decreased. The amplitudes of the output signals from the AL307 LED photodetectors with modified package geometry were 25 mV for an average power of the recorded femtosecond radiation pulses of 7 mW.

Figure 1 gives autocorrelation functions obtained using LEDs with unchanged (Fig. 1b) and modified package geometry (Figs. 1c and 1d). All the autocorrelation functions are almost identical and in our opinion, the slight differences in the profile are attributable to a corresponding slight deformation of the femtosecond pulse shape caused by the different tuning of the titanium sapphire laser at different measurement times.

The relatively arbitrary choice of Russian LEDs made by us, suggests that there is evidently a class of LEDs having a nonlinear electrical response when used as unbiased photodiodes to record ultrashort light pulses. There is clearly a need for a detailed study of this phenomenon, and to continue our search for, and study of, various LEDs suitable for use as photodetectors for the diagnostics of light pulses of different duration and power in different spectral ranges.

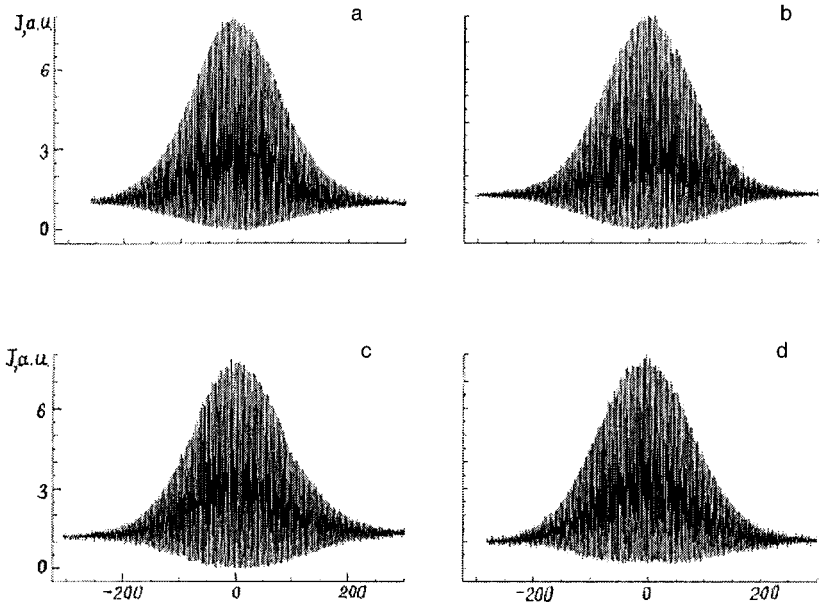

FIG. 1.

Note that an effect associated with the photoconduction of a semiconductor (ZnSe) induced by two-photon excitation during the recording of ultrashort light pulses was observed in Ref. 3. As in our experiments, the radiation source was a Ti:Sapphire laser (pulse length 120 fs, repetition frequency 76 MHz, central wavelength 800 nm). According to the data given in Ref. 3, the output signal from a specially fabricated ZnSe-based photodetector was 0.7 V (without amplification) and 60 mV when the average power of the recorded radiation was 10 mW and 1 mW, respectively. The mechanism responsible for the nonlinear electrical response of the AL307 LEDs exposed to ultrashort light pulses may be similar to that described in Ref. 3.

Since these AL307 LEDs are extremely cheap and readily available, and they are also easy to use and fairly sensitive as photodetectors, they can completely replace the conventionally used nonlinear crystal and photomultiplier, or photodiode systems in scanning autocorrelators, at least in the middle infrared, for measuring the length of ultrashort light pulses from Ti:Sapphire, Cr:LiSAF, Cr:LiS GaF, and other lasers. These LEDs may also be used as sensors for electronic display systems and for automatic triggering of mode self-locking in various lasers.

[1] D. T. Reid, M. Padgett, C. McGowan, W. E. Sleat, and W. Sibbett, Opt. Lett. **22**, 233 (1997).
[2] Novosibirsk State University Laboratory of Laser Systems Internet home page, URL: http://www.cnit.nsu.ru/nwww/lls/english/index.htm
[3] W. Rudolph, M. Sheik-Bahae, A. Bernstein, and L. F. Lester, Opt. Lett. **22**, 313 (1997).

Translated by R. M. Durham

Field-ion microscope analysis of the action of laser pulses on the surface of $YBa_2Cu_3O_{7-y}$ single crystals

G. G. Kuzyakhmetov, A. F. Bobkov, A. L. Suvorov, Yu. N. Cheblukov, A. N. Balabaev, and A. S. Fedotov

State Scientific Center—Institute of Theoretical and Experimental Physics, Moscow
(Submitted August 28, 1997)
Pis'ma Zh. Tekh. Fiz. **24**, 66–72 (January 12, 1998)

Field-ion microscopy is used to investigate the interaction between electromagnetic radiation and the surface of $YBa_2Cu_3O_{7-y}$ single crystals. It is shown that this action leads to the formation of a thin molten film on the surface of the sample, followed by the appearance of wave-like instabilities. Complexes of point defects, predominantly vacancies, similar to depleted zones, form in the bulk of the material.
[S1063-7850(98)01301-9]

The synthesis and development of complex multicomponent compounds, including high-temperature superconducting (HTSC) materials, and the unique properties associated with them, requires a more detailed study of how these materials are influenced by radiation and other external effects. This may be an important method of explaining the critical superconductivity parameters, as well as giving photoinduced and radiation control of their properties and parameters. We are familiar with various studies in which laser irradiation has changed the electrical conductivity and induced a superconducting transition,[1] has been used to vary the superconducting characteristics of HTSC films in a controlled fashion in a certain energy density range,[2] and has appreciably increased the critical currents.[3,4]

An investigation of the interaction between electromagnetic radiation and the surface of HTSC materials by field-ion microscopy may provide unique information on the structural changes in the crystal lattice at the level of individual atoms, on the kinetics of field-induced evaporation of the surface atomic layers under the action of single laser pulses, and on the spectrum of surface and bulk defects. Such investigations are reported here. Studies of radiation defects in Y–Ba–Cu–O single crystals by field ion microscopy were reported earlier in Ref. 5.

A special assembly was constructed for this purpose, comprising a field-ion microscope, a pulsed neodymium laser ($\lambda = 1060$ nm, $\tau = 20$ ns), an alignment laser, and a cassette containing removable filters to vary the sample irradiation intensity. The intensity was determined to be $I \sim 3 \times 10^8$ W/cm^2 by trial and error. The samples for the field-ion microscopic analyses were prepared from $YBa_2Cu_3O_{7-y}$ single crystals which were cleaved into small fragments and the sharpest fragments attached to tungsten needle-substrates with an electrically conducting adhesive.[6] This adhesive was a suspension of graphite powder in acetone.

The samples were irradiated in two regimes. In the first, after the voltage giving the best image had been reached and the characteristic surface structure of the sample recorded on photographic film, the sample voltage was reduced so that only weak luminescence was observed on the microscope screen. The tip of the sample was then subjected to laser irradiation. As a result, the brightness and area of the image increased abruptly, denoting a newly formed surface relief. In this regime, the sample voltage remained constant (Fig. 1). This effect may be attributed to sharpening of the sample tip as it is pulled into the field (thermofield rearrangement-sharpening effect).[7,8]

In the second regime, the samples were irradiated at the voltage of the best image without reducing the potential. In this case, the sample was either damaged or the field evaporated an appreciable number of the surface atomic layers, activated by the laser radiation. The pattern resembled damage to the sample as a result of the ponderomotive forces of the electric field (Fig. 2).

When analyzing the results of these experiments, the following factors must be borne in mind: the vacuum insulation, the cryogenic cooling, the high electric field, and the small size of the sample. Recently published experimental data[9] suggests that these newly formed ordered structures may be arbitrarily divided into two groups. The first group includes strictly periodic gratings formed on the surface of solids as a result of nonuniform heating in the irradiation zone. The second group may include the relief structures formed as a result of uniform heating.[10] Having in mind the very small size of the surface under study (and the sample), we can assert that the material was uniformly heated. The presence of a high-intensity electric field above the molten surface of the emitter leads to the formation of wave-like instabilities,[11] with predominantly short-wavelength perturbations appearing on the surface. Their wavelength was determined directly from the field-ion images as approximately 10–15 nm. Taking into account the results of Ref. 7, we can postulate that the buildup of these instabilities is a stepwise process: various spheroidal or conical microprotuberances are initially formed on the surface of the liquid, they are then abruptly pulled into peaks with decreasing radius as a result of localization of the electric field at the roughnesses formed, before being instantaneously frozen.

In accordance with Ref. 12, a small perturbation of the liquid on the side of the applied electric field causes a vertical displacement of the surface atoms. In this case, an additional negative pressure, directed along the normal to the surface, acts on the surface of the liquid. In the absence of an

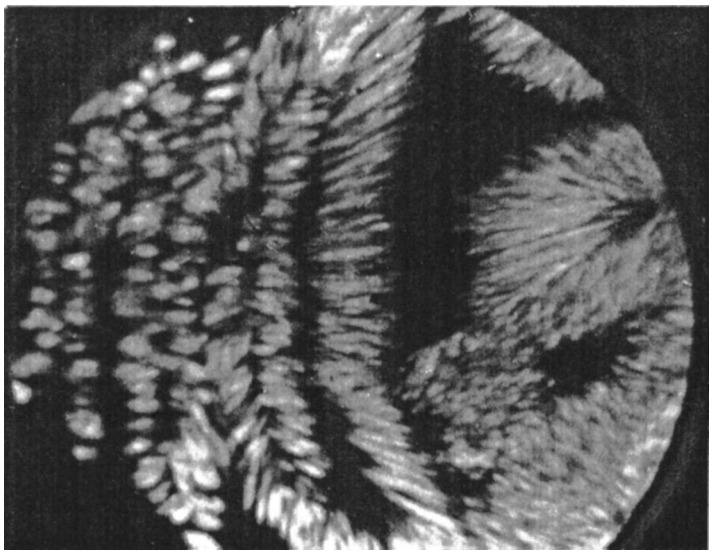

FIG. 1. Field-ion image of the surface of a $YBa_2Cu_3O_{7-y}$ single crystal after exposure to pulsed laser radiation. Sample potential $U_0 = 9.0$ kV.

electric field, only surface tension forces act on the molten tip of the sample. In a field, the initial perturbation destroys the pressure balance and increases the negative pressure, which then intensifies the perturbation, and so on.[7]

Field-ion microscopic examinations of $YBa_2Cu_3O_{7-y}$ single crystals after exposure to laser pulses revealed that the newly formed surface is not very sensitive to the applied field. It was observed visually that a small increase in the potential on the sample was only accompanied by enhanced brightness of the image on the screen, without making any significant changes to the overall contrast of the image. An appreciable increase in voltage, by 15–20% of the initial value, was required to evaporate the surface amorphized layer. The method of field-induced evaporation was used to make a field-ion microscope analysis of the bulk structure of high-temperature superconductors, at a depth of several tens of atomic layers. A typical microscope contrast is shown in Fig. 3. Considerable structural changes take place in the bulk, resulting in the complete absence of a crystal structure, the formation of small vacancy clusters in the surface layer, preferentially depleted zones. The main factors in the action of the pulsed laser radiation in this case are the thermal and impact loading on the surface of the material. As a result, large numbers of isolated vacancies are generated in the bulk of the samples, which may promote the formation of vacancy clusters and pores. It should also be borne in mind that, at the instant of the laser irradiation, a strong electric field is present at the surface of the sample which may displace atoms from their normal positions in the crystal lattice.[13] This factor may have a substantial influence on the damage caused to the crystal lattice in the bulk of the material. A series of field-ion microscope images was used to assess the linear dimensions of the defect zones, taking into account the results of Ref. 14. The right-hand part of the image (Fig. 3) reveals several closely spaced defect zones which, subject to certain assumptions, may be identified as pores with linear dimensions of 5–10 nm. At the same time, it is quite logical to assume that these pores are artifacts, specifically, the consequence of field etching of depleted zones. No unambiguous conclusion can be reached on the basis of these results. It may also be postulated that the formation of defect zones under the action of laser pulses is caused by the high mobil-

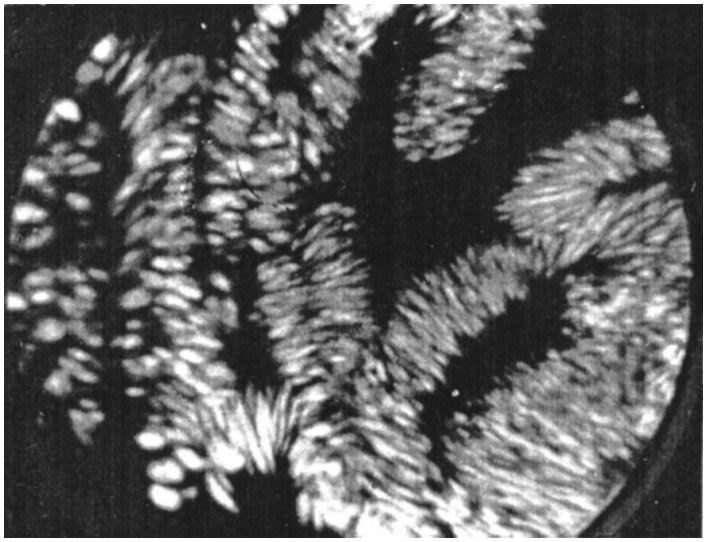

FIG. 2. Field-ion image of the surface of a $YBa_2Cu_3O_{7-y}$ single crystal after the next laser pulse (see text). $U_0 = 12.0$ kV.

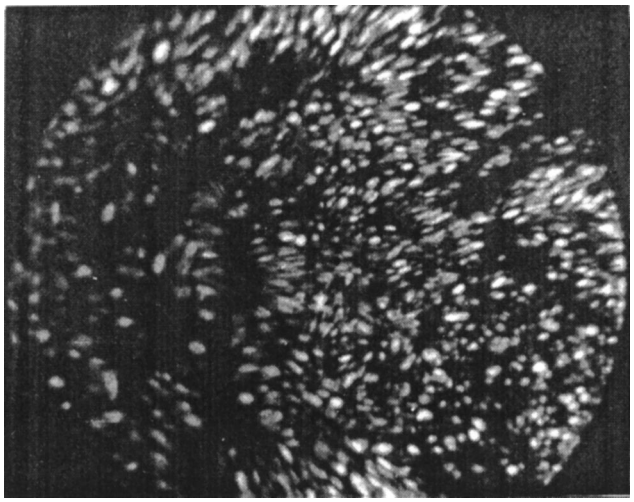

FIG. 3. Field-ion image of the surface of a $YBa_2Cu_3O_{7-y}$ single crystal after field evaporation of several tens of atomic layers. $U_0 = 15.0$ kV.

ity of the oxygen atoms in the CuO_4 base plane, and also by the weak bonding of the barium atoms in the crystal lattice.[15,16] In this case, the observed defect zones correspond to cascades of atom–atom displacements.

To sum up, when $YBa_2Cu_3O_{7-y}$ single crystals are exposed to laser pulses of intensity $I \sim 3 \times 10$ W/cm^2, a thin molten film forms on the surface followed by the appearance of wave-like instabilities. The surface is damaged, loses its superconducting structure, and becomes less sensitive to the evaporating field. Complexes of point defects, predominantly vacancies, having parameters similar to depleted zones, form in the bulk of the material.

[1] A. I. Kirilyuk, N. M. Kreĭnis, and V. I. Kudinov, JETP Lett. **52**, 49 (1990).
[2] M. L. V'yukov, A. A. Komarnitskiĭ, and A. I. Frolov, Sverkhprovodimost' (KIAE) **2**(12), 108 (1989).
[3] I. G. Gorol'chuk, A. G. Ul'yashin *et al.*, Sverkhprovodimost' (KIAE) **3**, 2616 (1990).
[4] A. L. Mikhaĭlichenko, G. N. Mikhaĭlova *et al.*, Kvant. Elektron. (Moscow) **26**, 715 (1996).
[5] G. G. Kuzyakhmetov and A. L. Suvorov, Pis'ma Zh. Tekh. Fiz. **21**(14), 31 (1995) [Tech. Phys. Lett. **21**, 551 (1995)].
[6] A. J. Melmed, J. Phys. (Paris), Colloq. **49**, Colloq. 6, 67 (1988).
[7] M. D. Gabovich, Usp. Fiz. Nauk **140**, 137 (1983) [Sov. Phys. Usp. **26**, 447 (1983)].
[8] V. N. Shrednik, Rost. Kristall. **13**, 68 (1980).
[9] S. A. Akhmanov, V. I. Emel'yanov, N. I. Koroteev, and V. N. Seminogov, Usp. Fiz. Nauk **147**, 675 (1985) [Sov. Phys. Usp. **28**, 1084 (1985)].
[10] V. I. Emel'yanov, E. M. Zemskov, and V. I. Seminogov, Kvantovaya Elektron. (Moscow) **11**, 2283 (1984) [Sov. J. Quantum Electron. **14**, 1515 (1984)].
[11] S. V. Zaĭtsev and A. L. Suvorov, Zh. Tekh. Fiz. **60**(9), 156 (1990) [Sov. Phys. Tech. Phys. **35**, 1097 (1990)].
[12] L. D. Landau and E. M. Lifshitz, *Electrodynamics of Continuous Media* (Pergamon Press, Oxford, 1960; Gostekhizdat, Moscow, 1957).
[13] E. W. Müller and T. T. Tsong, *Field Ion Microscopy: an Introduction to Principles, Experiments, and Applications* (American Elsevier, New York, 1969; Metallurgiya, Moscow, 1972).
[14] A. L. Suvorov and A. G. Sokolov, Kristallografiya **20**, 379 (1975) [Sov. Phys. Crystallogr. **20**, (1975)].
[15] I. Yu. Bezotosnyĭ, V. F. Elesin *et al.*, Sverkhprovodimost' (KIAE) **5**, 835 (1994).
[16] V. I. Gatal'skaya, G. V. Gatal'skiĭ *et al.*, Izv. Ross. Akad. Nauk, Ser. Fiz. **59**(**10**), 164 (1995).

Translated by R. M. Durham

Influence of triboelectric treatment on the coercivity of magnetic films

A. Yu. Toporov, V. A. Klyuev, and M. V. Valeĭko

Institute of General Physics, Russian Academy of Sciences, Moscow; Institute of Physical Chemistry, Russian Academy of Sciences, Moscow

(Submitted September 6, 1996; resubmitted March 10, 1997)
Pis'ma Zh. Tekh. Fiz. **24**, 73–78 (January 12, 1998)

A study has been made to determine how the properties of magnetic films are influenced by the triboelectric fields accompanying the polishing of articles with fur and results are presented. For insulating films of bismuth-containing iron garnet an increase in the coercivity was observed, evidently caused by the electromagnetic effect, in spite of reduced defects in the crystal structure. © *1998 American Institute of Physics.* [S1063-7850(98)01401-3]

It is known that the triboelectric fields generated as a result of the friction between insulators in a vacuum may lead to electrical erosion of the contacting surfaces. For a specific configuration of friction pair, electrical erosion smoothing of the surface is observed and this has served as the basis for a new method of treating the surfaces of insulators and semiconductors—triboelectric polishing.[1] In this method of treatment the surface of the article being treated is exposed to the action of a soft fleecy material attached to the cylindrical surface of a rapidly rotating roller.

Special experiments have shown that the triboelectric fields generated in vacuum are so large that they not only smooth the microrelief by electrical erosion to levels unattainable by other known methods of polishing, but they also modify the structure, particularly the defect structure of the surface layers of the materials being treated.[2]

A reduction in structural defects after this treatment has been observed for many insulating and semiconductor materials (such as glass, quartz, and silicon). Moreover, the reduction in defects detected by field emission and double-crystal radioscopy, especially for silicon wafers treated by the triboelectric technique, was also observed when these were used to fabricate semiconductor devices, which then showed improved properties in factory tests.[2]

The mechanism responsible for these reduced defects is attributed to the action of high-intensity electric fields on the material. In the case of insulating magnetic materials, this reduction in defects should lead to reduced coercivity.[3]

Since a specific change in the magnetic properties of materials is extremely important for engineering, we set ourselves the task of determining whether the coercivity of magnetic films could be changed by triboelectric treatment.

The influence of triboelectric treatment was investigated using Bi-containing easy-plane iron garnet films grown by liquid-phase epitaxy on (III)-oriented gallium gadolinium garnet substrates. The thickness of the films was 1–4 μm.

The triboelectric treatment was carried out using a roller coated with soft natural fur (to reduce the mechanical action on the film) which was in very light contact with the surface of the film. The sliding velocity of the fur on the surface of the film was 13 m/s. The treatment time did not exceed 1 h.

The change in the magnetic properties under the influence of the triboelectric treatment was assessed from the change in the coercivity of the film material. The coercivity was determined by a magnetooptic method using the Faraday effect. Hysteresis loops of the films were recorded in the initial state and after the triboelectric treatment using a system described in Ref. 4.

The investigations showed that under the influence of the triboelectric treatment, the coercivity of the sample material

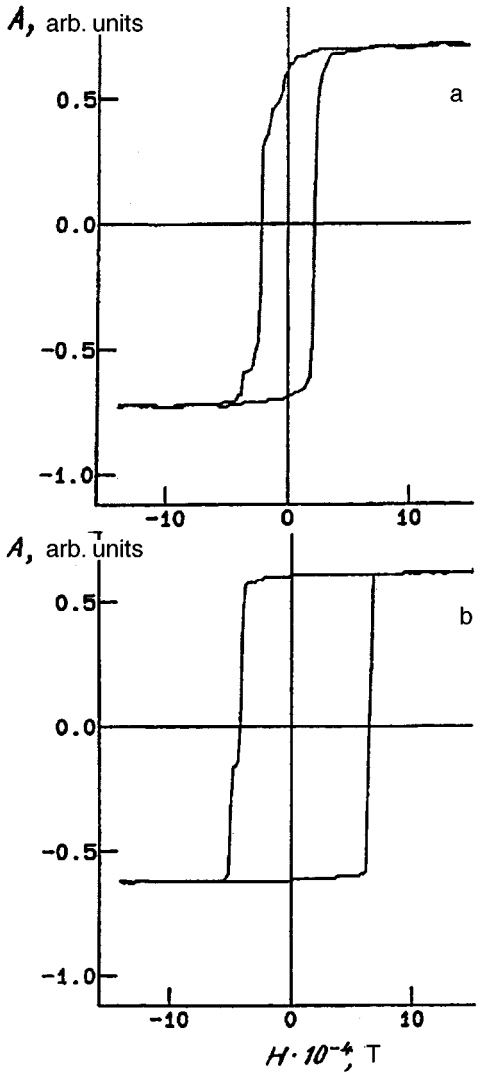

FIG. 1. Magnetic reversal curves of Bi-containing iron garnet film along the easy magnetization axis before (a) and after triboelectric treatment (b).

 1063-7850/98/010033-03$15.00

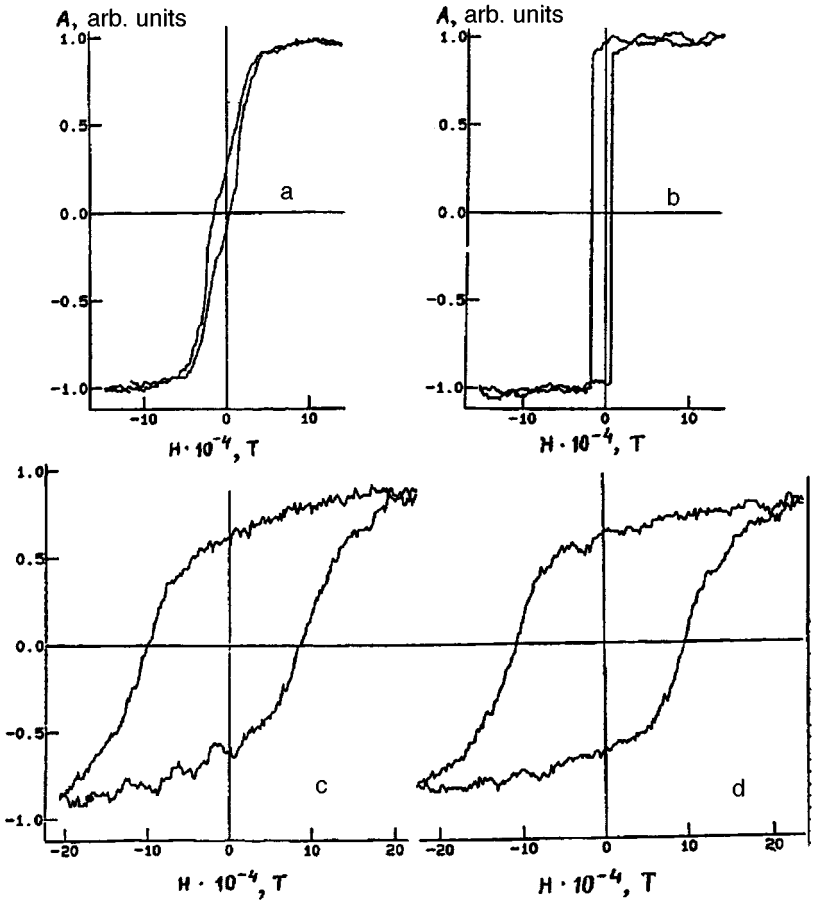

FIG. 2. Magnetic reversal curves of FeCoNiSiB film along the easy (a, c) and difficult magnetization axes (b, d) before (a, b) and after triboelectric treatment (c, d).

changes substantially. Generally, the coercivity increases. Triboelectric treatment leads to a significant change in the profile of the hysteresis loop, which becomes broader and more rectangular. By way of an example Fig. 1 shows hysteresis curves of the magnetic reversal curves of Bi-containing iron garnet films 2 μm thick before and after triboelectric treatment. An analysis of the profile of the hysteresis loops indicates that the in-plane anisotropy of the magnetic properties of the material is conserved. After triboelectric treatment some reduction in the crystal structure defects is observed.

It should be noted that this result is only observed when the triboelectric treatment process is carried out in high vacuum ($>10^{-4}$ mm Hg). Under the same friction conditions in air, no significant change in the coercivity is observed. This is because the electrification process is more intensive in vacuum and is accompanied by the generation of higher-power electric fields compared with the friction process in air.

Thus, the experiments have shown that, despite the observed decrease in structural defects in these Bi-containing iron garnet films, triboelectric treatment is in fact accompanied by increased coercivity. Since the temperature of the samples during polishing did not exceed 80 °C, the influence of heating on changes in the magnetic characteristics of these films can be neglected.

An obvious explanation for the observed increase in coercivity may be the appearance of a magnetoelectric effect[5] caused by the films attaining an electret state and electric fields being induced in the bulk.

The injection of electric charges into the bulk of the film during friction, capture of these charges by trap defects, and the drift of charged defects toward the film–substrate interface has the result that, even after the friction process has ended, an internal electric field is conserved in the bulk of the film, and this is responsible for the magnetoelectric effect. Note that the previously observed change in the coercivity of Bi-containing iron garnet films following their treatment in a corona discharge was also explained by the magnetoelectric effect.[6] It should be stressed the purely mechanical action of the fur on the surface during the triboelectric treatment can only be discounted for fairly hard materials, such as Bi-containing iron garnet films. For softer and more electrically conducting materials, the mechanical effect may have an important influence. A clear example may be provided by the results of using a rotating roller to treat films of an amorphous magnetic substance having the general composition FeCoNiSiB deposited by laser evaporation on the surface of glass and silicon substrates using a method described in Ref. 4 (the film thickness was 10–1000 Å).

Figure 2 shows the hysteresis curves before and after treatment of a film 1000 Å thick. It can be seen that the coercivity also increases in this case. Since conversion to an electret state and the formation of an internal electric field do not take place in conducting materials, and an analysis of the hysteresis curves suggests that defects in the film are in-

creased, the change in coercivity is evidently caused by purely mechanical action on the surface of the film. This is also evidenced by the complete disappearance of anisotropy (the hysteresis loops are isotropic in the easy and difficult axes).

Thus, the change in the magnetic properties observed in this case is caused by the appearance of additional defects as a result of the friction between the films and the fur, which increases the pinning of the domain walls.

It should be noted that triboelectric treatment cannot generally be applied to the surfaces of conducting materials. No electrical erosion polishing can be achieved in this case and the surface layers of the treated articles show no reduction in structural defects.

On the whole, the results have shown that when triboelectric treatment is used to alter the magnetic properties of insulators and semiconductors, allowance must be made for their conversion to the electret state which gives rise to the magnetoelectric effect.

This work received considerable financial support from the Russian Fund for Fundamental Research, Grant No. 95–03–04766.

[1] V. A. Klyuev *et al.*, USSR Author's Certificate No. 643302 Int. Cl. B241; Byull. Otkr. Izobret. No. 3, 45 (1979).
[2] V. A. Klyuev, M. A. Kolobov, Yu. P. Toporov *et al.*, Élektron. Prom. No. 7, 46 (1991).
[3] D. D. Mishin, *Magnetic Materials* [in Russian], Vysshya Shkola, Moscow (1991).
[4] P. I. Nikitin, M. V. Valeĭko, A. M. Gorbanadze *et al.*, Kvant. Elektron. (Moscow) **23**, 383 (1996).
[5] L. D. Landau and E. M. Lifshitz, *Electrodynamics of Continuous Media* (Pergamon Press, Oxford, 1960; Gostekhizdat, Moscow, 1957)
[6] V. G. Kostishin and L. M. Letyuk, Zh. Tekh. Fiz. **65**(7), 179 (1995) [Tech. Phys. **40**, 930 (1995)].

Translated by R. M. Durham

Release of hydrogen from an insulating liquid under the action of ultrasound

G. M. Mikheev, Gr. M. Mikheev, G. P. Nekryachenko, and I. P. Gotlib

Institute of Applied Mechanics, Ural Branch of the Russian Academy of Sciences, Izhevsk; ''Chuvashénergo'' Company, Cheboksary

(Submitted June 5, 1998)
Pis'ma Zh. Tekh. Fiz. **24**, 79–84 (January 12, 1998)

Coherent anti-Stokes light scattering spectroscopy is used to study the release of hydrogen from an insulating liquid under the action of focused ultrasound which causes mixing of the liquid to form a fountain. It is shown that the action of ultrasound on an insulating liquid in an evacuated volume or in normal-pressure air substantially accelerates the desorption of hydrogen into the gas phase. © *1998 American Institute of Physics.* [S1063-7850(98)01501-8]

The amount of hydrogen in solids may be measured by extracting it in the gas phase by heating and melting.[1–3] The content of gases, including hydrogen, in liquids may be determined by releasing dissolved gases from the liquid phase into the gas phase at reduced ambient pressures.[4] In Ref. 5 it is suggested that gas may be extracted from a liquid by convection produced by microwave irradiation of the liquid. In the diagnostics of power transformers the gas content in a sample of insulating liquid (transformer oil) is usually determined by direct vapor-phase analysis. This method involves transferring some of the dissolved gas into an inert atmosphere above the liquid by periodic shaking[6] until thermodynamic equilibrium is established and then analyzing the gas mixture with a chromatograph.

Here we demonstrate that the process of hydrogen release from an insulating liquid can be speeded up considerably under the action of focused ultrasound. This is of interest for the development of methods for rapid analysis of gas content, in transformer oils for instance.

It is known that losses of ultrasonic energy in a medium lead to the appearance of a so-called radiation force.[7] Under the action of this force, jets of liquid (a fountain) may appear above the focal region of a spherical ultrasonic emitter. This causes vigorous mixing and degassing of the liquid. In addition, when the ultrasound is focused, the amplitude of the acoustic pressure is spatially nonuniform (graded). Gas bubbles in the field of such an acoustic wave are subjected to the Bjerknes force[8] given by $F_B = -\langle V \nabla P \rangle$, where V and P are the instantaneous values of the bubble volume and acoustic pressure, and averaging is performed over time within the period of the oscillations. The action of this force causes spatial displacement (migration) of the bubbles into zones of elevated pressure.[9,10] For the case of a focused ultrasound beam, the region of elevated pressure is situated near the focus of the emitter. Consequently, gas inclusions exposed to the action of the Bjerknes force near the focus of an ultrasonic emitter will be expelled into the surrounding atmosphere together with the fountain, which may lead to even more efficient degassing of the liquid. However, the action of fairly high-power acoustic waves may give rise to various acousto-chemical reactions,[11] including decomposition of the insulating liquid to form hydrogen, methane, ethane, and so on.[12] For this reason, insulating liquids should be degassed at low ultrasound powers.

This method of degassing a liquid was checked out experimentally using the apparatus shown schematically in Fig. 1. A spherical piezoceramic transducer *1* attached to a conducting mount *2* and a glass container *3*, excites acoustic oscillations in the liquid *4* under the action of a resonant rf voltage (~27 V, 1.76 MHz). The ultrasound propagating in the liquid is focused at its surface and generates a fountain *5*, which then decays into fine droplets. The gas released from the liquid is fed via a connecting tube *6* to an optical measuring cell *7* with optical windows *8* and is recorded at a specific repetition frequency by coherent anti-Stokes light scattering using resonant biharmonic laser pumping based on stimulated Raman light scattering.[13,14] This method of recording hydrogen in a gas mixture is selective and, unlike

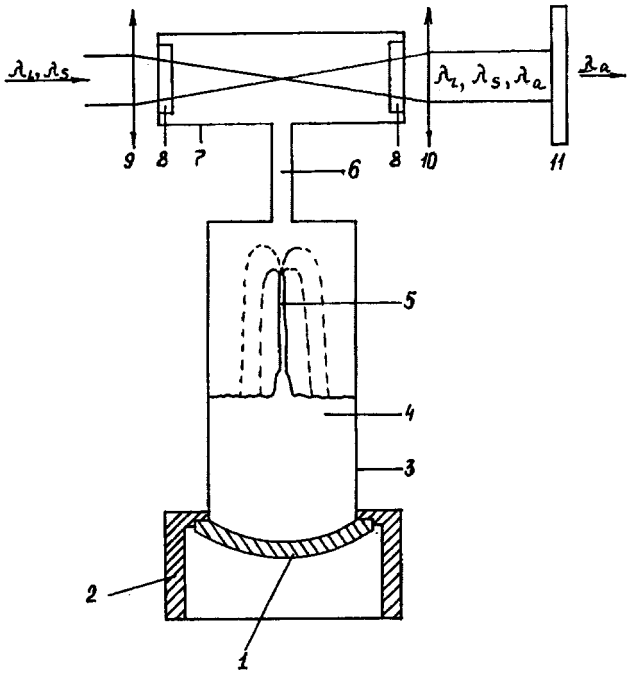

FIG. 1. Schematic of experiment: *9*—lens to focus biharmonic pump radiation λ_L, λ_S ($\lambda_L = 532$ nm, $\lambda_S = 683$ nm), tuned to the $Q_{01}(1)$ vibrational transition frequency of molecular hydrogen; *10*—collimating lens, *11*—optical filter to select anti-Stokes scattering component λ_a ($\lambda_a = 436$ nm), generated by coherent anti-Stokes scattering of light, whose intensity can be used to assess the hydrogen concentration in the measuring cell (the remaining notation is given in the text.)

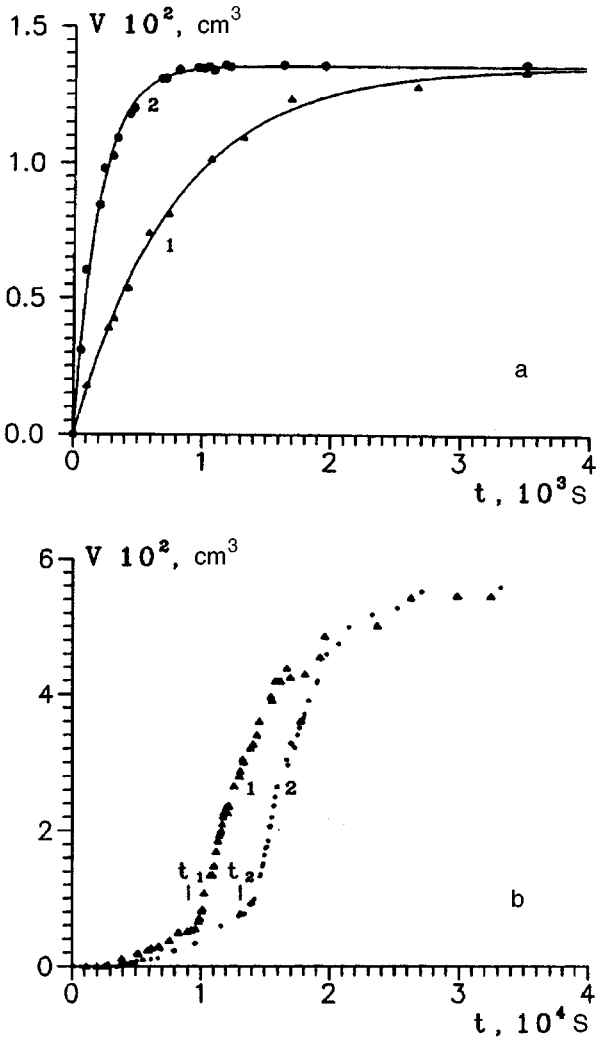

FIG. 2. Volume V of hydrogen released from GK-grade prehydrogenated transformer oil as a function of time t in vacuum with a residual air pressure of 100 Pa (a) (*1*—spontaneous desorption, *2*—desorption under the action of ultrasound) and in normal-pressure air (b).

chromatography, allows the kinetics of the gas release from the liquid phase to be observed in real time.

The effective ultrasonic power N coupled into the liquid was estimated from the law of energy conservation using the following formula: $N=(\pi/8)\rho d^2(2gh)^{3/2}$, where ρ is the liquid density, g is the free-fall acceleration, h is the height of the fountain, and d is the average diameter of the jet. For $d=1.5$ mm, $h=0.15$ m, and $\rho=880$ kg/m^3 we then obtain $N=4$ mW. At the focus of the transducer *1*, the power density of the ultrasound is then 220 mW/cm^2. This ultrasound power does not stimulate chemical decomposition reactions in the insulating liquid. Experiments showed that the action of this ultrasound power for 180 min on 40 ml of various grades of degassed transformer oil was not accompanied by any decomposition to form hydrogen at normal pressure or in vacuum.

Figure 2 shows the kinetics of hydrogen release from transformer oil after this had been preliminarily hydrogenated. Here V is the volume of gaseous hydrogen reduced to normal conditions. The results plotted in Fig. 2a were obtained after accelerated hydrogen saturation of the oil under mixing conditions, whereas those in Fig. 2b were obtained for natural diffusion of low-pressure hydrogen into the oil over a period of days. It can be seen that spontaneous desorption of gas over a certain time t may take place in vacuum (Fig. 2a, curve *1*). Under these conditions, the action of the ultrasound appreciably accelerates the gas release process (Fig. 2a, curve *2*). The experimental dependences of the gas release $V(t)$ plotted as a series of points in Fig. 2a are accurately described by the function $V=V_0(1-\exp(-t/\tau))$, where V_0 is the reduced volume of the initial hydrogen contained in the oil, and τ is the characteristic gas release time, which is reduced by a factor of 3.9 when the ultrasound is switched on. At normal pressures in air, the process of hydrogen desorption from the oil is substantially slower (Fig. 2b, initial section of curve *1*). However, the application of ultrasound at $t=t_1$ abruptly increases the rate of gas release. Delaying the time of application of the ultrasound to t_2 shifts the dependence $V(t)$ to the right on the time scale (Fig. 2b, curve *2*). An appreciable change in the rate of increase in $V(t)$ in air is observed after certain delay following the application of the ultrasound. Experiments have shown that this can be attributed to the finite time t_D required for hydrogen to diffuse in air along the connecting tube *6* to the optical measuring cell *7* (Fig. 1). As the air pressure decreases, t_D tends to zero.

It has thus been demonstrated experimentally that low-power focused ultrasound can be successfully used to speed up the release of hydrogen and other gases from liquid insulators in a gaseous atmosphere.

The authors are grateful to N. B. Kuznetsov, T. N. Mogileva, and E. G. Fateev for technical assistance with the work.

[1] V. I. Shapovalov and V. V. Trofimenko, *Flaking and Hydrogen Monitoring in Steel* [in Russian], Metallurgiya, Moscow (1987).
[2] G. M. Mikheev, D. I. Maleev, E. S. Makhev *et al.*, Zh. Prikl. Spektrosk. **60**, 11 (1994).
[3] O. I. Kon'kov, I. N. Kapitonov, I. N. Trapeznikova *et al.*, Pis'ma Zh. Tekh. Fiz. **23**(1), 3 (1997) [Tech. Phys. Lett. **23**, 9 (1997)].
[4] V. G. Arakelyan, Electrotehnica No. **2,** 8 (1994).
[5] B. G. Emets, Pi'ma Zh. Tekh. Fiz. **22**(8), 22 (1996) [Tech. Phys. Lett. **22**, 313 (1996)].
[6] B. V. Ioffe, M. I. Kostkina, and A. G. Vitenberg, Zh. Prikl. Khim. **53**, 2280 (1980).
[7] O. V. Rudenko, Vestn. Mosk. Univ. Fiz. Astron. No. **6**, 18 (1996).
[8] L. A. Crum, J. Acoust. Soc. Am. **57**, 1363 (1975).
[9] É. M. Agrest and G. N. Kuznetsov, Akust. Zh. **18**, 168 (1975) [Sov. Phys. Acoust. **18**, (1975)].
[10] T. V. Makarova and E. A. Gubernatorova, Akust. Ul'trazvukov. Tekh.: Resp. Mezhved. Nauch.—Tekh. Sb., No. 26, 15 (1991).
[11] M. A. Margulis, *Principles of Acoustochemistry* [in Russian], Vysshaya Shkola, Moscow (1984).
[12] V. G. Arakelyan, L. A. Dar'yan, and A. K. Lokhanin, Élektrichestvo, No. 5, 33 (1988).
[13] G. M. Mikheev and Gr. M. Mikheev, Élektrichestvo, No. 6, 33 (1996).
[14] G. M. Mikheev and T. N. Mogileva, Kvant. Elektron. (Moscow) **23**, 943 (1996).

Translated by R. M. Durham

Use of a transverse nanosecond discharge at the prebreakdown electron ionization multiplication stage for selective excitation of neon atoms

A. K. Shuaibov

Uzhgorod State University
(Submitted June 3, 1997)
Pis'ma Zh. Tekh. Fiz. **24**, 85–90 (January 12, 1998)

An investigation is made of the characteristics of a transverse nanosecond discharge in Ne/SF_6 and $He/Ne/SF_6$ mixtures at the prebreakdown electron ionization multiplication stage. The conditions needed to obtain a stable transverse discharge with ultraviolet spark preionization are studied as well as the spectral and temporal characteristics of the plasma radiation. It is shown that this transverse discharge burning regime may be promising for the selective excitation of neon atoms which may be used to develop an electric-discharge, $\lambda = 585.3$ nm, Ne($3s-3p$) plasma laser. © *1998 American Institute of Physics.* [S1063-7850(98)01601-2]

When a conventional high-current transverse discharge obtained in $He/Ne/H_2$ mixtures at moderate pressures ($P = 10-20$ kPa) is used to pump $\lambda = 585.3$ nm NeI plasma lasers, the efficiency is poor.[1,2] This is because the transverse discharge plasma contains no high-energy electrons and the impedances of the pump source and the transverse discharge are mismatched. The addition of electronegative molecules (NF_3, $P = 3-4$ kPa) to He and Ne atoms increases the output energy of a transverse-discharge-pumped laser by an order of magnitude but the pulse length does not exceed 10–20 ns and the main mechanism for filling of the upper active state is direct electron impact.[3,4] The use of discharges with a hard current component,[5] longitudinal discharges, and hollow-cathode discharges[6] increases the duration of the lasing by incorporating recombination mechanisms for filling the $3p$ states of NeI but the scope for spatial scaling of the volume of the laser active medium is limited for these methods of pumping.

Here, an investigation is made of the characteristics of a transverse discharge with ultraviolet spark preionization, initiated at the stage of prebreakdown ionization multiplication of electrons, in order to produce a collisional nonequilibrium plasma in Ne/SF_6 and $He/Ne/SF_6$ mixtures. It was suggested that SF_6 molecules used previously to obtain lasing on $3s-3p$ NeI transitions in the red could be used to depopulate the lower active state of neon.[7] It was shown in Ref. 8 that a volume discharge in an $He/Kr/F_2$ mixture has a stable stage with prebreakdown ionization multiplication, which is promising for obtaining 249 nm lasing in KrF*. The possibilities for achieving this type of discharge in the active medium of a neon-atom plasma laser were not investigated. A discharge at the prebreakdown ionization multiplication stage develops under conditions where the electric field strength at the electrodes is fairly high over the entire energy deposition time and is characterized by a plasma electron density of $10^{12}-10^{13}$ cm^{-3}. This makes it similar to an electron-beam-controlled discharge but the electron density is sufficient to obtain an inversion at $\lambda = 585.3$ nm in NeI.

A transverse discharge with prebreakdown ionization multiplication was investigated in the emitter of a laser diagnostic complex, described in Ref. 9. The discharge was ignited in an electrode system 18 cm long, where the radius of curvature of the working surface was 1.7 cm. The width of the discharge region was 0.7 cm. Preionization was provided using two spark lines mounted on either side of the cathode. A pulsed voltage generator was formed by an LC system with a 30 nF main storage capacitor and a 9.4 nF peaking capacitor. The switch was a TGI1 1000/25 thyratron. The transverse-discharge current and voltage pulses were measured with a Rogowski loop and a low-inductance capacitive voltage divider. The plasma radiation spectra were investigated using an MDR-2 monochromator, a Foton photomultiplier, an electrical system for recording low-repetition-frequency radiation pulses, and a KSP-4 automatic plotter. The temporal characteristics of the transverse-discharge radiation were recorded with an ÉLU14-FS linear electron multiplier and 6LOR-04 or S1-79 oscilloscopes. At Ne/SF_6 and $Ne/Ne/SF_6$ mixture pressures in the range 5–200 kPa, ignition of the high-current diffusive transverse discharge was preceded by a stable, spatially uniform, yellow discharge with a 0.7×2.2 cm aperture in a narrow range of supply voltages $\Delta U = \pm 0.5$ kV. The coefficient of plasma

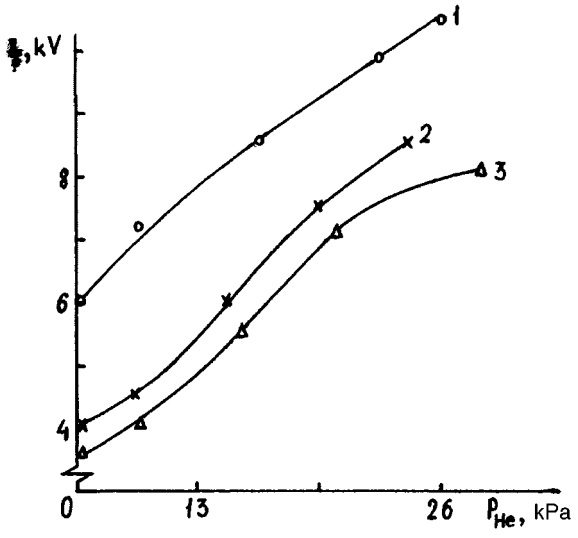

FIG. 1. Burning voltage of transverse discharge at prebreakdown ionization multiplication stage as a function of gas mixture pressure and composition: *1*—$Ne/SF_6 = 32/1.6$ kPa, *2*—20/0.8 kPa, and *3*—10/0.8 kPa.

 1063-7850/98/010038-03$15.00

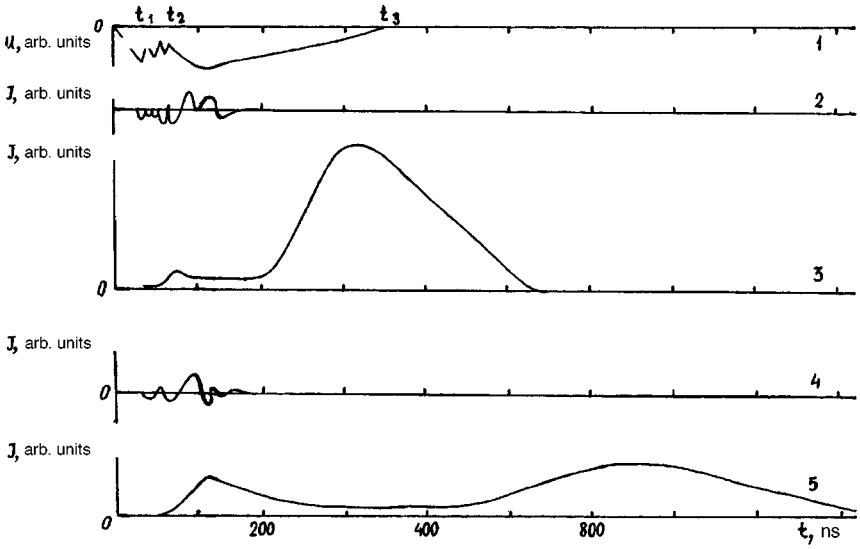

FIG. 2. Oscilloscope traces of current, voltage, and radiation pulses for a $\lambda = 585.3$ nm NeI transverse discharge at the prebreakdown ionization multiplication stage, ignited in $Ne/SF_6 = 60/0.8$ kPa (*1–3*) and 166/0.4 kPa mixtures (*4, 5*).

filling of the interelectrode gap was unity, which was substantially higher than its value ($k = 0.5-0.7$) in a high-current transverse discharge in the active media of a XeCl* laser. This value of k is similar to the coefficients for a transverse discharge with anisotropic resistive electrodes,[10] which makes it promising to use a transverse discharge with prebreakdown ionization multiplication in wide-aperture emitters. A study of the overall radiation spectra of a transverse discharge with prebreakdown ionization multiplication in (He)/Ne/SF_6 mixtures has shown that in the yellow-red range, the main emission line is $\lambda = 585.3$ nm NeI with a contrast of 7–12 relative to the other lines on the $3s-3p$ NeI transitions.

Figure 1 gives the maximum transverse discharge burning voltage (U_f) at the prebreakdown ionization multiplication stage as a function of the pressure and composition of the (He)/Ne/SF_6 mixture. The optimum concentration of SF_6 molecules was in the range 0.5–1.0 kPa. As the SF_6 content and neon pressure in the binary mixture increased, the value of U_f and the energy characteristics of the transverse discharge increased. When the concentration of SF_6 molecules was increased appreciably ($\geqslant 1.6$ kPa), the uniformity of the ultraviolet preionization deteriorated and the discharge with prebreakdown ionization multiplication became unstable. The addition of He to the Ne/SF_6 mixture increased U_f but optimum densities of He atoms in a ternary mixture existed for the $\lambda = 585.3$ nm NeI radiation. The temporal characteristics of a transverse discharge with prebreakdown ionization multiplication in Ne/SF_6 mixtures are given in Fig. 2. After breakdown of the discharge gap, a high electric field strength is maintained at the electrodes. The voltage pulse consisted of a rapidly decaying section of U—$(0;t_1)$ corresponding to breakdown of the discharge gap, a section $(t_1;t_2)$ corresponding to quasi-steady-state burning when ionization attractive equilibrium is established, and the time interval $(t_2;t_3)$ corresponding to prebreakdown ionization multiplication. The profile of U as far as time t_2 was similar to a pulsed discharge in pure SF_6 in a system of metal electrodes with ultraviolet preionization.[11] The $\lambda = 585.3$ nm NeI radiation pulse consisted of an initial steady-state section of low amplitude, and a high-intensity second peak formed as a result of the complete decay of the voltage across the discharge gap (time t_3). The total duration of the radiation at the base of the oscilloscope trace was 1.0 μs. An increase in the neon pressure ($\geqslant 50-70$ kPa) caused a drop in the radiation intensity on this neon line and changed the ratio between the first and second peaks of the NeI radiation, increasing its duration ($\geqslant 1.0$ μs). It can be seen from Fig. 2, that recombination filling of the $3p$ NeI state takes place in this plasma. At the prebreakdown ionization multiplication stage, in a strong electric field excited neon atoms are generated, they undergo multistage ionization, and Ne^+ ions are converted to Ne_2^+ and $HeNe^+$ which then selectively fill the Ne($3p$) state as the parameter (E/N) decreases, as a result of recombination processes. The specific mechanism for filling of the upper state for the $\lambda = 585.3$ nm NeI transition in a breakdown discharge with prebreakdown ionization multiplication requires special study.

To sum up, it has been shown that in a breakdown discharge with prebreakdown ionization multiplication in He(Ne)/SF_6 mixtures at atmospheric pressure, a stable discharge is initiated for which the coefficient of filling of the interelectrode gap is unity, the spatial homogeneity is good, and the $3p$, $3s$ states of the neon atom are filled under nonequilibrium conditions. This behavior is of interest for the development of $\lambda = 585.3$ nm, NeI electric-discharge plasma lasers.

[1] M. I. Lomaev, A. N. Panchenko, and V. F. Tarasenko, Kvantovaya Elektron. (Moscow) **14**, 933 (1987) [Sov. J. Quantum Electron. **17**, 631 (1987)].
[2] G. A. Batyrbekov, É. G. Batyrbekov, V. A. Danilychev *et al.*, Kvantovaya Elektron. (Moscow) **16**, 2060 (1989) [Sov. J. Quantum Electron. **19**, 1325 (1989)].
[3] M. I. Lomaev and V. F. Tarasenko, Pis'ma Zh. Tekh. Fiz. **14**, 1045 (1988) [Sov. Tech. Phys. Lett. **14**, 460 (1988)].
[4] M. I. Lomaev and V. F. Tarasenko, Kvantovaya Elektron. (Moscow) **19**, 146 (1992) [Sov. J. Quantum Electron. **22**, 129 (1992)].
[5] E. L. Latush, M. F. Sém, and G. D. Chebotarev, Kvantovaya Elektron. (Moscow) **17**, 1418 (1990) [Sov. J. Quantum Electron. **20**, 1327 (1990)].
[6] V. B. Borisov, V. S. Egorov, M. N. Kirshin *et al.*, Opt. Spektrosk. **72**, 1064 (1992) [Opt. Spektrosk. **72**, 581 (1992)].

[7] V. M. Kaslin and G. G. Petrash, Zh. Prikl. Spektrosk. **12**, 540 (1970).
[8] V. M. Borisov, F. I. Vysikaĭlo, and O. B. Khristoforov, Kvantovaya Elektron. (Moscow) **12**, 1311 (1985) [Sov. J. Quantum Electron. **15**, 870 (1985)].
[9] A. K. Shuaibov, Yu. Yu. Neĭmet, A. I. Khodanich, and V. S. Shevera, Opt. Spektrosk. **75**, 713 (1993) [Opt. Spectrosc. **75**, 422 (1993)].
[10] M. A. Kanatenko, Zh. Tekh. Fiz. **64**(6), 198 (1994) [Tech. Phys. **39**, 627 (1994)].
[11] G. L. Spichkin, Zh. Tekh. Fiz. **56**, 1923 (1986) [Sov. Phys. Tech. Phys. **31**, 1150 (1986)].

Translated by R. M. Durham

Reflection of an electromagnetic wave by a layered superconductor-dielectric structure

A. G. Glushchenko and M. V. Golovkina

Volga Institute of Informatics, Radio Engineering, and Communications, Samara
(Submitted April 3, 1997)
Pis'ma Zh. Tekh. Fiz. **24**, 9–12 (January 12, 1998)

An analysis is made of the propagation of an electromagnetic wave through an infinite periodic superconductor-dielectric structure consisting of alternating layers of dielectric and thin layers of type II superconductor. The presence of thin layers of superconductor is taken into account by introducing a suitable boundary condition. It is observed that the reflection coefficient depends abruptly on the angle of incidence of the wave, the thickness of the superconducting film, and the external magnetic field. © *1998 American Institute of Physics.* [S1063-7850(98)00201-8]

The motion of a vortex structure in high-temperature superconductors may be utilized to amplify electromagnetic[1] and spin waves.[2,3] Periodic superconducting structures possess various fundamentally new properties compared with homogeneous materials, although they have not been used so far for wave amplification. We consider an infinite periodic structure consisting of dielectric layers of thickness d_1 separated by thin layers of type II superconductor of thickness t, where $t \ll \lambda$, where λ is the wavelength (Fig. 1). We direct the y axis perpendicular to the interfaces between the layers and the x axis parallel to the interfaces. The entire structure is situated in a magnetic field B_{y0} whose magnitude exceeds the first critical field for the superconductor, directed in the opposite direction to the y axis. Under the action of a transport current perpendicular to the field B_{y0} along the z axis, a network of Abrikosov vortices in the superconductor layers moves along the x axis. We consider the propagation of an H wave in the xy plane at the angle θ to the y axis. For simplicity, we shall assume that in the plane of the layers, the fields only depend on one coordinate and also that $\partial/\partial z = 0$.

The presence of a thin layer of superconductor of thickness $t \ll \lambda$, because of its small thickness, is best taken into account by introducing a special boundary condition. We consider a layer of superconductor at the boundary $y = 0$. In the instantaneous-response approximation and neglecting the elastic ''rigidity'' of the vortex lattice (the existence of elastic forces in the vortex network as this undergoes deformation leads to nonlinear coupling between the wave and the network, which is insignificant in this linear approximation), the boundary condition is written as follows:[2]

$$\frac{\partial B^y}{\partial t}(y=t) + \frac{j_{z0}\Phi_0}{\eta}\frac{\partial B_y}{\partial t}(y=t) = \frac{B_{y0}\Phi_0}{\eta t}\frac{\partial}{\partial x}[H_x(y=t) - H_x(y=0)], \tag{1}$$

where j_{z0} is the current density in the superconducting layer, η is the coefficient of viscosity of the magnetic vortex, and Φ_0 is the magnetic flux quantum.

We consider a single period of the structure, containing a single thin superconductor layer and a layer of dielectric. Its thickness is $d = d_1 + t$, where d_1 is the thickness of the dielectric layer. The boundary condition (1) may be written in the form of a matrix M_1 linking the fields at the boundaries $y = 0$ and $y = t$. The transformation matrix M_2 linking the fields at the end and beginning of the dielectric layer is known.[4] Then, the fields at the end of the period are related to those at the beginning by the matrix $M = M_1 \cdot M_2$. The dispersion relation for an infinite periodic medium is written in the form:[4]

$$\cos Kd = \frac{1}{2}(m_{11} + m_{22}), \tag{2}$$

where K is the Bloch wave number for the H-wave, m_{11} and m_{22} are the diagonal elements of the transition matrix M. The unknown dispersion relation for the H-wave is:

$$\cos Kd = \cos k_y d_1 + \frac{i\omega\mu_0 t}{2k_y B_y 0}\left(\frac{\eta}{\Phi_0} - \frac{j_{z0}k_x}{\omega}\right)\sin k_y d_1, \tag{3}$$

where $k_x = (\omega/c)\sqrt{\varepsilon\mu}\cos\theta$, and $k_y = (\omega/c)\sqrt{\varepsilon\mu}\sin\theta$. The fact that the Bloch wave number has an imaginary part indicates that the electromagnetic wave will decay exponentially as it propagates deep inside the periodic medium. However, if one of the conditions: $\sin k_y d_1 = 0$ or $\eta/\Phi_0 - (j_{z0}\cdot k_x)/\omega = 0$ is satisfied, the Bloch wave number becomes purely real and the electromagnetic wave may penetrate deep inside the periodic structure.

Figure 2 gives results of numerical calculations of the reflection coefficient R as a function of the angle of incidence θ for a structure consisting of a single layer of high-

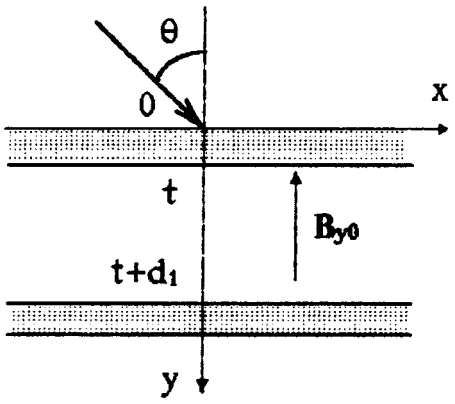

FIG. 1. Geometry of structure.

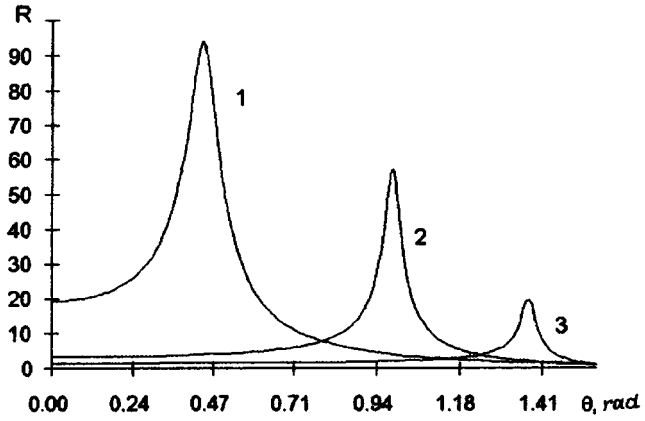

FIG. 2. Reflection coefficient R versus angle of incidence θ of electromagnetic wave for various thicknesses t of the superconducting layer: curve *1*—$t=44$ nm, curve *2*—$t=43$ nm, and curve *3*—$t=42$ nm. The parameters were: $B_{y0}=5$ T, $d=0.5$ μm, $\eta=10^{-8}$ N/s/m^2, $j_{z0}=10^8$ A/m^2, and $\omega=10^{10}$ Hz.

temperature superconducting ceramic $YBa_2Cu_3O_7$ of thickness t and a single layer of MgO dielectric of thickness d on a $SrTiO_3$ substrate. For this structure the reflection coefficient depends very strongly on the angle of incidence θ, the thickness of the superconducting film t, and the external magnetic field B_{y0}. An abrupt increase in the reflection coefficient R is observed when the condition $\mathrm{Re}(Z_{in})=-\omega\mu_0\mu_1/k_{y1}$ is satisfied which can be achieved by varying the input impedance Z_{in} of the layered structure over a wide range by varying B_{y0}, j_{z0}, and θ. This behavior of the reflection coefficient R is attributable to interaction between the electromagnetic wave and the moving network of Abrikosov vortices. For these structures an amplification effect is observed in magnetic fields B_{y0} of the order of 5 T although these fields do not exceed the upper critical field for $YBa_2Cu_3O_7$, which is estimated to be 30 T at $T=77$ K (Ref. 5).

In view of the high values of the reflection coefficient and the abrupt dependence of the reflection coefficient on the frequency of the incident wave, the angle of incidence, and the external magnetic field B_{y0}, these structures can be used to develop new magnetic-field-controlled devices with high parameter selectivity (in particular, amplifiers and filters).

[1] A. G. Glushchenko, Pis'ma Zh. Tekh. Fiz. **17**(22), 11 (1991) [Sov. Tech. Phys. Lett. **17**, (1991)].
[2] A. F. Popov, Pis'ma Zh. Tekh. Fiz. **15**(5), 9 (1989) [Sov. Tech. Phys. Lett. **15**, (1989)].
[3] A. G. Glushchenko, Pis'ma Zh. Tekh. Fiz. **16**(21), 26 (1990) [Sov. Tech. Phys. Lett. **16**, (1990)].
[4] F. G. Bass, A. A. Bulgakov, and A. P. Tetervov, *RF Properties of Semiconductors with Superlattices* [in Russian], Nauka, Moscow (1989).
[5] A. P. Malozemoff, U. J. Gallagher, and R. E. Shvoll, *High-Temperature Superconductors* [Russ. transl., Mir, Moscow, 1988].

Translated by R. M. Durham

Study of the growth of $YBa_2Cu_3O_{7-x}$ films on a Al_2O_3 single crystal with a CeO_2 buffer sublayer

V. V. Afrosimov, E. K. Gol'man, R. N. Il'in, M. N. Panov. D. A. Plotkin, S. V. Razumov, V. I. Sakharov, I. T. Serenkov, and A. V. Tumarkin

A. F. Ioffe Physicotechnical Institute, Russian Academy of Sciences, St. Petersburg; St. Petersburg State Electrotechnical University
(Submitted August 28, 1997)
Pis'ma Zh. Tekh. Fiz. **24**, 91–95 (January 12, 1998)

Superconducting $YBa_2Cu_3O_{7-x}$ films were prepared by magnetron sputtering on Al_2O_3 single crystals with a CeO_2 sublayer. Scattering of moderate-energy ions and x-ray diffraction were used to show that the films exhibit good single-crystal properties over the entire thickness up to 2.6 μm. The hypothesis is advanced that the indentations formed by the growth of films above ''extraneous'' phase grains may act as defect sinks. © *1998 American Institute of Physics.* [S1063-7850(98)01701-7]

The initial stages of growth of superconducting films of complex composition such as $YBa_2Cu_3O_{7-x}$ prepared by an evaporation technique may be accompanied by the formation of islets of the main phase with differently oriented c axis and by ''extraneous'' phases whose composition and orientation differ from the main phase. During the subsequent growth of the film after the thickness has reached hundreds of nanometers, in the first case, a transition takes place from c-normal to a-normal growth[1] whereas in the second case, outgrowths or indentations form on the surface of the films.[2,3]

Here we investigate the quality of a $YBa_2Cu_3O_{7-x}$ film grown by magnetron sputtering on an Al_2O_3 substrate with a CeO_2 buffer layer[4] as a function of the film thickness under conditions where ''extraneous'' phases may form at the initial stage.[5] The structure of the films was investigated by scattering of moderate-energy ions[6,7] and by x-ray diffraction analysis while the surface was examined with a scanning electron microscope.

We investigated six films of different thicknesses, which were determined by the discharge current and the sputtering time. The characteristics of the films are given in Table I. The thicknesses of the first four films were determined from the ion backscattering spectra. Assuming close-packed structures ($\rho = 6.35$ g/cm^3), 10^{15} mol/cm^2 corresponds to 1.72 nm, i.e., the thinnest film was 82 nm thick. For the thickest film, the profilometer measurements gave 2600 nm. All the films were superconducting with $T_c = 88-90$ K. For the three thickest films the surface resistance, determined using the surface resonance at 4 GHz and 78 K, was less than 10^{-3} Ω. On the surface of all the films, scanning electron microscopy revealed indentations occupying between 3% and 18% of the surface area, their diameter increasing from 0.15 to 0.35 μm with increasing film thickness. X-ray diffraction analyses showed that in film No. 1 the fraction of grains with the c-axis normal to the substrate was at least 94% and for the other films, this fraction was even greater.

Scattering of $E = 240$ keV protons in channeling and unoriented beam modes was used to study the quality of the crystal structure of the films near the surface and over depth. The energy spectra of the scattered ions were measured using a spectrometric semiconductor detector with a resolution of around 3 keV, mounted at an angle of 155° to the incident beam. Spectra obtained in the channeling mode $Y_c(E)$ and with an unoriented beam $Y_r(E)$ are shown in Fig. 1 for sample No. 3.

The bulk quality of the film can either be assessed from the experimentally determined dependence of the fraction of the dechanneled beam on the energy of the scattered ions

$$\chi(E) = Y_c(E)/Y_r(E) \tag{1}$$

(also shown in Fig. 1), or using the model depth dependence of the dechanneling—$\chi^m(t)$. The parameters of the function $\chi^m(t)$ are selected to obtain the best agreement between the experimental curve $Y_c(E)$ and the calculated curve $Y_c^m(E)$, obtained by modeling the spectrum in the channeling mode. Data on the composition and thickness of the films were obtained by the generally accepted method of modeling the spectrum in the random orientation mode.[8] For all the films studied the function $\chi^m(t)$ is accurately described by the linear dependence

$$\chi^m(t) = \chi_0 + Dt. \tag{2}$$

This function may be compared with the analytic expression for the dependence of the dechanneled fraction of the beam on the depth distribution of defects when the concentration of these defects is low:[8]

TABLE I.

Film No.	Current, A	Time, h	Thickness, 10^{15} mol/cm^2	D, 10^{-18} cm^2/mol	χ_0	χ_{min}
1	0.2	5	48	1.8	0.14	0.20
2	0.4	2.5	60	2.6	0.10	0.16
3	0.2	10	95	2.6	0.07	0.13
4	0.2	20	155	1.8	0.06	0.12
5	0.2	45		1.6	0.06	0.11
6	0.4	40	2.6 μm*	1.7	0.07	0.11

*Measured with profilometer.

 1063-7850/98/010041-02$15.00

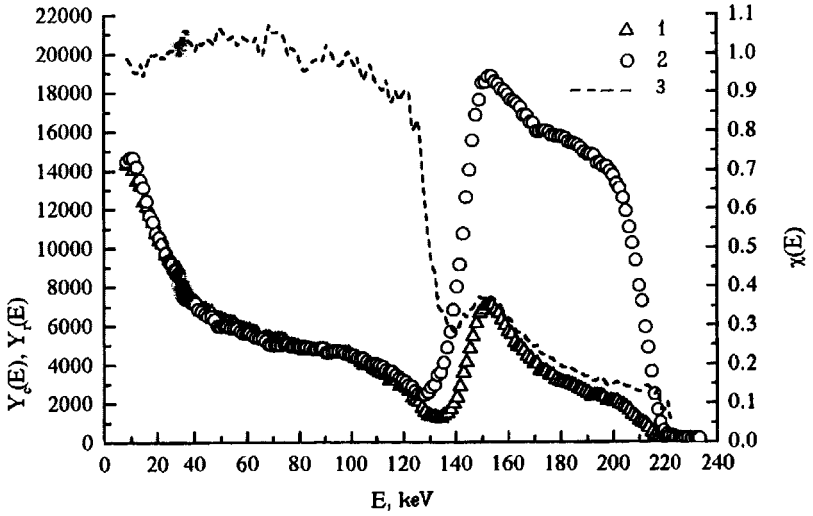

FIG. 1. Energy spectra of backscattered protons for film No. 3: *1*—channeling mode, *2*—unoriented mode, *3*—relative yield. (The number of particles is given on the *x* axis.)

$$\chi(t)=\chi_i(t)+\sum_k\left(f_k\frac{n_k(t)}{N}+\int_0^t\sigma_k(\varepsilon(z))n_k(z)dz\right), \tag{3}$$

where $\chi_i(t)$ characterizes the dechanneling in a defect-free crystal, n_k is the concentration, σ_k is the dechanneling factor, and f_k is the scattering factor for type k defects, ε is the precollisional energy, and N is the atomic concentration in the target. The scattering factor f_k is close to 1 for point defects and can be neglected for all others. For a fairly good-quality $YBa_2Cu_3O_{7-x}$ single crystal, $\chi_i(t)$ is expressed by the function (2) with $\chi_0=0.03$ and $D=0.9\times10^{-18}$ cm^2/mol (Ref. 7). The linear behavior of these functions (2) is quite consistent with the behavior of expression (3) assuming that the defect concentration is constant over depth. The parameters χ_0 and D obtained for these films are given in Table I.

The parameter D describes the rate of dechanneling with depth. The fact that this parameter does not increase with increasing film thickness, combined with the linear behavior of $\chi(t)$ and the fact that the film conserves its c-orientation with increasing thickness, as is deduced from the x-ray diffraction measurements, suggests that the grains forming the film have a uniform structure and extend from the interface with the sublayer to the surface.

The quality of the film near the surface is characterized by the minimum yield $\chi_{\min}$ determined from formula (1) directly after the surface peak (in our case at $t\approx30$ nm) or by the parameter χ_0 from formula (2) corresponding to $t=0$. The values of the parameter $\chi_{\min}$ are also given in Table I.

An analysis of the minimum yield data given in Table I shows that for thick films this is mainly determined by the value of $\chi_{\min}$ for the single crystal (0.07–0.08 (Ref. 7)) and by the misorientation of the blocks whose contribution, estimated according to Ref. 9 from our measured angular dependences of the scattered ion yield, may reach 0.04. For thin films having indentations whose width exceeds the thickness of the film, an appreciable contribution to $\chi_{\min}$ is made by the ''extraneous'' phase grains lying at the bottom of the indentations, which are not shaded by walls as in thick films.

To sum up, these studies have shown that during growth, at least to thicknesses of 2.5 μm, the films retain their homogeneous structure over most of the area and the direction of the c axis remains normal to the surface. Grains of extraneous phases are responsible for the formation of indentations on the surface but these do not cause any deterioration in the crystallinity of the rest of the film and their boundaries may even act as defect sinks.

This work was supported by BMDF/DVI Project No. 029850 (Germany).

[1] S. N. Basu, T. Roy, T. E. Mitchell, R. E. Muenchausen, and M. Nastasi, in *Science and Technology of Thin Film Superconductors 2* (Plenum Press, New York, 1990), pp. 341–349.
[2] M. G. Norton, C. B. Carter, B. H. Moeckly *et al.*, in *Science and Technology of Thin Film Superconductors 2* (Plenum Press, New York, 1990), pp. 379–387.
[3] R. Ramesh, A. Inam, D. M. Hwang, T. D. Sands, C. C. Chang, and D. L. Hart, Appl. Phys. Lett. **58**, 1558 (1991).
[4] E. K. Hollmann, A. G. Zaitsev, V. E. Loginov *et al.*, J. Phys. D **25**, 504 (1992).
[5] E. K. Gol'man, V. I. Gol'drin, D. A. Plotkin *et al.*, Fiz. Tverd. Tela (St. Petersburg) **39**(2), 216 (1997) [Phys. Solid State **39**, 189 (1997)].
[6] V. V. Afrosimov, G. O. Dzyuba, R. N. Il'in *et al.*, Sverkhprovodimost' **4**, 1767 (1991).
[7] V. V. Afrosimov, G. O. Dzyuba, R. N. Il'in *et al.*, Zh. Tekh. Fiz. **66**(12), 76 (1996) [Tech. Phys. **41**, 1240 (1996)].
[8] L. C. Feldman, J. W. Mayer, and S. R. Picraux, *Material Analysis by Ion Channeling* (Academic Press, New York, 1982).
[9] H. Ishiwara and S. Furukawa, J. Appl. Phys. **47**, 1686 (1976).

Translated by R. M. Durham

Stressed state of a matrix and an inclusion made from a twisted composite superconductor in cladding when a circular current interacts with a magnetic field

E. A. Devyatkin

Institute of Problems in Mechanics, Russian Academy of Sciences, Moscow
(Submitted May 22, 1997)
Pis'ma Zh. Tekh. Fiz. **24**, 1–6 (January 26, 1998)

This paper discusses the stressed state of the matrix and a long wire made from a twisted multicore composite superconductor and encased in cladding when the circular component of the transport current interacts with a magnetic field. © *1998 American Institute of Physics.* [S1063-7850(98)01801-1]

References 1–3 discussed the stressed state of the matrix and a long cylindrical inclusion made from a twisted multicore composite superconductor with a transport current, caused by the interaction of its longitudinal component with a magnetic field. It was shown in particular that the epoxy resin often used as the matrix in superconducting magnets and possessing low shear strength[4] $\tau_f=(1-6)\times10^6$ Pa when the critical current density is 10^9 A/m^2 in a wire with radius 10^{-3} m cracks in an external magnetic field of 2–12 T. The ratio of the circumference of a wire of twisted multicore composite superconductor to its pitch can be several tens;[5] consequently, the interaction of the circular component of the current with the magnetic field must in general be taken into account. Below we study the stressed state of the matrix and the wire in the cladding when such an interaction occurs.

Let us consider a wire consisting of a single twisted multicore composite superconductor ''soldered'' to an infinite nonferromagnetic matrix, surrounded by a cladding of radius δ_* and lying in an external homogeneous magnetic field with induction $\mathbf{B}_a$. Let the external field vary with time slowly enough that no macroscopic screening occurs. A transport current I, monotonically increasing with time and less than the critical value I_s ($I<I_s$), flows in the region $\delta<r<1$ (see Fig. 1), where $\delta^2=1-I/I_s$.[5] We shall assume that the superconducting properties of the wire are independent of the stresses and strains; that a macroscopic approach and the quasi-static approximation are valid when describing its physicomechanical state; that the inclusion, the cladding, and the matrix are linearly elastic, homogeneous, and isotropic; and that their Young's moduli and Poisson ratios equal, respectively, $E^{(k)}$ and $\nu^{(k)}$ ($k=i,e,m$). In the saturated zone, a Lorentz force $\mathbf{f}=\mathbf{j}_s\times\mathbf{B}$ acts on a wire in a magnetic field $\mathbf{B}$. Let us find the stresses in the media, caused by the interaction of the circular component j_θ of the transport current density vector $\mathbf{j}_s$ with the magnetic field (see Fig. 1). For small λ_p, defined as the ratio of the circumference of a wire made from a twisted multicore composite superconductor to its pitch, we have $j_\theta=\lambda_p j_s r$.[5] The magnetic field $\mathbf{B}$ is a superposition of the external field $\mathbf{B}_a$, which has a transverse component $\mathbf{B}_\perp$ and an axial component $\mathbf{B}_\parallel$ ($\mathbf{B}_a=\mathbf{B}_\perp+\mathbf{B}_\parallel$), and the field $\mathbf{B}_j$ of the circular currents of the wire ($\mathbf{B}=\mathbf{B}_a+\mathbf{B}_j$).

The equilibrium equation for the displacements $\mathbf{u}^{(j)}$ in the saturation zone has the form[6]

$$\Delta\mathbf{u}^{(j)}+\frac{1}{1-2\nu^{(i)}}\,\mathrm{grad}\ \mathrm{div}\ \mathbf{u}^{(j)}=-\frac{\mathbf{f}}{G^{(i)}},\tag{1}$$

where Δ is the Laplacian, and $G^{(i)}=E^{(i)}/[2(1+\nu^{(i)})]$ is the shear modulus of the wire. The volume force $\mathbf{f}$ in the case considered here has a radial component f_r and an axial component f_z. The displacements $\mathbf{u}^{(k)}$ outside the saturated zone satisfy similar homogeneous equations. We assume that, far from the inclusion, the matrix is not loaded [$\sigma^{(m)}(\infty)=0$]. The fact that the media are cemented means that there are no discontinuities of the displacements, the normal stresses σ_n, or the tangential stresses σ_τ at the boundaries of the regions:

$$[\mathbf{u}]=0,\quad [\sigma_n]=0,\quad [\sigma_\tau]=0\quad \text{for } r=\delta,1,\delta_*.\tag{2}$$

Let us first consider the interaction of a circular current with a transverse field $\mathbf{B}_\perp$ directed along the x axis. The volume force acts along the wire and is equal to $f_z=-j_\theta B_\perp\cos\theta$. We shall assume that the displacements are independent of the z coordinate.[1)] Then, from Eq. (1), we have for their longitudinal components $u_z^{(j)}$ Poisson's equation in a saturated field and Laplace's equation outside it. Continuous solutions of these equations, bounded at the axis of the inclusion and damping at infinity, with corresponding continuous stresses tangent to the boundaries under consideration, are

$$\begin{aligned}
&u_z^{(i)}=\frac{a}{G^{(i)}}r\cos\theta,\quad u_z^{(j)}=\frac{1}{G^{(i)}}(br+Wr^3+cr^{-1})\cos\theta,\\
&u_z^{(e)}=\frac{1}{G^{(e)}}(dr+er^{-1})\cos\theta,\quad u_z^{(m)}=\frac{g}{G^{(m)}}r^{-1}\cos\theta,\\
&\sigma_{rz}^{(i)}=a\cos\theta,\quad \sigma_{rz}^{(j)}=(b+2Wr^2-cr^{-2})\cos\theta,\\
&\sigma_{rz}^{(e)}=(d-er^{-2})\cos\theta,\quad \sigma_{rz}^{(m)}=-gr^{-2}\cos\theta,\\
&\sigma_{\theta z}^{(i)}=-a\sin\theta,\quad \sigma_{\theta z}^{(j)}=-(b+Wr^2+cr^{-2})\sin\theta,\\
&\sigma_{\theta z}^{(e)}=-(d+er^{-2})\sin\theta,\quad \sigma_{\theta z}^{(m)}=-gr^{-2}\sin\theta.
\end{aligned}\tag{3}$$

Here and below, the displacements are dimensionless, $W=\alpha_\perp W_j[2(1-\delta^2)]$, $W_j=(B_j^{(j)})^2/(2\mu_0)$, $B_j^{(i)}$ is the magnetic induction of the circular currents in the region $0\leqslant r\leqslant\delta$, $\alpha_\perp=B_\perp/B_j^{(i)}$, and μ_0 is the permeability of free space. The coefficients, normalized to $2W(1-\delta^4)$, equal

$$a=b+\frac{\delta^2}{1-\delta^4}=-\frac{1}{2}\frac{3+\delta^2}{1+\delta^2}-\beta_1(1+\beta_2),$$

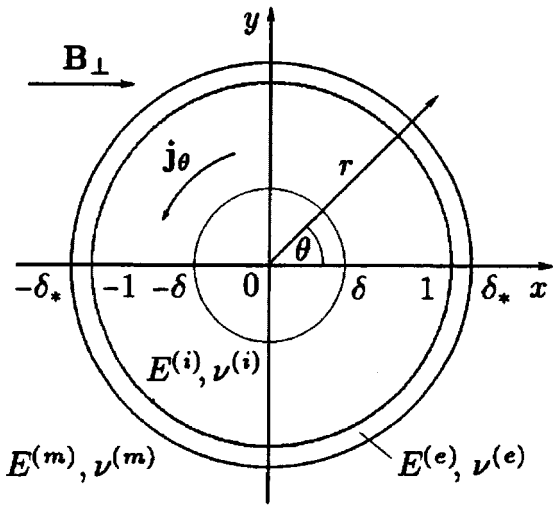

FIG. 1.

$$c=\frac{1}{2}\frac{\delta^4}{1-\delta^4},$$
$$d=-\beta_1, \quad e=\beta_1\beta_2, \quad g=\beta_1(\delta_*^2+\beta_2), \tag{4}$$

where

$$\beta_1=\left[\frac{G^i}{G^{(e)}}(1-\beta_2)-1-\beta_2\right]^{-1}, \quad \beta_2=\delta_*^2\frac{G^{(m)}+G^{(e)}}{G^{(m)}-G^{(e)}}.$$

Let us now consider the interaction of the circular currents with the longitudinal component of the magnetic field, equal to the sum of the field of these currents $B_j=B_j^{(j)}\times(1-r^2)/(1-\delta^2)$ and the homogeneous field $B_\parallel$. The volume force in this case has only a radial component $f_r=j_\theta(B_j+B_\parallel)$. From Eq. (1), we have ordinary differential equations for the radial displacements in each region. For a flat deformed state, their solutions, satisfying the conditions at the interfaces of the regions given by Eq. (2), the boundedness of the stresses on the axis of the inclusion, and the fact that they vanish as $r\to\infty$, are

$$u_r^{(i)}=Ar, \quad u_r^{(e)}=Dr+\frac{E}{r}, \quad u_r^{(m)}=\frac{F}{r},$$

$$u_r^{(j)}=Br-Pr^3\left(3\alpha_\parallel+\frac{3-r^2}{1-\delta^2}\right)+\frac{C}{r},$$

$$\sigma_r^{(i)}=\sigma_\theta^{(i)}=\frac{2G^{(i)}A}{1-2\nu^{(i)}},$$

$$\begin{pmatrix}\sigma_r^{(e)}\\ \sigma_\theta^{(e)}\end{pmatrix}=2G^{(e)}\left(\frac{D}{1-2\nu^{(e)}}\mp\frac{E}{r^2}\right),$$

$$\begin{pmatrix}\sigma_r^{(j)}\\ \sigma_\theta^{(j)}\end{pmatrix}=\frac{2G^{(i)}}{1-2\nu^{(i)}}\left\{B+Pr^2\left[\begin{pmatrix}5-4\nu^{(i)}\\ 1+4\nu^{(i)}\end{pmatrix}\frac{r^2}{1-\delta^2}-3\begin{pmatrix}3-2\nu^{(i)}\\ 1+2\nu^{(i)}\end{pmatrix}\left(\alpha_\parallel+\frac{1}{1-\delta^2}\right)\right]\mp(1-2\nu^{(i)})\frac{C}{r^2}\right\},$$

$$\sigma_r^{(m)}=-\sigma_\theta^{(m)}=-2G^{(m)}\frac{F}{r^2}, \quad \sigma_z^{(k)}=\nu^{(k)}(\sigma_r^{(k)}+\sigma_\theta^{(k)}). \tag{5}$$

Here

$$P=[(1-2\nu^{(i)})/(1-\nu^{(i)})]W_j/[12G^{(i)}(1-\delta^2)],$$
$$\alpha_\parallel=B_\parallel/B_j^{(i)},$$
$$A=B-3P\delta^2\left(2\alpha_\parallel+\frac{2-\delta^2}{1-\delta^2}\right)=P(1-\delta^2)^2(2+3\alpha_\parallel)+(1+\chi)D,$$
$$D=\frac{E}{\chi}=\frac{F}{\delta_*^2+\chi}=\frac{W_j}{6}[(1+\delta^2)(2+3\alpha_\parallel)-1]\times\left[\frac{G^{(i)}}{1-2\nu^{(i)}}(1+\chi)-G^{(e)}\left(\frac{1}{1-2\nu^{(e)}}-\chi\right)\right]^{-1},$$
$$C=-P\delta^4\left(3\alpha_\parallel+\frac{3-2\delta^2}{1-\delta^2}\right),$$
$$\chi=-\delta_*^2\left[1+2\frac{1-\nu^{(e)}}{1-2\nu^{(e)}}\left(\frac{G^m}{G^e}-1\right)^{-1}\right]. \tag{6}$$

A superposition of the solutions obtained in Refs. 2 and 3 and determined by Eqs. (3)–(6) makes it possible in general to calculate the stress–strain state of a matrix and a long wire ''soldered'' to it and made from a twisted multicore composite superconductor with a transport current in the presence of an arbitrarily oriented external magnetic field. Numerical estimates based on a solution of Eqs. (3) and (4) show that, in the practically interesting case of a strong transverse field and an epoxy matrix, the limiting stressed state of the matrix and of a thin cladding similar to it in elastic properties[4] can be analyzed with an accuracy no worse than 1–2%, starting from the solution obtained in Ref. 2.

The results of this paper can be used to analyze the stressed state of design elements containing superconductors that weakly elastically interact with each other.

[1)]Such a state occurs, for example, in a thin ring made from a twisted multicore composite superconductor situated in a magnetic field perpendicular to its plane. For $x>0$ and $x<0$ (see Fig. 1) the longitudinal Lorentz forces are equal in magnitude and oppositely directed.

[1] E. A. Devyatkin, Pis'ma Zh. Tekh. Fiz. **22**, No. 10, 74 (1996) [Tech. Phys. Lett. **22**, 420 (1996)].
[2] E. A. Devyatkin, Cryogenics **37**, 129 (1997).
[3] E. A. Devyatkin, *Abstracts of Reports of the Fourth International Conference–Seminar on Engineering Physics Problems of New Technology*, Moscow, 1996, pp. 66–67.
[4] E. S. Bobrov, J. E. S. Williams, and V. Iwasa, Cryogenics **25**, 307 (1985).
[5] A. Vl. Gurevich, R. G. Mints, and A. L. Rakhmanov, *The Physics of Composite Superconductors* (Nauka, Moscow, 1987).
[6] V. Novatskiĭ, *The Theory of Elasticity* (Mir, Moscow, 1975).

Translated by W. J. Manthey
Edited by David L. Book

Superconducting-coil–resistor circuit with electric field quadratic in the current

N. A. Poklonskiĭ and S. Yu. Lopatin

State University of Belarus, Minsk
(Submitted April 16, 1997)
Pis'ma Zh. Tekh. Fiz. **24**, 7–11 (January 26, 1998)

It is shown for the first time that the observed [Phys. Lett. A **162**, 105 (1992)] potential difference Φ_t between the resistor and the screen surrounding the circuit is caused by polarization of the resistor because of the kinetic energy of the electrons of the superconducting coil. The proportionality of Φ_t to the square of the current and to the length of the superconducting wire is explained. It is pointed out that measuring Φ_t makes it possible to determine the Fermi quasimomentum of the electrons of a metal resistor. © *1998 American Institute of Physics.* [S1063-7850(98)01901-6]

Edwards *et al.*[1,2] observed the appearance of an electric potential that was quadratic in the current I on a resistor that formed a closed circuit with a superconducting coil relative to a grounded screen (see Fig. 1). They showed experimentally that the potential difference between the center of the resistor R and the screen satisfies $\Phi_t \propto bI^2$, where b is the length of the superconducting wire. The value of Φ_t is virtually independent of the configuration inductance of the coil, $L_c \approx 800$ μH, which is minimized by bifilar winding. When the current is $I=16$ A and $b \approx 700$ m, for $R=82$ $\mu\Omega$, a typical value is $\Phi_t \approx 5$ mV. The time constant of the circuit is $\tau = L_c/R \approx 10$ sec. A superconducting wire (NbTi, pure Nb, and also Pb) with a diameter of $2a \approx 127$ μm was covered with a copper layer (thickness 19 μm) whose resistance was much greater than R. The coil and the resistor were immersed in liquid helium; the signal wire of the electrometer V was connected to the center of the resistor. The resistor and the electrostatic screen were made from brass.

In principle, a steady-state electric field quadratic in current appears along a rectilinear superconductor of finite length.[3] However, for a closed circuit, it is necessary to take into account the retardation of fields[4] from charges moving with acceleration because of the rotation of their current velocity vector (this was neglected in Ref. 5). When a consistent treatment is used, it is found that there is no electric field around a superconducting circuit with a steady-state current.[6] At the same time, it is shown in Ref. 7 that, if the ratio of the distance between the ''superconducting'' electrons to the distance between the atomic residues (the ions) is assumed to be equal to $\sqrt{1-\beta^2}$, where β is the ratio of the current velocity of the electrons to the velocity of light, the total electric field is proportional to β^2 even when it is averaged over a sphere surrounding a circuit with a current. However, this assumption has not been proven.[8–10]

The appearance of an electric field proportional to I^2 can also be caused by the accelerated motion of charges in the curvilinear section of a conductor,[11] by the redistribution under the action of the intrinsic magnetic field of the electric charge density (the radial Hall effect)[12,13] or of the current in an electrically neutral metal medium (the pinch effect),[14] as well as by the difference of the cross-sectional area of different sections of a conductor (the Bernoulli effect).[13,15] However, quantitative estimates do not allow Edwards *et al.*'s results to be regarded as a manifestation of these effects (see also Refs. 1 and 2). This served as the basis for the discussion of Refs. 7–10 on the relativistic invariance of the equations that describe the total charge of a closed system with a current. (In the recent ''optical'' experiment of Ref. 16, the Lorentz transformations were confirmed with an accuracy of 7×10^{-5}.)

The goal of this paper is to interpret the experiments of Edwards *et al.*.[1,2]

We start from the fact that the total energy of a superconducting coil with current I is the sum of the magnetic-field energy $L_cI^2/2$ and the kinetic energy K of the directed motion of the electrons. For a coil wound with wire $2a$ in diameter and b in length, the kinetic energy of the electrons is[17]

$$K = \frac{L_kI^2}{2} = \frac{\mu_0 \lambda b}{8\pi a} I^2, \tag{1}$$

where L_k is the kinetic inductance, $\lambda \ll a$ is the London current-excitation depth in the wire, and μ_0 is the permeability of free space.

Under the conditions of Edwards *et al.*'s experiment, the total inductance of the coil is $L_t = L_c + L_k \approx L_c$.

After the resistor is added to the superconducting circuit, the current damps out and an induction electric field appears, aligned with the current. The induction potential difference at the ends of the resistor is $U_i \approx -L_c dI/dt = IR$; the potential of the center of the resistor is $\Phi_i = U_i/2$ (here and below, relative to an infinitely remote point, where the potential is set equal to zero). A potential Φ_n, proportional to the current in the coil, appears at the point where the electrometer is grounded, as a consequence of the mutual inductance of the circuit and the screen. It is clear that Φ_n has different magnitudes (and signs) at different sections of the screen because of the vortex character of the currents I_n.

At the initial instant when the resistor is connected into the superconducting circuit, all of its N conduction electrons are displaced by the mean free path l relative to the atomic residues, in the direction opposite the current. As a result, the resistor is polarized, thereby consuming part of the energy stored in the superconducting coil.[18,19] The potential energy of the polarization is $W = EP/2$, where E is the electric field, $P = qlN$ is the dipole moment, and $q > 0$ is the electronic

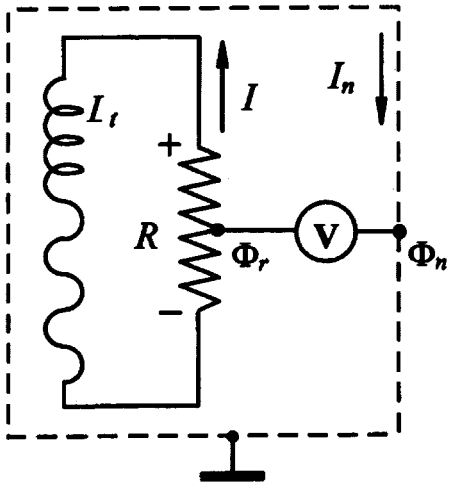

FIG. 1. Schematic representation of the measurements of Edwards *et al.*.[1,2]

charge. The polarization potential difference on the ends of a resistor of length d is $U_p = Ed$; the potential of the center of the resistor is $\Phi_p = U_p/2$.

Since the energy W consumed by the polarization of the resistor is limited to K, from the relationship $U_p P/2d = L_k I^2/2$ and using Eq. (1), we get the estimate

$$\Phi_p = \frac{L_k I^2 d}{2qlN} = \frac{\mu_0 \lambda b}{8\pi qalSn} I^2, \tag{2}$$

where $n = N/Sd$ is the density of conduction electrons in a resistor with cross-sectional area S and length d.

It follows from Eq. (2) that the polarization potential Φ_p is proportional to the square of the current and the length of the superconducting section of the circuit but is independent of the length of the resistor.

At liquid-helium temperature, the contribution of the additional resistance of the resistor–superconductor junction (the critical temperature is ≈ 10 K) to creating a potential difference at the ends of the resistor is negligible.[17]

Provided that $q(U_p - IR) = 2q(\Phi_p - \Phi_i)$ remains less than the energy gap of the superconductor (≈ 3 meV), the current in the circuit ceases.

The potential difference between the resistor and the screen measured in Edwards *et al.*'s experiments is thus $\Phi_t = \Phi_r - \Phi_n$, where $\Phi_r = \Phi_p - \Phi_i$ is the potential of the center of the resistor (the point where the signal wire is connected), and Φ_n is the potential of the grounding point of the electrometer.

From the parameters of a brass resistor, $R = 82\ \mu\Omega$, $d = 14$ mm, and $S \approx 0.1$ cm^2, we find its conductivity $\sigma \approx 1.6 \times 10^5 \Omega^{-1}$ cm^{-1}. According to the data of Ref. 20, the density of conduction electrons in brass ($Cu_{1-x}Zn_x$) with an atomic density of 8.65 g·cm^{-3} for $x \approx 0.2$ is $n \approx 9.8 \times 10^{22}$ cm^{-3}. At liquid-helium temperature, the mean free path $l = p_F \sigma/q^2 n$ of the conduction electrons is determined by the quasi-momentum $p_F = \hbar(3\pi^2 n)^{1/3}$ at the Fermi surface. Substituting the values $\lambda \approx 38$ nm (for Nb and Pb) and $l \approx 10$ nm (for brass) into Eq. (2), with $I = 16$ A gives $\Phi_p \approx 4$ mV and $\Phi_i \approx 0.65$ mV. The potential difference $\Phi_t \approx \Phi_r = \Phi_p - \Phi_i \approx 3.3$ mV (for $\Phi_n = 0$) is comparable with the experimental value.

The sign of $\Phi_t = \Phi_r - \Phi_n$ must be independent of the direction of the current in the circuit for a given electrical configuration.

Note that, when $l \propto p_F/n$, $\Phi_p \propto \lambda/p_F$ follows from Eq. (2); i.e., the Fermi quasi-momentum p_F of the electrons in the resistor can be determined by measuring $\Phi_t \approx \Phi_p$.

Thus, the superconducting-coil–resistor circuit in Edwards *et al.*'s experiments[1,2] has an electric field that is quadratic in current because the polarization electric field of the resistor predominates over the induction field. In a well-known sense, Edwards *et al.*'s experiments supplement the experiments of Tolman *et al.* (see Ref. 21), who measured a damped current in a closed circuit, caused by the motion of the conduction electrons due to inertia after the removal of a rotating nonsuperconducting coil.

We are grateful to I. Z. Rutkovskiĭ, G. S. Kembrovskiĭ, and V. V. Mityanok for discussions.

This work was carried out within the Low-Dimension Systems Program of the Ministry of Education of the Republic of Belarus.

[1] W. F. Edwards, C. S. Kenyon, and D. K. Lemon, Phys. Rev. D **14**, 922 (1976).
[2] D. K. Lemon, W. F. Edwards, and C. S. Kenyon, Phys. Lett. A **162**, 105 (1992).
[3] V. V. Mityanok and N. A. Poklonskiĭ, Zh. Tekh. Fiz. **63**, No. 1, 189 (1993) [Tech. Phys. **38**, 49 (1993)].
[4] L. D. Landau and E. M. Lifshitz, *The Classical Theory of Fields* (Nauka, Moscow, 1988; Pergamon Press, New York, 1975).
[5] V. N. Strel'tsov, Soobshch. OIYaI Dubna, No. D2–92–196, 1 (1992).
[6] J. D. Jackson, *Classical Electrodynamics* (Wiley, New York, 1975).
[7] T. Ivezic, Phys. Lett. A **162**, 96 (1992).
[8] D. F. Bartlett and W. F. Edwards, Phys. Lett. A **162**, 103 (1992).
[9] N. Bilic, Phys. Lett. A **162**, 87 (1992).
[10] A. K. Singal, Phys. Lett. A **162**, 91 (1992).
[11] A. R. Apsit, Fiz. Tekh. Poluprovodn. **26**, 1850 (1992) [Sov. Phys. Semicond. **26**, 1039 (1992)].
[12] M. L. Martinson and A. V. Nedospasov, Usp. Fiz. Nauk **163**, No. 1, 91 (1993) [Phys. Usp. **36**, 23 (1993)].
[13] R. Jaggi, Phys. Rev. **122**, 448 (1961).
[14] É. A. Kaner, Yu. G. Leonov, and N. M. Makarov, Zh. Éksp. Teor. Fiz. **93**, 2020 (1987) [Sov. Phys. JETP **66**, 1153 (1987)].
[15] M. Chester, Phys. Rev. A **133A**, 907 (1964).
[16] D. Hils and J. L. Hall, Phys. Rev. Lett. **64**, 1697 (1990).
[17] V. V. Shmidt, *Introduction to Superconductor Physics* (Nauka, Moscow, 1982).
[18] V. G. Polevoĭ, Izv. Vyssh. Uchebn. Zaved. Radiofiz. **33**, 818 (1990).
[19] M. A. Miller, Izv. Vyssh. Uchebn. Zaved. Radiofiz. **29**, 991 (1986).
[20] I. S. Grigor'ev and E. Z. Meĭlikhov, Eds., *Physical Quantities. A Handbook* (Energoatomizdat, Moscow, 1991).
[21] I. M. Tsidil'kovskiĭ, Usp. Fiz. Nauk **115**, 321 (1975) [Sov. Phys. Usp. **18**, 161 (1975)].

Translated by W. J. Manthey
Edited by David L. Book

The possibility of improving the structural perfection of the new heterojunctions GaAs–$(Ge_2)_{1-x}(ZnSe)_x$, Ge–$(Ge_2)_{1-x}(ZnSe)_x$, GaP–$(Ge_2)_{1-x}(ZnSe)_x$, and Si–$(Ge_2)_{1-x}(ZnSe)_x$

A. S. Saidov, É. A. Koshchanov, and A. Sh. Razzakov

Physics–Sun Physicotechnical Institute Scientific Manufacturing Organization, Academy of Sciences of the Republic of Uzbekistan, Tashkent
(Submitted April 30, 1997)
Pis'ma Zh. Tekh. Fiz. **24**, 12–16 (January 26, 1998)

Based on morphological investigations, as well as on a study of the scanning patterns and diffraction spectra of the heterostructures GaAs–$(Ge_2)_{1-x}(ZnSe)_x$, Ge–$(Ge_2)_{1-x}(ZnSe)_x$, GaP–$(Ge_2)_{1-x}(ZnSe)_x$, and Si–$(Ge_2)_{1-x}(ZnSe)_x$, it is shown that the crystal perfection of these structures depends on the choice of the conditions of liquid-phase epitaxy. It is shown that mirror-smooth epitaxial layers of $(Ge_2)_{1-x}(ZnSe)_x$ with the lowest stress levels can be obtained on GaAs (100) and Ge (111) substrates.
[S1063-7850(98)02001-1]

Since the practicability of using any particular kind of heterostructure is mainly determined by its crystal perfection, the study of defect formation in the resulting heterojunctions, both in the region of the heteroboundary and in the bulk of the epitaxial layer, is one of the most important stages in semiconductor device technology.

This paper presents the results of studies of the structural perfection of the heterojunctions GaAs–$(Ge_2)_{1-x}(ZnSe)_x$, Ge–$(Ge_2)_{1-x}(ZnSe)_x$, GaP–$(Ge_2)_{1-x}(ZnSe)_x$, and Si–$(Ge_2)_{1-x}(ZnSe)_x$ as a function of the conditions under which they are fabricated. We were the first to obtain these heterojunctions by growing epitaxial layers of solid solutions of $(Ge_2)_{1-x}(GaAs)_x$, from a tin solution–melt bounded by two horizontal substrates by the method of forced cooling.[1] Single-crystal plates of GaAs, Ge, GaP, and Si oriented along the (111) and (100) directions served as substrates.

Preliminary experiments showed that the basic conditions that are imposed on a solution–melt when growing solid solutions of the $(IV_2)_{1-x}(III–V)_x$ class[2,3] also need to be created when growing solid solutions of the $(IV_2)_{1-x}(II–VI)_x$ class. Therefore, the process of growing layers of the solid solutions in question was preceded by a careful selection of the appropriate solvent, the solution–melt composition, and the temperature interval of growth, as well as by preliminary experiments on the solubility of ZnSe in a multicomponent liquid phase. Morphological studies of the cleavage face of the structures and of the surface of the epitaxial layers, carried out with an MIM-8M metallographic microscope, showed that mirror-smooth epitaxial layers of $(Ge_2)_{1-x}(ZnSe)_x$ grow on GaAs substrates oriented in the (100) direction and on Ge substrates oriented in the (111) direction. As expected (since the lattice mismatch is 4%), continuous epitaxial layers of $(Ge_2)_{1-x}(ZnSe)_x$ of satisfactory quality cannot be obtained on GaP substrates. At the temperature at which epitaxy begins, $T_{crys}=660$ °C, only growth islands are obtained on GaP. Although the growth islands melted into each other as the temperature at which epitaxy begins is increased, forming a continuous layer, such layers had a matt surface and numerous cracks. We observed the same situation when we attempted to grow layers of $(Ge_2)_{1-x}(ZnSe)_x$ solid solutions on silicon substrates.

The quality of the epitaxial layers of $(Ge_2)_{1-x}(ZnSe)_x$ grown on GaAs and Ge substrates also depended on the forced cooling rate, which was varied in the interval 1–5°/min. The optimum cooling rate for obtaining mirror-smooth layers of the solid solution $(Ge_2)_{1-x}(ZnSe)_x$ was 1–1.5°/min, which corresponded to an actual crystallization rate of the layers of 0.17–0.2 μm/min. The structural perfection of the layers thus grown, other conditions being equal, also depended on the gap δ between the horizontal substrates, whose value can be varied in the interval 0.25–2.5 mm by means of special graphite supports. For gaps of $\delta<0.35$ mm, no growth of epitaxial layers was observed in general, probably because the substrates are not wetted by the solution–melt. The layers of solid solutions that were most perfect in structure both on the upper and lower substrates are grown with gaps δ lying in the interval 0.35–0.8 mm. For $\delta>0.8$ mm, the quality of layers grown on the lower and upper substrates differed greatly. The quality of the epitaxial layers grown on the lower substrates was always higher than in the layers grown on the upper substrates. This was also reflected in the surface dislocation density of the as-grown layers. This difference increased with increasing δ. In our opinion, this is associated with the fact that convection flows become predominant over molecular diffusion in the mechanism by which mass is supplied to the crystallization front as the gap increases, as we established earlier.[4]

The x-ray fluorescence spectrum of the layer surface contained peaks corresponding to germanium ($\lambda=1244$ mÅ), zinc ($\lambda=1306$ mÅ), and selenium ($\lambda=1105$ mÅ), while a determination of the layer composition through the thickness by means of an x-ray microanalyzer showed that the ZnSe concentration in the layer increases along the growth direction. The rapidity with which x varied over the thickness depended on process factors (the growth-temperature interval, the gap between the substrates, the solution–melt composition, the crystallization rate, etc.). Moreover, it was found that the ZnSe concentration in the

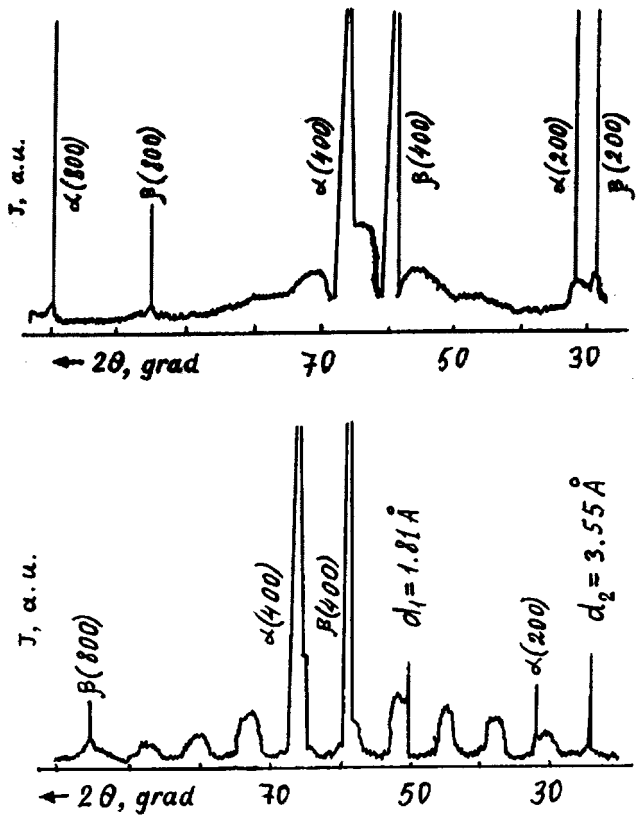

FIG. 1. Diffraction patterns of GaAs–$(Ge_2)_{1-x}(ZnSe)_x$ heterostructures grown on the upper (a) and the lower (b) substrate.

interface region increases with the temperature T_{crys} at which crystallization begins from 46 mol% at $T_{crys}=580$ °C to 72 mol% at $T_{crys}=680$ °C.

Raster scans of a cleavage face of the structure and of the surface of the layers, measured at the characteristic x-ray lines K_α(Ge), K_α(Zn), K_α(Se), K_α(Ga), and K_α(As), showed that macroscopic defects and metal inclusions are absent both at the interface and in the bulk of the layer and that the distribution of the Zn, Se, and Ge components of the solid solution is homogeneous over the surface of the epitaxial layer.

The structural perfection of the layers thus grown was also studied by x-ray diffraction on a DRON-UM1 apparatus. The diffraction spectra were obtained by continuous recording at the lines of the copper anode ($\lambda_\alpha=1.5418$ Å and $\lambda_\beta=1.3922$ Å). The anode voltage and current were 30 kV and 10 mA, respectively. The exposure time was varied in the interval 1–3 h. It was found that the shape and location of the diffraction peaks in the spectrum depend on the growth conditions of the solid solutions (see Figs. 1a and 1b). The crystal lattice constants, estimated from the angles of the diffraction maxima, lie in the interval $(5.655-5.662)\pm0.005$ Å. If we assume that Vegard's law is valid, we get $a=5.662$ Å for solid solutions of $(Ge_2)_{1-x}(ZnSe)_x$ with a composition of $x=0.5$.

Since the lattice constants of the GaAs substrate (5.654 Å) and the solid solution $(Ge_2)_{1-x}(ZnSe)_x$ almost coincide within the limits of measurement error, it can be assumed that the individual maxima of the corresponding crystal lattices of the substrate and the epitaxial layer coincide in the diffraction spectrum. It should also be pointed out that the epitaxial layers of solid solutions of $(Ge_2)_{1-x}(ZnSe)_x$ grown on the lower substrates are distinguished by good monocrystallinity and the smallest stress levels; this is evidenced by the absence in the diffraction pattern of peaks corresponding to phases that differ from the initial values. At the same time, additional peaks corresponding to interplane distances $d_1=1.81$ Å and $d_2=3.55$ Å, as well as shallow maxima located symmetrically relative to the $\alpha(400)$ and $\beta(400)$ maxima of the initial phases, are detected in the diffraction spectrum (see Fig. 1b) of layers grown on the upper substrates (i.e., with accelerated growth). The additional peaks can apparently be associated with the possible formation of phases of the wurtzite modification of the solid solutions. As many as fourteen similar symmetrical shallow peaks were also observed by Abdikamalov *et al.*[5] in multilayer GaAs–ZnSe structures. However, they detected no connection of the shallow maxima with either the crystal structure or the chemical composition of the multilayer structures.

In conclusion, we should point out that, by choosing the conditions of liquid-phase epitaxy, it is possible to obtain structurally perfect graded-gap epitaxial layers of $(Ge_2)_{1-x}(ZnSe)_x$ solid solutions on GaAs and Ge substrates.

[1] A. S. Saidov, D. V. Saparov, É. A. Koshchanov, A. Sh. Razzakov, and V. A. Rysaeva, in *Abstracts of Reports of the Scientific–Technical Conference on New Inorganic Materials*, Tashkent, September 18–20, 1996, p. 98.

[2] A. S. Saidov, É. A. Koshchanov, B. Sapaev, and G. N. Kovardakova, Dokl. Akad. Nauk Uz. SSR. No. 2, 26 (1988).

[3] Zh. I. Alferov, M. Z. Zhingarev, K. G. Konnikov *et al.*, Fiz. Tekh. Poluprovodn. **16**, 831 (1982) [Sov. Phys. Semicond. **16**, 532 (1982)].

[4] A. S. Saidov, É. A. Koshchanov, A. Sh. Razzakov, D. V. Saparov, and V. A. Rysaeva, Uzb. Fiz. Zh. No. 1, 16 (1997).

[5] B. A. Abdikamalov, B. Atashov, M. D. Duĭsenbaev, and U. K. Ernazarov, in *Abstracts of Reports of the Second International Conference on Multilayer Graded-Gap Periodic Semiconductor Structures and Devices Based on Them*, Nukus, 28–30 September 1993, pp. 17–18.

Translated by W. J. Manthey
Edited by David L. Book

Optical amplification in a planar multichannel Mach–Zehnder interferometer based on metal–semiconductor–metal structures

N. M. Ushakov and K. Yu. Kravtsov

Institute of Radio Engineering and Electronics, Russian Academy of Sciences (Saratov Branch)
(Submitted June 25, 1997)
Pis'ma Zh. Tekh. Fiz. **24**, 17–21 (January 26, 1998)

This paper describes a new optoelectronic device—an optical transistor that provides power amplification of output visible radiation. The optical transistor is structurally based on a metallized semiconductor plate with a microchannel gap in the form of a planar Mach–Zehnder interferometer. A device of the light–light type is controlled by modulating the refractive index in one arm of the interferometer. © *1998 American Institute of Physics.*
[S1063-7850(98)02101-6]

A refractive-index change in the optical region sufficient for practical applications has been obtained comparatively recently by means of photoinduced free carriers (see, for example, Ref. 1). Modulation and switching of the light–light type have also been obtained through photoinduced perturbation of the refractive index in photoconductive planar and channel waveguides based on silicon[2] and gallium arsenide[3] and in concentrated structures on a $p-n$ junction.[4]

This paper proposes a new optoelectronic light-controlled device for modulating and amplifying light signals with metal–semiconductor–metal structures, which could be widely used in optical information-processing systems and fiber-optic communication lines.[5]

The optical transistor is a planar Mach–Zehnder interferometer based on a metallized semiconductor plate with a gap in the form of a microchannel structure in parallel waveguides. The structure of the waveguides has a Y-shaped branching at the input and output, an optical-wave phase compensator, and a control element consisting of the open gaps of the microchannel waveguides. Such structures could have extensive applications, because the fabrication process is simple and comparatively cheap.

An overall view of the optical transistor is shown in Fig. 1. Reference radiation is introduced into the interferometer through the input (end) of the semiconductor substrate in a microchannel waveguide. The carrier concentration in the waveguide is varied by means of continuous compensating visible radiation incident on one arm of the interferometer, and the refractive index is thereby changed in this arm of the waveguide. When this is done, the necessary phase shift is created to provide the minimum value of the output optical power (the transistor shuts off). The optical control (modulating) beam is introduced through the other arm of the interferometer. This causes a phase shift different from π between the parallel arms of the interferometer, and the radiation intensity at the output of the optical transistor increases. The entire structure of the metal electrodes is connected to an external source of electric field, which provides a field of $E \simeq 10^4$ V/cm in the gap. In this case, the gap is comparable with the width of the depletion region of the semiconductor.

The dependence of refractive index n on the carrier concentration N has the form[6]

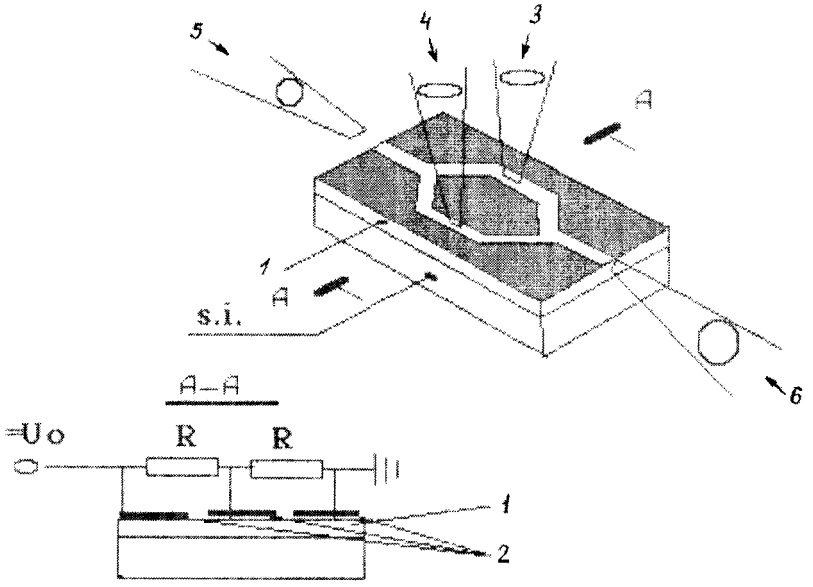

FIG. 1. Overall view of optical transistor: *1*—active layer, *2*—metal electrodes, *3*—control signal (input), *4*—compensation signal, *5*—reference signal, *6*—output signal.

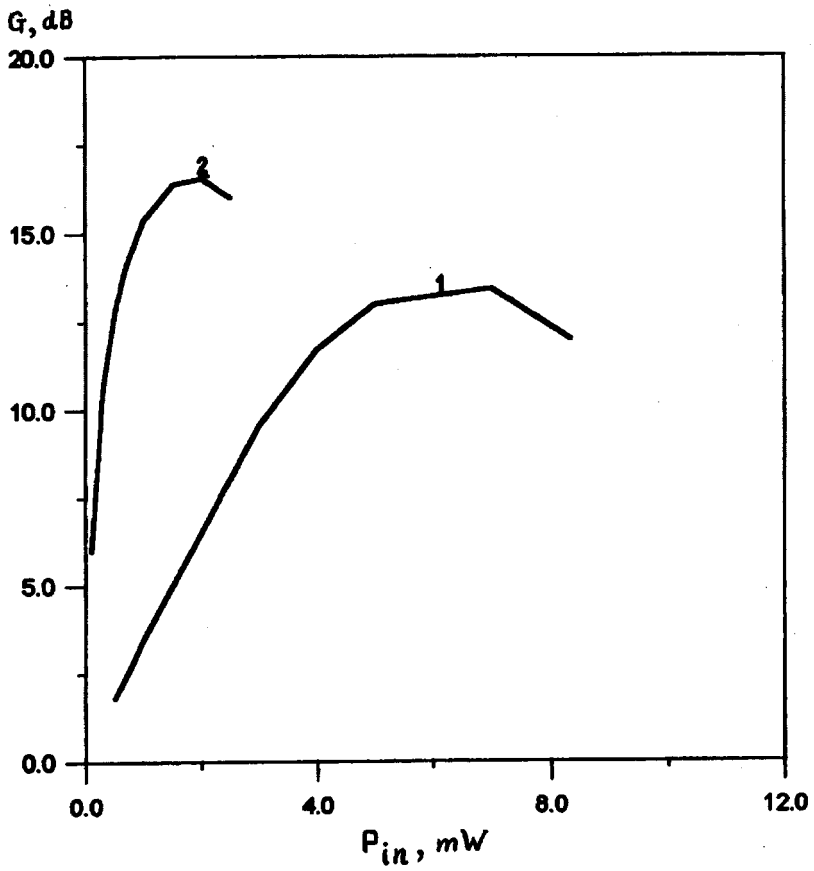

FIG. 2. Optical gain vs input optical power for $l=0.3$ mm (*1*) and $l=1$ mm (*2*).

$$n=n_0-(Nq^2/2\varepsilon_0 m^*\omega^2),$$

where n_0 is the refractive index in the absence of a nonequilibrium concentration of free carriers, q is the charge of an electron, ε_0 is the permittivity of free space, m^* is the effective mass, m_0 is the mass of a free electron in vacuum, ω is the circular frequency of light, and N is the nonequilibrium carrier concentration in the semiconductor.

To maintain a lower-order mode, it is necessary that $\Delta n \simeq 10^{-4}$. Using, for example, the parameters for n-GaAs ($m^*=0.067m_0$, $\omega^2=3.6\times10^{30}$ Hz^2, and $n_0=3.16$), we get $\Delta n=2.5\times10^{-27}N$ (in SI units). For a value of $\Delta n=10^{-4}$, we get $N=10^{23}$ m^{-3} (or 10^{17} cm^{-3}).

In a Mach–Zehnder interferometer, the optical signal is modulated through either arm of the interferometer.

Since the light is modulated by means of P_{in}, the gain G of an optical transistor will be defined as

$$G=P_{\text{out}}/P_{\text{in}}=I_{\text{out}}/I_{\text{in}}=G_0\sin^2(\Delta\Phi/2),$$

where $G_0=P_0(\eta\tau/h\nu V\Delta N)$ is the maximum gain of the optical transistor; P_0 is the power of the reference signal in W; η is the quantum efficiency of the photoelectric converter; τ is the nonequilibrium carrier lifetime in the semiconductor in sec; h is Planck's constant in J·sec; ν is the frequency of light in sec^{-1}; V is the absorbing volume in m^3; ΔN is the change of the carrier concentration in m^{-3}; $\Delta\Phi=2\pi L\Delta n/\lambda$ is the change of the phase shift of the light wave in the controlling arm of the interferometer; L is the length of the arm in m; Δn is the change of the refractive index; and λ is the wavelength of the light in m.

Figure 2 shows the results of calculating the gain of an optical transistor on semi-insulating n-GaAs, provided that the power of the reference signal is $P_0=0.1$ W, the length of the arm is $L=0.3$ mm (*1*) and 1 mm (*2*), and the wavelength of the light is $\lambda=1$ μm. When a control signal with power in the range 1–10 mW is used, the gain for case (1) equals 13–14 dB and has a dynamic range of 2–12 mW in the control signal. Here ''dynamic range'' refers to the limits of the input optical control power for which the gain varies by no more than 3 dB. Increasing the length of the arm to 1 mm, other conditions being equal, reduces the power of the control signal by a factor of 4–10, broadens the dynamic range by a factor of 2.5, and increases the gain by 5–6 dB.

[1] B. R. Bennett, R. A. Soref, and J. D. Alomo, IEEE J. Quantum Electron. **19**, 1525 (1990).
[2] P. D. Colbourne and P. E. Jessop, Electron. Lett. **24**, 303 (1988).
[3] Z. Y. Cheng and C. S. Tsai, Appl. Phys. Lett. **59**, 2222 (1991).
[4] P. G. Kasherinov, A. V. Kichaev, Yu. N. Perepelitsyn *et al.*, Preprints Nos. 1569 and 1570, Ioffe Physicotechnical Institute, St. Petersburg, 1991, parts 1 and 2.
[5] N. M. Ushakov and K. Yu. Kravtsov, ''An optical transistor,'' Russian Federation Patent No. 202899, Byul. 23. Cl. G 02 F 3/00 (1994).
[6] G. S. Svechnikov, *Elements of Integrated Optics* (Radio i Svyaz', Moscow, 1987).

Translated by W. J. Manthey
Edited by David L. Book

A universal expression for the propagation rate of the normal phase over a high-temperature superconducting film with a transport current

N. A. Buznikov and A. A. Pukhov

Joint Institute of High Temperatures, Moscow Center for Research in Applied Electrodynamics Problems, Russian Academy of Sciences, Moscow
(Submitted May 13 1997)
Pis'ma Zh. Tekh. Fiz. **24**, 22–26 (January 26, 1998)

The transport-current-initiated propagation of the normal phase over a high-temperature superconducting film located on a thermally stabilized substrate has been studied theoretically. A universal expression for the propagation rate of the normal phase is obtained that takes into account the influence of the substrate on the evolution of thermal instability in the film and can be applied for an arbitrary dependence of the critical current on temperature. The resulting expression is shown to describe the experimental data satisfactorily. © *1998 American Institute of Physics.* [S1063-7850(98)02201-0]

The breakdown of superconductivity by the transport current in a high-temperature superconducting (HTSC) film is associated with the onset of thermal instability in it. The asymptotic behavior of the nonlinear stage of the instability is characterized by the propagation over the film of a normal-phase front, moving with constant velocity. A number of papers[1–4] have reported the propagation rate v of the normal phase, experimentally measured for HTSC films with various temperature dependences of the critical current $I_c(T)$, with various cooling conditions, and also with various regimes for introducing current into the film. In this paper, a universal expression is obtained for the rate at which a normal-phase front propagates over an HTSC film placed on a thermally stabilized substrate, yielding a satisfactory description of the results of experiments.

The propagation rate of the normal phase over the film substantially depends on the distribution of the temperature field through the thickness of the substrate, whose reverse side is thermally stabilized at a temperature of T_0.[5] To compute the propagation rate v of the normal phase, the film and the substrate must be treated separately, as two interacting thermal subsystems. The temperature T in a film of thickness D_f and a substrate of thickness is D_s described by

$$C_f\frac{\partial T}{\partial t}=\frac{\partial}{\partial x}\left(k_f\frac{\partial T}{\partial x}\right)+Q(T)+\frac{k_s}{D_f}\left(\frac{\partial T}{\partial y}\right)\Bigg|_{y=D_f},$$

$$0<y<D_f, \tag{1}$$

$$C_s=\frac{\partial T}{\partial t}=\frac{\partial}{\partial x}\left(k_s\frac{\partial T}{\partial x}\right)+\frac{\partial}{\partial y}\left(k_s\frac{\partial T}{\partial y}\right),\quad D_f<y<D_f+D_s. \tag{2}$$

Here C_f and C_s are the heat capacities and k_f and k_s are the thermal conductivities of the film and the substrate, respectively, $Q(T)$ is the specific power of the Joule heating, x is the longitudinal coordinate (in the direction of the current), and y is the coordinate transverse to the surface of the film. It is assumed in Eq. (1) that, for a typical relationship of the parameters, $k_fD_s\gg k_sD_f$, the temperature of the film does not vary in the transverse direction, while the last term describes the heat dissipation from the film into the substrate. The specific power of the heating of the film by the transport current in the simplest approximation can be approximated by the step function[6] $Q(T)=(\rho I^2/W^2D_f^2)\,\eta(T-T_r)$, where ρ is the resistivity of the film in the normal state, I is the transport current, W is the width of the film, $T_r(I_c)$ is the temperature of the resistive transition, determined from the condition $I_c(T_r)=I$, and $\eta(x)$ is the Heaviside step function.

For typical ratios of the film and substrate parameters, $D_f\ll D_s$, $k_fD_f\ll k_sD_s$, and $C_fD_f\ll C_sD_s$, Eqs. (1) and (2) simplify.[5] Let us assume for simplicity that the temperature dependence of C_s and k_s can be neglected. Then, in a coordinate system comoving with the normal-phase front ($z=x+vt$), Eq. (2) takes the form

$$\frac{\partial^2T}{\partial z^2}+\frac{\partial^2T}{\partial y^2}-v\cdot\frac{C_s}{k_s}\cdot\frac{\partial T}{\partial z}=0,\quad 0<y<D_s, \tag{3}$$

while Eq. (1) and the condition of thermal stability of the reverse side of the substrate transform into the following boundary conditions on Eq. (3):

$$\left.\frac{\partial T}{\partial y}\right|_{y=0}=-\frac{\rho I^2(T_c-T_0)}{k_sD_fW^2[T_r(I)-T_0]}\cdot\eta(z),\quad T|_{y=D_s}=T_0. \tag{4}$$

Here T_c is the critical temperature. The conditions given by Eqs. (4) mean that, far from the normal-phase front, the HTSC film is in a homogeneous superconducting state [$T(z,0)=T_0$ for $z\to-\infty$] and a homogeneous normal state [$T(z,0)=T_0+\rho I^2D_s/k_sW^2D_f^2$ for $z\to\infty$], while the origin along the z axis is chosen so that the condition $T(0,0)=T_r(I)$ is satisfied. Equations (3) and (4) can be solved by separation of variables, which gives the following expression for the propagation rate v of the front:

$$1-2\xi=\sum_{k=0}^{\infty}\frac{1}{\lambda_k^2\sqrt{1+(2\lambda_kv_h/v)^2}}, \tag{5}$$

where $\lambda_k=\pi(2k+1)/2$, $v_h=k_s/C_sD_s$ is the characteristic thermal velocity, and $\xi=k_sD_fW^2[T_r(I)-T_0]/\rho I^2D_s$ is a dimensionless parameter that characterizes the ratio of the heat dissipated into the substrate at the normal-phase front to the Joule self-heating of the normal region. Equation (5) reduces

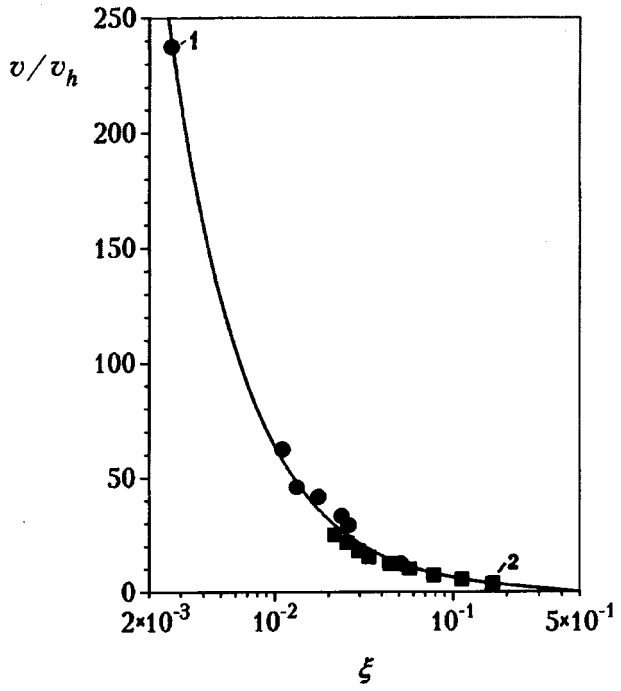

FIG. 1. Comparison of the theoretical dependence given by Eq. (5) with experimental data:[1,2] *1*—variation of temperature T_0 for a fixed current $I=1.33$ A; $D_s=5\times10^{-4}$ m, $C_s=9\times10^4$ J·m^{-3}K^{-1}, $k_s=20$ W·m^{-1}K^{-1}, $D_f=10^{-6}$ m, $W=1.5\times10^{-3}$ m, $T_c=85.8$ K, $\rho=4.5\times10^{-6}\Omega\cdot$m.[1] *2*—variation of current I at fixed temperature $T_0=78$ K; $D_s=5\times10^{-4}$ m, $C_s=2\times10^6$ J·m^{-3}K^{-1}, $k_s=10$ W·m^{-1}K^{-1}, $D_f=4\times10^{-7}$ m, $W=10^{-3}$ m, $T_c=87$ K, $\rho=5\times10^{-7}\Omega\cdot$m, $I_{c0}=1.7$ A.[2]

the dependence of the propagation rate v of the normal-phase front on numerous parameters to a universal relationship between v/v_h and ξ. In this case, v vanishes at $\xi=1/2$ and diverges at $\xi=0$. Note that the ''thermal'' velocity v_h is determined only by the properties of the substrate and can vary in a wide range from 10^{-2} to 1 m/sec.

In the case of a power-law dependence of the critical current on temperature, $I_c\propto(1-T/T_c)^n$, for the parameter ξ we have

$$\xi=(1-i^{1/n})/\alpha i^2, \tag{6}$$

where $\alpha=\rho I_{c0}^2 D_s/k_s D_f W^2(T_c-T_0)$ is the effective Steckley parameter of the film–substrate system, $i=I/I_{c0}$, and I_{c0} is the critical current at $T=T_0$.

Figure 1 compares the universal dependence given by Eq. (5) with the results of the experiments of Refs. 1 and 2. It demonstrates rather good agreement of the theoretical calculation with the experimental results. It should be pointed out that the experimental data shown in the figure were obtained on films with different values of n ($n=1$, Ref. 1 and $n=2$, Ref. 2) and different experimental methods (steady current flow over the film[2] and time-dependent resistive response of the film to short current pulses[1]) and for different measurement conditions (variation of current I for fixed T_0, Ref. 2, and variation of T_0 for fixed current amplitude I, Ref. 1). The universal relationship represented by Eq. (5) thus yields a satisfactory description of the experimental data on the rate of growth of thermal instability in an HTSC film when the data are obtained on different samples and under different experimental conditions.

We are grateful to V. N. Skokov for useful discussions of the results.

This work was carried out with the support of the GNTP ''Critical Directions in Condensed Media Physics'' (Project No. 96083) and the Russian Fund for Fundamental Research (Project No. 96-02-18949).

[1] Sh. K. Dhali and L. Wang, Appl. Phys. Lett. **61**, 1594 (1991).
[2] V. N. Skokov and V. P. Koverda, Sverkhprovodnost' (KIAE) **6**, 1646 (1993).
[3] V. N. Skokov and V. P. Koverda, Phys. Status Solidi A **142**, 193 (1994).
[4] M. O. Lutset and S. V. Klimov, Sverkhprovodnost' (KIAE) **7**, 1372 (1994).
[5] N. A. Buznikov and A. A. Pukhov, Pis'ma Zh. Tekh. Fiz. **22**, No. 12, 45 (1996) [Tech. Phys. Lett. **22**, 499 (1996)].
[6] A. Vl. Gurevich, R. G. Mints, and A. L. Rakhmanov, *The Physics of Composite Superconductors* [in Russian] (Nauka, Moscow, 1987).

Translated by W. J. Manthey
Edited by David L. Book

Adsorption-controllable channel conductivity in oxidized porous silicon

V. M. Demidovich, G. B. Demidovich, S. N. Kozlov, and A. A. Petrov

M. V. Lomonosov Moscow State University
(Submitted September 2, 1997)
Pis'ma Zh. Tekh. Fiz. **24**, 27–31 (January 26, 1998)

It is shown that an adsorption field acting on a silicon–oxidized-porous-silicon–metal structure can create a ''frozen'' state with conductivity increased by a factor of hundreds or thousands. The effect is associated with the modulation of the channel conductivity of oxidized silicon filaments of fractal material by ionic charge migrating along the surface of the oxidized layer. © *1998 American Institute of Physics.* [S1063-7850(98)02301-5]

The problem of new ways to make cheap, compact chemical sensors has become especially pressing in recent years in connection with the general worsening of the ecological situation. Porous materials have continued to attract the attention of investigators and developers of chemical sensors because of their large specific surface. Porous silicon is very promising in this regard, since it fits in well with modern microelectronics technology; moreover, it luminesces in the visible region.[1,2]

As is well known, one of the basic factors that determine the sensitivity of a semiconductor sensor to certain molecules is the concentration of free charge carriers.[3] By varying the electron and hole concentrations (for example, with an external electric field), it is possible in principle to tune a sensor to an adsorbate of a particular type. Unfortunately, an external electric field can be used to control the electrical properties of only the relatively small part of the surface of a porous material directly adjacent to an interphase boundary.

This paper proposes a new method of controlling the charge-carrier concentration in nanometer filaments of oxidized porous silicon (OPS), based on the use of ionic drift along the oxide ''shells'' of the crystal filaments of a fractal material.

A layer of porous silicon 7 μm thick was created on the (100) surface of *p*-type single-crystal silicon with a resistivity of 12 $\Omega\cdot$cm by electrochemical anodization in a mixture of a 48% HF solution with 96% ethanol (1:1) with a current density of 20 mA/cm^2. The oxide was grown on the surface of the porous layer by two-stage oxidation in dry oxygen; the first stage lasted 3 h at a temperature of 300 °C, and the second stage lasted 2 h at 730 °C. Two-step oxidation was carried out in order to prevent the porous layer from being sintered in the high-temperature stage.[4] After the oxidation, thermal sputtering in vacuum was used to deposit onto the surface of the porous layer metal contacts 1 mm in diameter and transparent to molecules of the gaseous medium. Before the measurements were made, the structures were subjected to a standard heat treatment in vacuum: They were baked at

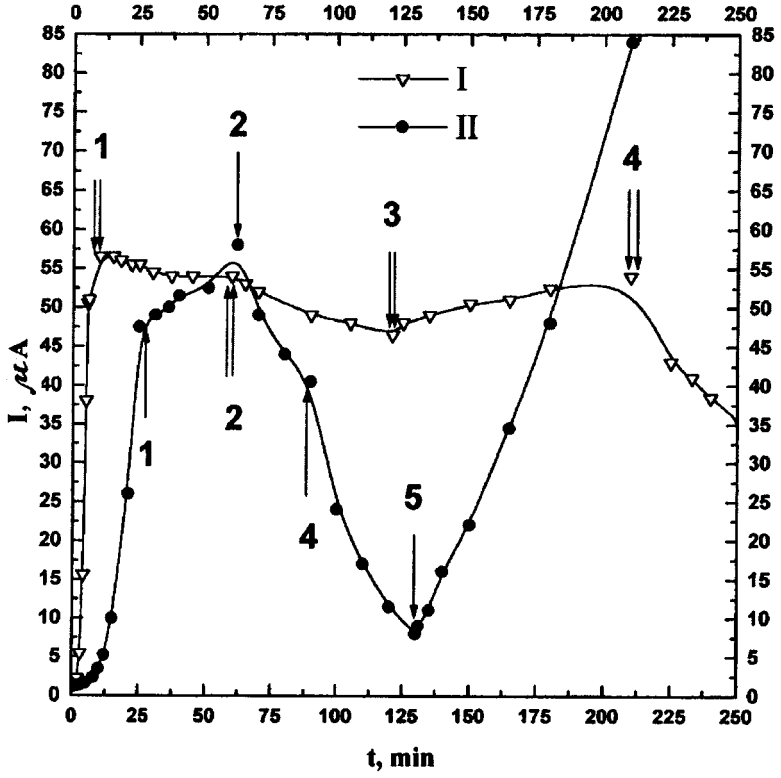

FIG. 1. Time dependence of the current through a Si–OPS–metal structure placed in ethanol vapor (I) and ammonia vapor (II) after applying a voltage of $V_g=-5$ V to the metal electrode and after the following procedures (the arrows show the time at which the corresponding procedures start): 1—evacuation with a voltage of $V_g=5$ V turned on; 2—bias switched off ($V_g=0$ V); 3, 5—switched on $V_g=-5$ V; 4—applied bias of $V_g=+5$ V. Vapor pressures: ethanol 8 Torr, ammonia 11 Torr.

 1063-7850/98/010053-02$15.00

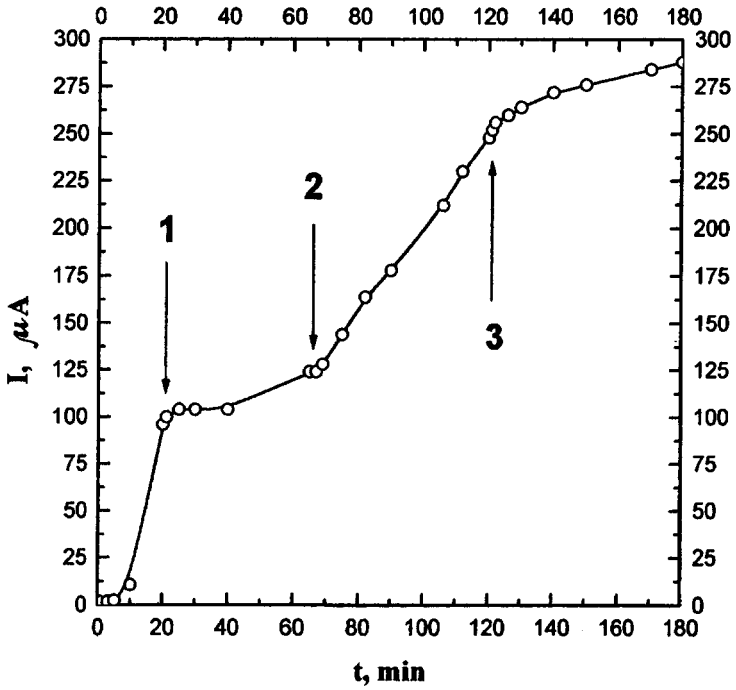

FIG. 2. Time dependence of the current through a Si–OPS–metal structure placed in ammonia vapor ($p=10$ Torr) after applying a voltage of $V_g=-5$ V to the metal electrode; subsequent evacuation at $V_g=-5$ V (1), admitting ethanol vapor ($p=0.6$ Torr) into the experimental chamber (2), and evacuation at $V_g=-5$ V (3).

210 °C in a vacuum of 10^{-5} Torr for 2 h. All the measurements were made at room temperature.

The possibilities of controlling the conductivity of the Si–OPS–metal system by means of adsorption-field effects are illustrated in Fig. 1. If a negative voltage of $V_g=-5$ V is applied at the initial instant to the metal electrode of the structure placed in ethanol or ammonia vapor, the current through the structure begins to increase. The rate of increase rises with the vapor pressure in the cell containing the sample (in vacuum with $V_g=-5$ V, the current remains unchanged for several hours). If the structure is held under voltage in ethanol or ammonia vapor for a sufficiently long time, the current can increase by several orders of magnitude. If the working cell is evacuated without removing the voltage ($V_g=-5$ V), the conductivity of the structure can either slowly increase or weakly decrease, depending on the specific conditions of the experiment (the surface state, the type of adsorbate). If the bias voltage is switched off ($V_g=0$), the rate at which the current through the structure decreases increases somewhat (Fig. 1). In this and the subsequent regimes, to measure the current through the structure, a voltage of $V_g=-5$ V is supplied at the metal electrode for a short time (on the order of seconds). With the opposite bias ($V_g=+5$ V), a rather rapid decrease of the conductivity of the structure was observed. If a voltage of $V_g=-5$ V was reapplied to the metal electrode, a rapid increase of the current through the structure was again produced.

These effects are evidently associated with the variation of the surface charge of nanocrystalline filaments of OPS because of the drift of ions along the oxide shell of nanocrystals of fractal silicon. When this happens, both the free charge-carrier concentration in the semiconductor core of the oxidized filament and their distribution along it vary. The ions appear when the molecules adsorbed on the surface of the OPS or the products of their interaction (for example, NH_4^+ and OH^- when ammonia is adsorbed onto the hydrated SiO_2 surface) dissociate. The dissociation process is apparently most intense along the perimeter of the metal electrode in the relatively higher ''edge'' electric field. When a negative voltage is applied to the metal electrode, negative ions accumulate on the surface of the filaments of the OPS, and this causes the silicon core of the filaments to be enriched with majority carriers (holes). When the cell with the sample is evacuated, the hydrate coating of the oxide is depleted and the surface mobility of the ions is reduced,[5] so that the surface charge is, as it were, frozen. Essentially, the structure can be ''formulated'' for molecules of a definite type by preliminary adsorption-field processing in the vapor of some other adsorbate (for example, ammonia) to specify virtually any required current level through the structure (and, consequently, the necessary concentration of free charge carriers in the fractal silicon, Fig. 2).

Preliminary adsorption-field processing of the Si–OPS–metal structure thus makes it possible to control the initial free charge-carrier concentration in silicon wires of fractal material. The proposed method for varying the surface charge of oxidized filaments of porous silicon can be useful not only for increasing the sensitivity and selectivity of chemical sensors based on porous silicon but also for controlling the luminescence parameters of porous silicon.

[1] L. T. Canham, Appl. Phys. Lett. **57**, 1046 (1990).
[2] Y. Kanemitsu, Phys. Rep. **263**, 1 (1995).
[3] F. F. Vol'kenshtein, *Physical Chemistry of Semiconductor Surfaces* [in Russian] (Nauka, Moscow, 1973).
[4] G. Bomchil and A. Halimaoui, Appl. Surf. Sci. **41/42**, 604 (1989).
[5] S. N. Kozlov and M. L. Slavova, Mikroelektronika **14**, 556 (1985).

Translated by W. J. Manthey
Edited by David L. Book

Stochastic self-oscillations of the surface photoelectromotive force

V. A. V'yun

Institute of Semiconductor Physics, Siberian Branch, Russian Academy of Sciences, Novosibirsk
(Submitted June 4, 1997)
Pis'ma Zh. Tekh. Fiz. **24**, 32–36 (January 26, 1998)

This paper describes for the first time the experimental observation and study of stochastic self-oscillations of the surface photoelectromotive force. A layered metal–insulator–semiconductor–metal structure available to most investigators is chosen, and new nonlinear properties are detected in it. © *1998 American Institute of Physics.* [S1063-7850(98)02401-X]

Stochastic self-oscillations, or dynamic chaos, are attracting the attention of investigators in various areas.[1–4] As usual, there is interest in new systems in which this phenomenon manifests itself. This paper presents the results of an experimental study of stochastic self-oscillations detected in the surface photoelectromotive force. This type of self-oscillations has not been described earlier (in particular, not even in the detailed monograph of Ref. 5).

The experimental layout of the study is shown in Fig. 1. It used the simplest layered metal–insulator–semiconductor–metal structure, in which it was possible to replace the semiconductors. Semiconductor *1* was an *n*-type silicon plate with resistivity 4 kΩ·cm, insulator *2* was a polished glass plate 1 mm thick, and electrodes *3* were metal foil. The lower electrode contained a slit for illuminating the surface of the semiconductor with LED *4*. The illumination was produced by an AL102A red LED, which, when supplied with an ac voltage, can generate light of the intensity being modelled.

In the test structure, when the surface of the semiconductor was illuminated with an LED, the resulting voltage of the capacitive photoelectromotive force was taken off the capacitive electrodes and was fed to the input of low-frequency amplifier *5*. The voltage from the amplifier, in turn, was fed through a resistor with $R=110\ \Omega$ to the LED. To select the working point of the LED, dc voltage V_g was also supplied to it through another resistance with $R=110\ \Omega$. Only regular self-oscillations of the photoelectromotive force were observed earlier in a similar circuit with such external negative feedback.[6–8] Such self-oscillations, whose frequencies are in the kilohertz range, are based on the relaxation properties of the capacitive surface photoelectromotive force. They are of interest for a high-precision, sensitive study of the relaxation of electronic processes on a semiconductor surface and for the construction of environmental sensors.

The experiments were done at room temperature. To study the character of the self-oscillations, the spectral dependence and the phase portrait for a photoelectromotive force of V_p at the output of the amplifier were recorded. The spectral dependence in this case was obtained by means of a spectrum analyzer, and the phase portrait was obtained from an oscilloscope whose vertical and horizontal plates were driven by signal V_p and its derivative with respect to time, respectively.

Stochastic self-oscillations of the photoelectromotive force were detected using semiconductors with a surface obtained after etching and natural oxidation in air at room temperature. When this was done, the majority charge carriers were depleted on the surface. This promoted the appearance of a large photoelectromotive force, which possessed the necessary relaxation properties when the illumination was turned on and off.

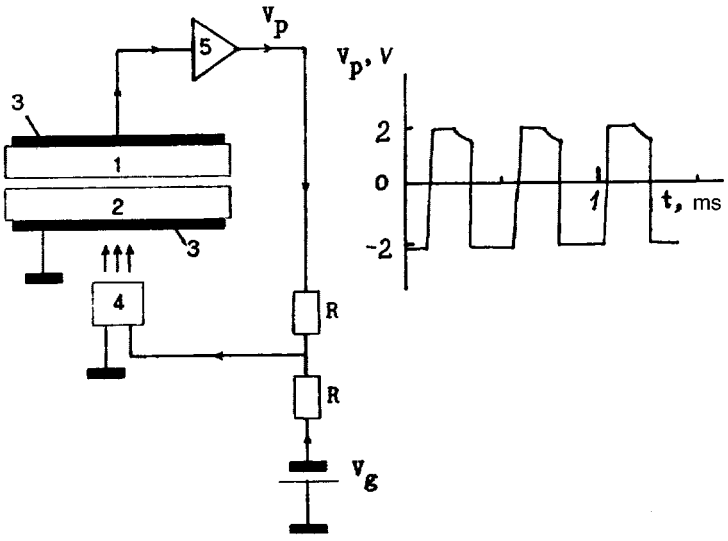

FIG. 1. Schematic of the experimental setup: *1*—semiconductor plate, *2*—insulator plate, *3*—electrodes, *4*—LED, *5*—low-frequency amplifier. (The inset on the right shows an oscilloscope tracing of the photoelectromotive force signal V_p for $K=90$ dB and $V_g=-6$ V.)

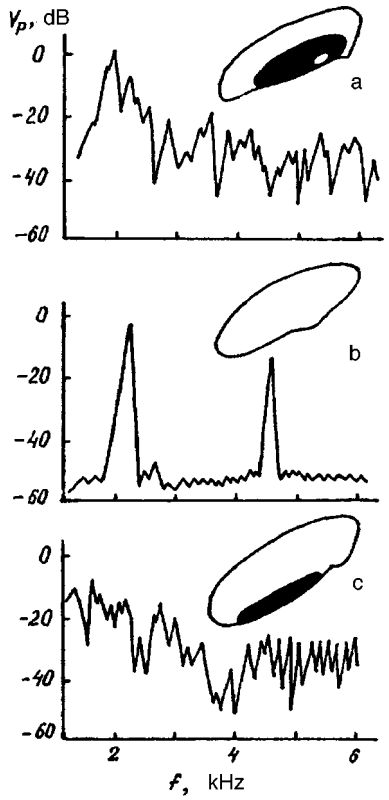

FIG. 2. Spectral dependence and phase portraits (in the upper parts of the figures) for the photoelectromotive force signal V_p for $K=90$ dB and a dc voltage of $V_g=0$ V (a), -6 V (b), and -10 V (c).

In the circuit considered here, a different type of self-oscillations appeared with the appropriate values of the gain K of the amplifier and dc voltage V_g. Thus, no self-oscillations were observed for K less than 60 dB, whereas regular quasi-harmonic self-oscillations were established when K ranged from 60 to 80 dB. When the gain K was increased further, strongly nonlinear and stochastic self-oscillations appeared. For $K=90$ dB, Figs. 2a–2c show an example of the spectral dependence and phase portraits for the photoelectromotive force signal V_p as the voltage V_g was increased. It is characteristic that strongly nonlinear regular self-oscillations appeared for a voltage V_g lying in the range -3 to -8 V. For $V_g=-6$ V, the inset to Fig. 1 shows the oscilloscope tracing of the photoelectromotive force signal V_p, and Fig. 2b shows its spectral dependence and phase portrait. The spectral dependence is characterized by the presence of the fundamental and higher harmonics, while the phase portrait is a closed curve (a stable attractor). However, for $V_g=0$ (Fig. 2a) and $V_g=-10$ V (Fig. 2c), the presence of the fundamental and the higher harmonics are already hard to make out. Stable and unstable (strange) attractors are seen on the phase portrait of the self-oscillations. The former is represented by the outer closed curve, while the latter is shown by the complex dark region, which the system most probably ''cross-hatches'' as it rotates around zero. In this case, the system for some part of the time leads to a stable attractor and is then disrupted and makes a transition to an unstable attractor. Such a transition from a regular regime of self-oscillations to a stochastic regime is characteristic of the scenario of a transition from regular to stochastic self-oscillations and back.[1–5,9]

To understand stochastic self-oscillations, it is not sufficient to use the phenomenological model of Refs. 6–8, which allows for surface states with a single nonequilibrium-charge relaxation time and explains regular self-oscillations of the photoelectromotive force. This is because the phase space of the system considered in this case is two-dimensional, and only regular self-oscillations are possible in it.[1–5] To explain the observed stochastic self-oscillations, it is apparently necessary to allow for several types of surface states of the semiconductor, so that the phase space of the system will have large dimensionality.

This work was supported by the Russian Fund for Fundamental Research (Grant No. 96-02-19393).

[1] H. Haken, *Synergetics, an Introduction: Nonequilibrium Phase Transitions and Self-Organization in Physics, Chemistry, and Biology, 3rd ed.* (Springer, Berlin, 1983); *Advanced Synergetics: Instability Hierarchies of Self-Organizing Systems and Devices* (Springer, Berlin, 1983).
[2] Yu. I. Neimark and P. S. Landa, *Stochastic and Chaotic Fluctuations* (Dordrecht; Kluwer Academic Publishers, Boston, 1992).
[3] H. G. Schuster, *Deterministic Chaos* (Physik-Verlag, Weinheim, 1984; Mir, Moscow, 1989).
[4] A. S. Dmitriev and V. Ya. Kislov, *Stochastic Fluctuations in Radiophysics and Electronics* [in Russian] (Nauka, Moscow, 1989).
[5] E. Scholl, *Nonequilibrium Phase Transitions in Semiconductors: Self-Organization Induced by Generation and Recombination Processes* (Springer, Berlin, 1987).
[6] V. A. V'yun, Poverkhnost' No. 6, 73 (1991).
[7] V. A. V'yun, in *Proceedings of the IEEE International Frequency Control Symposium*, 1993, p. 509–513.
[8] V. A. V'yun, Lith. Phys. J. **35**, 478 (1995).
[9] P. Mannevile and Y. Pomeau, Physica D **1**, 219 (1980).

Translated by W. J. Manthey
Edited by David L. Book

Electronic redistribution in the neighborhood of the nucleus of a linear dislocation

R. M. Peleshchak and B. A. Lukiyanets

Drogobych Pedagogical Institute, Lviv Polytechnical State University
(Submitted February 5 1997; revised June 16, 1997)
Pis'ma Zh. Tekh. Fiz. **24**, 37–41 (January 26, 1998)

This paper is devoted to a self-consistent solution of the electron–strain interaction in a crystal with linear dislocations. It shows that such self-consistency causes charge to be redistributed in the neighborhood of the dislocation nucleus and hence renormalizes the strain caused by the dislocation. The resulting charge redistribution forms a dipole whose moment is proportional to the length of the dislocation. The dislocation kinetics in the crystal can be affected when an external dynamic or static electric field acts on such a dipole.
 [S1063-7850(98)02501-4]

There are currently two basic models of electronic dislocation states for uncharged dislocations: the broken-bond model,[1] which takes into account the short-range potential of broken covalent bonds in the dislocation nucleus, and the strain-potential model.[2,3] However, the electron–strain interaction is not taken into account self-consistently in these models, and the character of the filling of the electron energy bands is neglected. This paper is devoted to the solution of such a self-consistent problem in a crystal with a linear dislocation. For this purpose, we use a model in which the state of the conduction electrons of an isotropic metal is described by a single orbitally nondegenerate band. The strain created by mechanical stress $\sigma_m(\mathbf{r})$ can cause such a band to shift in energy. The Hamiltonian that includes such an effect has the form (see Refs. 5 and 6)

$$H=\sum_{i\sigma}\,[\omega+SU(\mathbf{r}_i)]c_{i\sigma}^{+}c_{i\sigma}+\sum_{ij\sigma}\,\lambda_{ij}^{0}c_{i\sigma}^{+}c_{j\sigma}+\frac{1}{2}\sum_{i}\,K\Omega_0U^2(\mathbf{r}_i)+H_c\,. \tag{1}$$

Here $c_{i\sigma}$ ($c_{i\sigma}$) is the Fermi creation (annihilation) operator of an electron with spin σ in a localized Wannier state i, ω is the energy that characterizes the position of the center of the electron band, λ_{ij}^{0} is the electron-mixing integral in an undeformed lattice, S describes the shift of the conduction band during strain, K is the elastic stiffness of the lattice, $U(\mathbf{r}_i)=\mathrm{Tr}\hat{U}(\mathbf{r}_i)=(\Omega-\Omega_0)/\Omega_0$ is the strain parameter that describes the relative change of the volume of the cell because of the dislocation (Ω_0 is the initial volume of the unit cell), and H_c is the Hamiltonian of the Coulomb electron–electron interaction.

To determine the strain parameter $U(\mathbf{r})$, we use the condition of mechanical equilibrium,[7]

$$\left\langle\frac{\partial H}{\partial U(\mathbf{r})}\right\rangle=\sigma_m(\mathbf{r})V, \tag{2}$$

where V is the volume of the crystal. Using Eq. (1), we get from this that

$$U(\mathbf{r})=-\frac{S}{K\Omega_0}\sum_{kk'\sigma}\,\langle c_{k\sigma}^{+}c_{k'\sigma}\rangle\exp[-i(\mathbf{k}-\mathbf{k}')\mathbf{r}]+U_m(\mathbf{r}). \tag{3}$$

As follows from Eq (3), the strain parameter consists of an electronic part and a mechanical part $U_m(\mathbf{r})$. In the case under consideration of a linear dislocation with the line of the dislocation along the Z axis and the X axis along the Burgers vector, it is convenient to represent $U_m(\mathbf{r})$ in a cylindrical coordinate system with polar coordinates in the XOY plane in the form

$$U(\rho,\varphi,z)=\mathrm{Tr}\hat{U}_m=\begin{cases}D\dfrac{\sin\,\varphi}{\rho}, & \rho\geqslant\rho_0\\[2ex] \dfrac{D}{\rho_0^2}\rho\,\sin\,\varphi, & \rho\leqslant\rho_0\end{cases}. \tag{4}$$

(Here D is a constant, ρ_0 is the radius of the dislocation nucleus, equal to $(1–2)a$, and a is the lattice constant.) The expression for $U_m(\rho,\varphi,z)$ in the region $\rho\geqslant\rho_0$ is obtained from the expression for the mechanical stress $\sigma_m(\rho,\varphi,z)$ proposed in Ref. 4; $U_m(\rho,\varphi,z)$ in the region $\rho\leqslant\rho_0$ is the approximation of Ref. 8.

The computation of the electronic component of the strain parameter in Eq. (3) reduces to determining the correlator $\langle c_{k\sigma}^{+}c_{k'\sigma}\rangle$, which was done with the help of the single-frequency Green's function. In general, the problem reduces to solving a system of five equations for: (1) the concentration of conduction electrons, (2) the electrostatic potential that results from the electron-density change $\Delta n(\rho,\varphi,z)=n(\rho,\varphi,z)-n_0$ in the neighborhood of the dislocation (n_0 is the mean concentration of electrons arriving at a lattice point, taking into account the electron–strain interaction),[6] (3) the wave function of an electron in the neighborhood of a defect, (4) the Green's function, and (5) the chemical potential. This system of equations was solved by the method of successive approximations at $T=0$ K. The mechanical part of the strain parameter was taken as the zeroth approximation.[5,6] The dependence $\Delta n(\rho,\varphi,z)$ was obtained as a result of the computations. Figure 1 shows a family of curves $\Delta n(\rho,\varphi,z)$ for various angles φ in the plane $z=\mathrm{const}$ [the $\Delta n(\rho,\varphi,z)$ curves for $\varphi\in[0,\pi]$ are shown on the left, and those for $\varphi\in[\pi,2\pi]$ are shown on the right]. As follows from the figure, this dependence is antisymmetric relative to the dislocation. Since the electronic

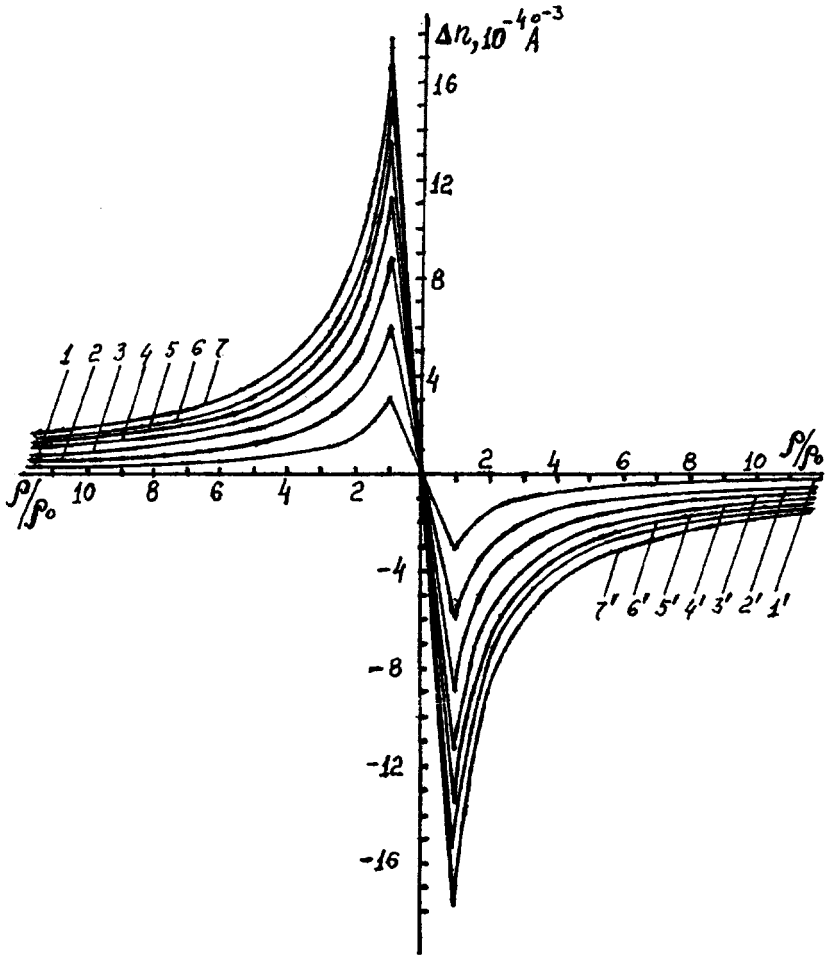

FIG. 1. Family of $\Delta n(\rho)$ curves for various values of φ (on the left for $\varphi \in [0,\pi]$ and on the right for $[\pi,2\pi]$) with $S=4.0$ eV, $n_0=10^{-5}$ Å^{-3}, and $K=0.47$ eV·Å^{-3}. Curves *1* for $\varphi=10°$ and 170° (*1′* for 190 and 370°), *2*—20 and 160° (*2′*—200 and 160°), *3*—*30* and 150° (*3′*—210 and 350°), *4*—40 and 140° (*4′*— 220 and 340°), *5*—50 and 130° (*5′*—240 and 320°), *6*—70 and 110° (*6′*—250 and 310°), *7*—90° (*7′*—270°).

component of the strain parameter equals $-S\Delta n(\rho,\varphi,z)/K$, it has the same character as does $\Delta n(\rho,\varphi,z)$ to within a sign and a constant factor.

The resulting charge redistribution makes it possible to give a more definite picture of the electronic dislocation states proposed in Ref. 9. Whereas, according to Ref. 9, a dislocation nucleus in a semiconductor crystal can either accumulate charges on itself or liberate them, according to our results, the dislocation possesses both properties. In the case considered above of an isotropic crystal, excesses and deficiencies of electrons (by comparison with the mean energy in the crystal) occur along the dislocation axis antisymmetric from it. A dipole is thus formed, whose moment **p** can easily be estimated. It will equal

$$\mathbf{p}=e\int\int\int \Delta n(\rho,\varphi,z)\rho d\rho d\varphi dz \tag{5}$$

(the integration over z is chosen along the dislocation axis). Consequently, **p** in this case will be proportional to the length of the dislocation axis. The presence of such a dipole moment can be used, in particular, to affect the kinetics of the dislocations in a crystal by superimposing an external electric field on them. Actually, because of polarization, according to the conclusions stated above, such a field can alter the electronic component of the stress σ. It is well known[9] that the dislocation rate v is associated with the stress σ and the temperature T by

$$v=v_0\left(\frac{\sigma}{\sigma_0}\right)^m \exp\left(-\frac{E}{kT}\right), \tag{6}$$

where v_0 and σ_0 are constants, $m=1-2$, and E is the activation energy. A change in σ thus directly affects v. It is possible that such changes are reflected in some way in the activation energy. It can be assumed that the effect of interacting with an external electric field will depend on its orientation relative to the dislocation and on whether the field is static or dynamic. These assumptions require additional study and lie outside the framework of this paper.

[1] W. Shockley, Phys. Rev. **91**, 228 (1953).
[2] I. M. Lifshits and Kh. I. Pushkarev, JETP Lett. **11**, (1970).
[3] M. A. Razumova and V. N. Khotyaintsev, Fiz. Tverd. Tela **31**, No. 2, 275 (1989) [Sov. Phys. Solid State **31**, 275 (1989)].
[4] A. M. Kosevich, *Theory of the Crystal Lattice* [in Russian] (Visha Shkola, Kharkov, 1988).
[5] R. M. Peleshak, ''Electronic states of the lattice strain of a crystal in the presence of point defects,'' Preprint-69-5R Inst. Tekh. Fiz. Akad. Nauk USSR, Kiev, 1989.
[6] I. V. Stasyuk and R. M. Peleshak, Ukr. Fiz. Zh. **36**, 1744 (1991).
[7] L. D. Landau and E. M. Lifshitz, *Theory of Elasticity* (Nauka, Moscow, 1965; Pergamon Press, Oxford, 1959).
[8] Yu. V. Kornyushin and S. I. Pekar, Fiz. Tverd. Tela (Leningrad) **6**, 1122 (1964).
[9] T. Suzuki, S. Takeuchi, and H. Yoshinaga, *Dislocation Dynamics and Plasticity* (Springer-Verlag, New York, 1991; Mir, Moscow, 1989).

Translated by W. J. Manthey
Edited by David L. Book

Effect of magnetic anisotropy on the mobility of the boundaries in thin magnetic films

V. I. Beresnev, B. N. Filippov, and L. G. Korzunin

Institute of the Physics of Metals, Ural Branch, Russian Academy of Sciences, Ekaterinburg
(Submitted January 29, 1997; revised October 28, 1997)
Pis'ma Zh. Tekh. Fiz. **24**, 42–46 (January 26, 1998)

This paper discusses the effect of magnetic crystallographic anisotropy on the mobility of the domain walls in thin magnetic films with an easy axis in the plane of the film. It shows that the stable configuration of a domain wall is a single-vortex Bloch domain wall. Besides this, there are two metastable states of the domain wall—a Néel domain wall and a domain wall with two magnetic vortices along the normal to the plane of the film. It is also shown that the mobilities of the single-vortex and Néel domain walls and the domain wall with two vortices decrease as the anisotropy constant increases and tend to the same value. © *1998 American Institute of Physics.* [S1063-7850(98)02601-9]

It is well known[1–3] that the domain walls in thin magnetic films with their easy axis parallel to the film surface can have a two-dimensional or a one-dimensional distribution of the magnetization vector. The goal of this paper is to study how the bulk crystallographic anisotropy affects the structure and mobility of the domain walls in thin magnetic films.

Consider a thin magnetic film with a thickness of h and with its easy axis parallel to the surface of the plate. Let us draw the z axis along the easy axis and assume that the distribution of the magnetization vector $\mathbf{M}$ in the domain wall that separates domains magnetized along $\pm z$ depends only on x and y (the x axis is perpendicular to the plane of the domain wall). Then the energy-density functional W is written as

$$W=\int_0^h dy\int_{-\infty}^{\infty} dx\{(A/M^2)[(\partial\mathbf{M}/\partial x)^2+(\partial\mathbf{M}/\partial y)^2] -(K/M^2)(\mathbf{Mc})-0.5\mathbf{MH}^m\}. \quad (1)$$

Here A is the exchange-interaction parameter, K is the magnetic anisotropy constant, M is the saturation magnetization, $\mathbf{c}$ is the unit vector along the easy axis, and $\mathbf{H}^m$ is the magnetostatic field.

We find the structure of the domain wall by numerically minimizing Eq. (1) (see Ref. 4 for more details). The quantity K was varied from 10^2 to 10^6 erg/cm^3. The other parameters were $A=10^{-6}$ erg/cm, $M=800$ Gs, and $h=10^{-5}$ cm.

Numerical calculations showed that the stable configuration of the domain wall as K varies is the well known single-vortex Bloch domain wall.[1,2] The formation of vortex distributions of $\mathbf{M}$ provides the minimum density of volume magnetic charges ($\mathrm{div}\mathbf{M}\Rightarrow 0$) and gives the best description of the properties of the exchange-interaction operator. Besides the single-vortex Bloch domain wall, there are two metastable states of the domain wall. One of them is a two-vortex asymmetric Néel domain wall.[1] The other—obtained by us for the first time (in a film of the given thickness)—is a two-vortex asymmetric domain wall, with the two vortices aligned along a normal to the film surface. As an example, Fig. 1 shows the domain wall structures for $K=10^3$ erg/cm^3. We associate the appearance of a two-vortex asymmetric domain wall as a metastable state with the fact that, for a thick enough film, two magnetization-vector vortices can be symmetrically localized in the surface of a film, in contrast with the two-vortex Néel domain wall (compare Figs. 1b and 1c). Note that the magnetostatic energy is approximately identical in the two-vortex asymmetric domain wall and the two-vortex Néel domain wall, but the exchange energy is greater in the two-vortex asymmetric domain wall. This is because the effective size of the vortex is greater in a two-vortex Néel domain wall. The results of calculations show that, as K increases, the energies of all three domain-wall configurations increase and gradually converge. Thus, for $K=10^3$ erg/cm^3, the reduced energies are $\varepsilon=W/2A$ equal ε (single-vortex Bloch domain wall)$=10.04$, ε (two-vortex Néel domain wall)$=12.85$, and ε(two-vortex asymmetric domain wall)$=17.98$, whereas, for $K=10^6$ erg/cm^3, ε (single-vortex

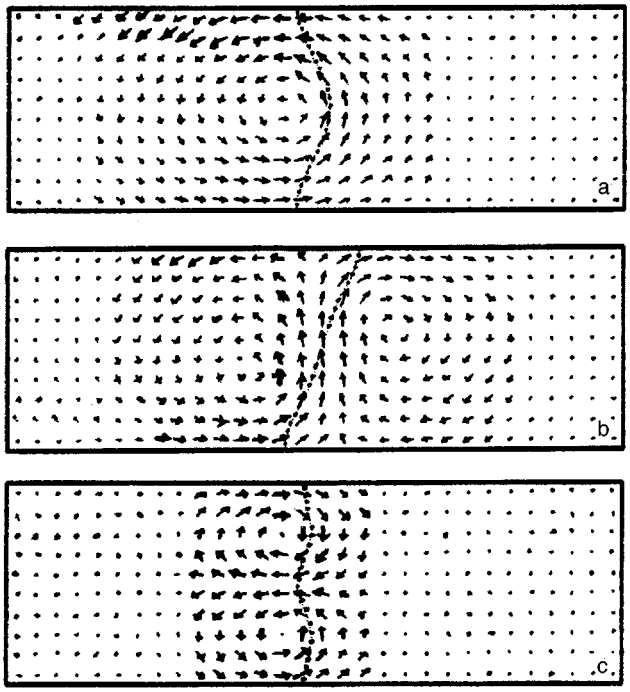

FIG. 1. Domain-wall structure for $A=10^{-6}$ erg/cm, $K=10^3$ erg/cm^3, $h=10^{-5}$ cm, and $m=800$ G. (a) single-vortex Bloch domain wall, (b) two-vortex Néel domain wall, and (c) two-vortex asymmetric domain wall.

 1063-7850/98/010059-02$15.00

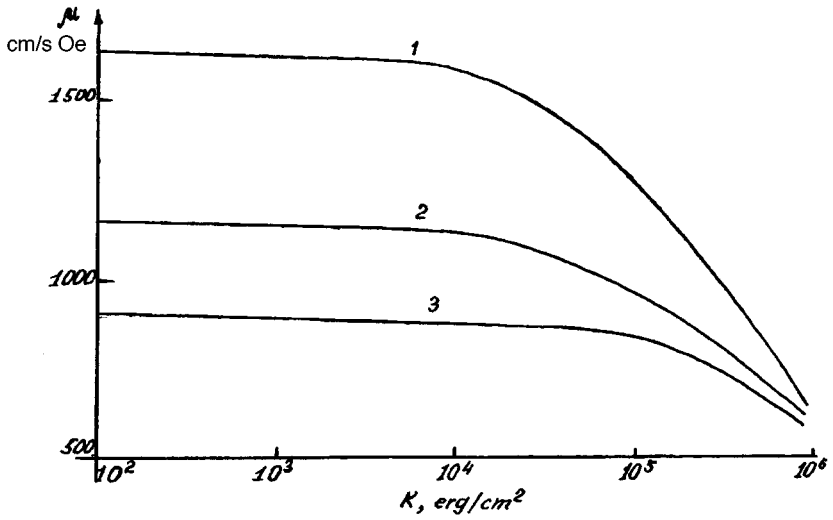

FIG. 2. Domain-wall mobilities vs anisotropy constant: *1*—single-vortex Bloch domain wall, *2*—two-vortex Néel domain wall, and *3*—two-vortex asymmetric domain wall.

Bloch domain wall)=25.18, ε (two-vortex Néel domain wall)=25.34, and ε (two-vortex asymmetric domain wall) =28.6. The energies of the single-vortex Bloch domain wall and the two-vortex Néel domain wall converge because the contribution of the anisotropy energy in the single-vortex Bloch domain wall increases by comparison with the two-vortex Néel domain wall. As K increases, the distribution of the magnetization vector in the domain wall varies in such a way that the effective width of the domain wall decreases.

We also considered the steady-state motion of the domain wall and calculated its mobility μ as K varies. In the limit of low domain wall velocity, μ can be determined by using the structure of static walls, which is found by minimizing the functional of Eq. (1), with[5]

$$\mu = 2h\gamma/\alpha I, \tag{2}$$

$$I = M^{-2}\int_0^h dy \int_{-\infty}^{\infty} dx(\partial \mathbf{M}/\partial x)^2, \tag{3}$$

where γ is the gyromagnetic ratio, and α is the Gilbert damping parameter.

Figure 2 shows the dependences of the mobilities of the single-vortex Bloch, two-vortex Néel, and two-vortex asymmetric domain walls, calculated from Eqs. (2) and (3) and on the basis of the distribution of the magnetization vector in the domain wall obtained for each value of the anisotropy constant K. Note that, for a Bloch domain wall in an infinite crystal, the mobility of the boundary depends on K as $K^{1/2}$. As can be seen from the figure, the mobility of the domain walls decreases with increasing K, which should be expected, but the change of μ is small in the K interval $10^2-/10^4$ erg/cm^3. This behavior of $\mu(K)$ is associated with the fact that, as calculations show, the fine structure of the domain wall is weakly dependent on K in the indicated interval of K values.

The mobilities of the single-vortex Bloch, two-vortex Néel, and two-vortex asymmetric domain walls decrease for large K, but the $K^{-1/2}$ dependence is not clearly followed. The exchange energies of all three domain-wall configurations are similar in magnitude for $K=10^6$ erg/cm^3, and therefore their mobilities are not very different, since, according to Eqs. (2) and (3), the value of μ is determined by a coefficient proportional to the part of the exchange energy given by Eq. (3).

Thus, numerical minimization of the domain-wall energy functional has been used to determine the fine structure of the domain wall in terms of a model of the two-dimensional magnetization-vector distribution as a function of the anisotropy constant. A new metastable domain-wall state has been found, with two vortices localized on the surfaces of the film. The steady-state motion of the domain wall has been considered, and its mobilities as K varies have been calculated.

This work was carried out with the partial support of the RFFR (Grant 96–02–16000).

[1] A. E. La Bonte, J. Appl. Phys. **40**, 2450 (1969).
[2] A. Hubert, Phys. Status Solidi A **32**, 519 (1969).
[3] A. Aharoni, Phys. Status Solidi A **18**, 661 (1973).
[4] B. N. Filippov and L. G. Korzunin, Fiz. Met. Metalloved. **75**, 49 (1993).
[5] B. N. Filippov, L. G. Korzunin, and V. I. Beresnev, Fiz. Met. Metalloved. **80**, 31 (1995).

Translated by W. J. Manthey
Edited by David L. Book

(111)⇒(001) orientational phase transitions and nature of the insulating state in BiSrCaCuO (2212 and 2223) films

V. D. Okunev and Z. A. Samoĭlenko

Physicotechnical Institute, Ukrainian National Academy of Sciences, Donetsk
(Submitted May 6, 1997)
Pis'ma Zh. Tekh. Fiz. **24**, 13–20 (January 12, 1998)

The influence of the growth temperature T_s on the structure, optical absorption, and electrical conductivity of BiSrCaCuO films has been studied. It was observed that nonmonotonic changes in the parameters of the films with T_s are caused by (111)⇒(001) phase transitions at $T_s \approx 550$ °C for the 2212 phase and $T_s \approx 600$ °C for the 2223 phase. These phase transitions stimulate the formation of metallic conductivity and are caused by a change in the system of preferential ordering planes of the atoms. © *1998 American Institute of Physics.* [S1063-7850(98)00301-2]

It is well known[1,2] that the parameters of high-temperature superconductors are sensitive to changes in technology or to external influences because of the nature of the free carriers and the possibility that inhomogeneities can easily form in the bulk of the samples. Changes in the hole concentration are mainly associated with the state of the oxygen subsystem. The nature of the inhomogeneities can also be considered to be well studied and they are mainly attributed to the formation of inclusions of simpler composition and phase structure having insulating properties or a lower T_c. However, our earlier experimental data[3–6] indicated that there may be a slightly different relation between the structural characteristics and the electrical properties of high-temperature superconductors: the appearance of (111) lines on the x-ray diffraction patterns was generally accompanied by an increase in the resistivity of the films and a deterioration in the critical parameters of the samples. Here we analyze this problem by studying the relation between the structure of the films and their electrical conductivity. A fairly broad spectrum of structural states may be achieved by varying the growth temperature of the films which is always one of the main parameters of any film technology. Thus, the problem reduced to studying the influence of the growth temperature on the structure and electrical conductivity of the films.

We studied the structure, and the electronic and optical properties of BiSrCaCuO (2212 and 2223) films obtained by dc sputtering of stoichiometric targets in air.[7] The air pressure in the working chamber was 2–3 Torr. The films were grown on MgO [on the (100) cleavage plane] or Al_2O_3 substrates [(1102) plane]. The film thicknesses were 0.3–0.5 μm, for which it was shown in Ref. 4 that, under optimum conditions, the crystal field of the substrate and the stresses at the film-substrate interface effectively influenced the growth of textured layers. The fraction of the material volume in the state with metallic conductivity was determined by an optical absorption technique[8–10] using those parts of the spectrum attributable to absorption by free carriers[8,11,12] and the dependence $\alpha \sim C_m p$, where α is the absorption coefficient, C_m is the concentration of the metallic phase, and p is the hole concentration. The measurements of C_m were made fairly far from the fundamental absorption edge, in the range of quantum energies $\hbar\omega < 1.2$ eV, where the contribution of interband optical transitions to α can be neglected.[11] The relative changes in the hole concentration were determined from the change in the position of the Fermi level.[8,10] These data were compared with the results of an x-ray structural analysis, using long-wavelength Cr K_α radiation. The bulk fraction of atomic groupings represented by the 001 diffraction peaks was estimated using the relation: $C_{001} = K \times I_{001}/I_{\text{coh}}$, where $I_{\text{coh}} = I_{001} + I_{111}$, K is a coefficient which is equal to the ratio of the coherent and incoherent x-ray scattering intensities, and I are the integrated intensities.

Figures 1 and 2 give the electrical conductivity ($T = 300$ K) of the films as a function of the substrate temperature T_s. The results were obtained for moderate interaction between the gas-discharge plasma and the growth surface.[7] Under these conditions, the 2223 films exhibit an amorphous state in the range $T_s \leqslant 400$ °C (Fig. 1). The growth of crystalline layers begins at 450 °C. In the (2212) system, which has a simpler structure, a crystalline structure begins to form at substantially lower temperatures—in the range $T_s = 200–250$ °C (Fig. 2). Taking into account the different stability of the amorphous state of these two phases, we can see that the changes in $\sigma = \sigma(T_s)$, which cover a range exceeding ten orders of magnitude, are qualitatively the same for the 2212 and 2223 systems and do not depend on the type of substrate. These changes are abruptly nonmonotonic. Their characteristics within the range of existence of the amorphous phase for 2223 films and the influence of the initial state on the critical parameters of the samples following an amorphous–crystal transition under high-temperature annealing were discussed in Refs. 3, 4, and 6.

Textured superconducting layers grow in the temperature range 690–710 °C only on MgO substrates. As a result of intensive chemical interaction between BiSrCaCuO and Al_2O_3, the layers deposited on sapphire substrates without a buffer sublayer remain in the insulating state over the entire range of T_s. Textured superconducting layers on sapphire substrates can be achieved under conditions of active interaction between the gas-discharge plasma and the growth

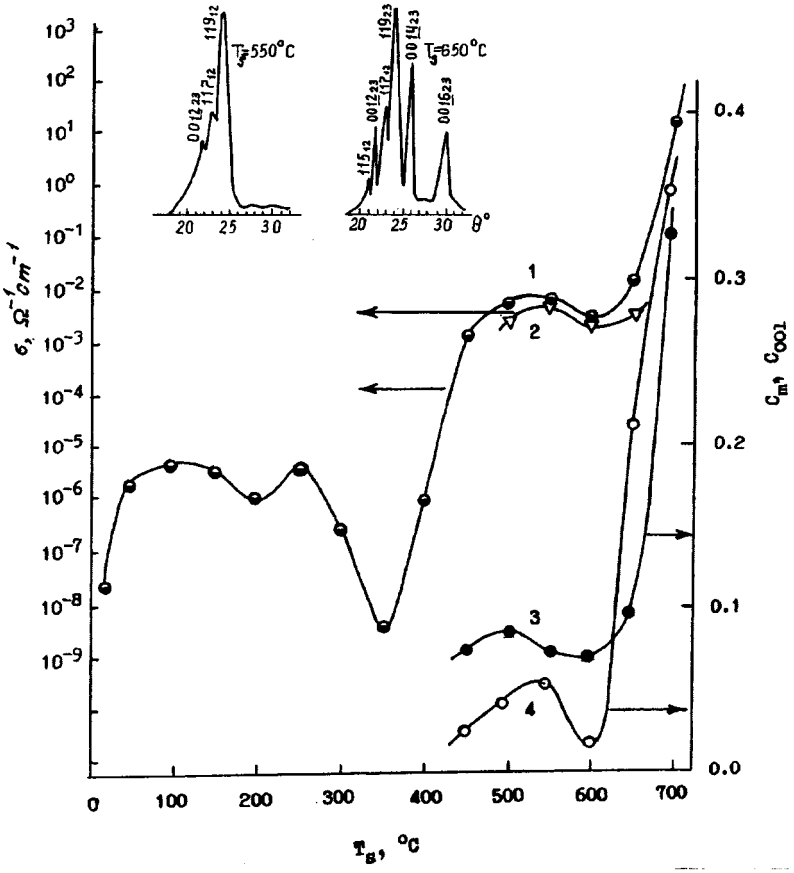

FIG. 1. Parameters of 2223 films versus growth temperature: *1*—electrical conductivity of films ($T=300$ K) on MgO substrates; *2*—electrical conductivity of films ($T=300$ K) on Al_2O_3 substrates; *3*—concentration of the metallic phase C_m in films on MgO from optical absorption data; *4*—concentration of material represented by 001 groups (C_{001}) in films on MgO from results of x-ray structural analyses. The inset shows x-ray diffraction patterns of films on MgO near the orientational phase transition.

surface[7] for which the deposition temperature can be reduced from ~700 to 400 °C (Ref. 13).

In our case, the most interesting ranges of variation of T_s are $250<T_s<700$ °C for 2212 films and $400<T_s<700$ °C for 2223 layers, in which the atomic order of the crystalline films is characterized by constant competition between two types of packing. In one case, the atoms are ordered preferentially in the (111) planes whereas in the other case, they are ordered in the (001) family which is responsible for the conductivity and superconductivity of high-temperature superconductors.

Curves *4* in Figs. 1 and 2 give the concentration of atoms in groups characterized by 001 reflection (C_{001}) as a function of the growth temperature T_s of the films. Studies of the diffraction patterns of the films (insets to Figs. 1 and 2) indicated that the nonmonotonic behavior of the curves $C_{001}=C_{001}(T_s)$ is attributable to a structural phase transition at $T_s\simeq 550-600$ °C when the dominant type of forming crystallographic planes changes. For 2223 films this point is observed near $T_s\simeq 600$ °C: for $T_s<600$ °C (111) planes dominate in the structure while for $T_s>600$ °C, the (001) planes dominate. For the 2212 phase the critical point is shifted 50° lower and is observed near $T_s\simeq 550$ °C (curve *4*, Fig. 2).

The concentration of the metallic phase (C_m) as given by the optical absorption data for 2223 films is around 7.5% at $T_s=450$ °C. As T_s increases to 500 °C, the concentration increases to 8.5%, then decreases to 7% at $T_s=600$ °C, before increasing rapidly with T_s to give a value higher than 30% at $T_s=700$ °C (curve *3* in Fig. 1). It can be seen from a comparison of curves *3* and *4* in Fig. 1 that the changes in C_m with T_s show reasonable agreement with the results of the x-ray structural analysis.

For 2212 films the dependence of C_m on T_s is more complex, mainly because of the wider range of existence of the crystalline state (curve *3*, Fig. 2). The agreement between the changes in C_m and C_{001} with T_s is also satisfactory. The x-ray structural analyses have shown that the minima of C_m and C_{001} observed at $T_s\simeq 450$ °C are attributable to disordering of the 2212 film structure accompanied by the formation of isolated families of 2223 phase plane in the bulk of the films.

The phase composition of the films is consistent with the composition of the 2223 and 2212 phases to within 3%. As long as the film structure is predominantly formed by (111) planes, the films are in the insulating state. Metallic conductivity appears if the bulk fraction of atomic groupings characterized by (001) planes exceeds 60%. In this case, the insulator–metal transition has a clearly defined percolation character.[10] The results agree with the theoretical predictions[14] whereby superlattices may be formed in high-temperature superconductors with complex lattices (Bi and Ti systems). The structure of the 2212 and 2223 crystalline phases combines elements of perovskite and cubic (such as NaCl) sublattices and the evolution of the perovskite structure involves the growth of layers of the homologous series $Sr_2Ca_{n-1}Cu_nO_{2n+1}$ (Ref. 2), which promotes the formation

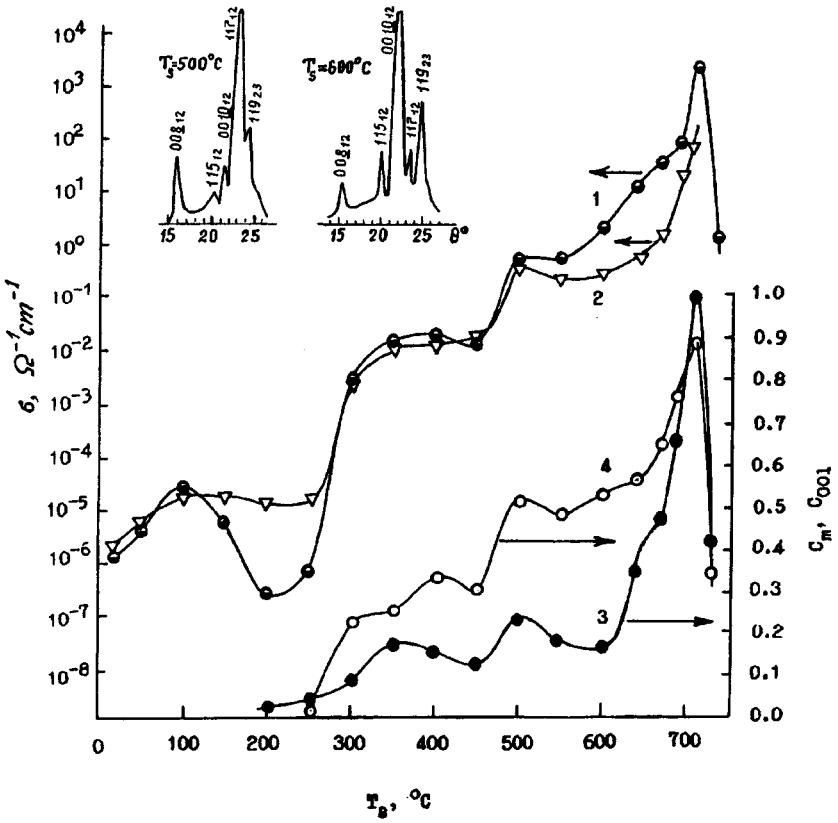

FIG. 2. Parameters of 2212 films versus growth temperature: *1*—electrical conductivity of films ($T=300$ K) on MgO substrates; *2*—electrical conductivity of films ($T=300$ K) on Al_2O_3 substrates; *3*—concentration of the metallic phase C_m in films on MgO from optical absorption data; *4*—concentration of material represented by 001 groups (C_{001}) in films on MgO from results of x-ray structural analyses. The inset shows x-ray diffraction patterns of films on MgO near the orientational phase transition.

of (111) planes. However, many elements of the homogeneous system incorporate a source of impairment of the initial order, with the formation of a heterogeneous structure[15] as soon as the external conditions (in our case, the increased diffusion mobility of the atoms with increasing temperature) begin to favor this. The transition of a multicomponent system from a homogeneous to a heterogeneous structure is a second-order phase transition with a reduction in the energy of the system[15] and is clearly caused by intensified interatomic interactions in the (001) planes. The establishment of heterogeneity is promoted by the inhomogeneity of the system and also by various physical parameters of the samples and conditions favoring the evolution of long-range interactions,[15] such as chains of indirect exchange interaction (Cu^{2+}–O^{2-}–Cu^{2+},....), $p-d$ exchange interactions, elastic anisotropic stresses at the film–substrate interface, and so on. (111)⇒(001) orientational phase transitions are observed, usually randomly, and are not generally taken into account[16–18] since high-temperature superconductors are synthesized at high temperatures when (001) reflections always predominate on the diffraction patterns.

Spatially isolated groupings with atomic ordering in the (111) planes, which precede the formation of the corresponding textured planes, are formed by insulating-phase inclusions in the superconducting matrix. In surface analyses of these results, these data may be incorrectly attributed to the formation of insulating phases for which the interplanar spacings are close to those for the 2212 or 2223 phases, or they may be attributed to a decrease in the carrier concentration (this is in fact the case but is not caused by a change in the oxygen concentration but by localization of electron states in (001) planes). In principle, crystallites represented by (111) crystallographic planes may, of course, also contain (001) planes. However, the disorder in the distribution of the atoms in these planes may be so great (this assumption is confirmed by the absence of any coherent reflections of appreciable intensity from these planes), that the Anderson localization criterion[19] is satisfied for the electron states and these crystallites may be in the insulating state regardless of the oxygen concentration.

The authors are grateful to V. M. Svistunov and B. Ya. Sukharevskiĭ for their interest in this work and for discussions of the results, and also to N. N. Pafomov, B. I. Perekrestov, T. A. D'yachenko, and E. I. Pushenko for assistance with the investigations.

[1] M. Yu. Kupriyanov and K. K. Likharev, Usp. Fiz. Nauk **160**(5), 49 (1990) [Sov. Phys. Usp. **33**, 340 (1990)].
[2] G. P. Shveĭkin, V. A. Gubanov, A. A. Fotiev, G. V. Bazuev, and A. A. Evdokimov, *Electronic Structure and Physical Properties of High-Temperature Superconductors* [in Russian], Nauka, Moscow (1990).
[3] V. D. Okunev, N. N. Pafomov, B. I. Perekrestov, and V. M. Svistunov, Pis'ma Zh. Tekh. Fiz. **20**(10), 60 (1994) [Tech. Phys. Lett. **20**, 414 (1994)].
[4] V. D. Okunev, Z. A. Samoĭlenko, E. I. Pushenko, Yu. F. Revenko, and B. I. Perekrestov, Neorg. Mater. **30**, 226 (1994).
[5] V. D. Okunev, Z. A. Samoĭlenko, N. N. Pafomov, and T. A. D'yachenko, Neorg. Mater. **32**, 855 (1996).
[6] V. D. Okunev, N. N. Pafomov, I. Iguchi, and V. M. Svistunov, Zh. Tekh. Fiz. **65**(12), 106 (1995) [Tech. Phys. **40**, 1260 (1995)].
[7] V. D. Okunev, N. N. Pafomov, Z. A. Samoĭlenko, and V. M. Svistunov, Pis'ma Zh. Tekh. Fiz. **19**(5), 39 (1993) [Tech. Phys. Lett. **19**, 147 (1993)].
[8] V. D. Okunev and T. A. D'yachenko, Fiz. Nizh. Temp. **22**, 1252 (1996) [Low Temp. Phys. **22**, 953 (1996)].
[9] V. D. Okunev, N. N. Pafomov, B. I. Perekrestov, and V. M. Svistunov,

Fiz. Nizh. Temp. **22**, 659 (1996) [Low Temp. Phys. **22**, 506 (1996)].
[10] V. D. Okunev, N. N. Pafomov, V. M. Svistunov, S. J. Lewandowski, P. Gierlowski, and W. Kula, Physica C **262**, 75 (1996).
[11] V. D. Okunev and T. A. D'yachenko, Fiz. Tverd. Tela (St. Petersburg) **35**, 3076 (1993) [Phys. Solid State **35**, 1514 (1993)].
[12] K. Hirochi, K. Setsune, S. Hayashi, K. Mizuno, T. Matsushima, Y. Ichikawa, H. Adachi, and K. Wasa, Physica B **165–166**, 1255 (1990).
[13] V. D. Okunev, N. N. Pafomov, Z. A. Samoilenko, A. T. Budnikov, Functional Mater. **3**(2), 139 (1996).
[14] V. A. Veryazov, Yu. É. Kitaev, V. P. Smirnov, and R. A. Évarestov, *High-Temperature Superconductivity*, Part 1 [in Russian], Mashinostroenie, Leningrad (1990), pp. 446–513.
[15] M. A. Krivoglaz, *Electronic Structure and Electronic Properties of Metals* [in Russian], Naukova Dumka, Kiev (1988), pp. 3–39.
[16] L. Ganapathi, J. Narayan, and A. Kumar, Appl. Phys. Lett. **55**, 1460 (1989).
[17] H. G. Lee, C. J. Kim, K. H. Lee, and D. Y. Won, Appl. Phys. Lett. **55**, 391 (1989).
[18] J. G. Noudem, J. Beille, D. Bourgault, A. Sulpice, and R. Tournier, Physica C **230**, 42 (1994).
[19] N. F. Mott, *Metal–Insulator Transitions* (Taylor and Francis, 1974; Mir, Moscow, 1979).

Translated by R. M. Durham

Effect of particle mass on the behavior of stochastic ratchets

A. P. Nikitin and D. É. Postnov

Saratov State University
(Submitted February 5, 1997)
Pis'ma Zh. Tekh. Fiz. **24**, 47–53 (January 26, 1998)

Nonlinear Brownian motion in stochastic rachets is investigated by electronic simulation methods. It is shown experimentally that it is possible to sort particles by mass using a discrete random process, binary noise, as the source of the nonequilibrium stochastic ratchets.
 [S1063-7850(98)02701-3]

The fundamental effects observed in stochastic ratchets[1–5] are not the only reason investigators are interested in them. Problems associated with the characteristics of Brownian motion in nonlinear potential fields play a growing role in molecular biology[1,4] and nanotechnology.[6] The term ''stochastic ratchets'' derives from the profile shape of an anisotropic (asymmetric) spatially periodic potential (Fig. 1a). Because of the asymmetry of the potential the probabilities of noise-induced transitions through the potential barriers can be different for opposite directions. This results in the appearance of a nonzero probability flux. A characteristic of stochastic ratchets is that nonequilibrium is produced in the system by noise and not by a constant external macroscopic force. The motion of a Brownian particle can be described by the equation

$$M\frac{d^2x}{dt^2}+\gamma\frac{dx}{dt}+\frac{\partial U(x,t)}{\partial x}+\xi(t)=0. \tag{1}$$

Here x is the spatial coordinate, $U(x,t)$ is the potential, M is the particle mass, γ is the viscosity, and $\xi(t)$ is white noise, where $\langle\xi(t)\rangle=0$, $\langle\xi(t)\xi(t+\tau)\rangle=2k_BT\gamma\delta(\tau)$, k_B is Boltzmann's constant, and T is the temperature. We write the potential $U(x,t)$ in Eq. (1) in the form

$$U(x,t)=V(x)+z(t)x, \tag{2}$$

where $V(x)$ is the anisotropic (asymmetric) periodic component of the potential, $V(x)=V(L+x)$, and L is the period of the potential. The typical form of $V(x)$ is shown in Fig. 1a. Here $z(t)$ is a random force with zero mean. If $z(t)=0$ holds, then according to the fluctuation-dissipation theorem Gaussian white noise $\xi(t)$ will be an equilibrium process for this system. This means that, irrespective of the profile shape of the potential barriers, the noise $\xi(t)$ cannot induce motion of the Brownian particles that is directed on the average. However, the introduction of external noise $z(t)$ can drive the system out of equilibrium and give rise to Brownian motion that is directed on the average. In addition, as shown in Refs. 2 and 7, the direction and magnitude of the particle flux induced by the noise $z(t)$ depends on the statistics of the noise $z(t)$.

In many cases problems of applied interest can be formulated in the approximation of small k_BT (high potential barriers $V(x)$). In the present Letter we study the effect of particle mass on particle transport in stochastic ratchets. We note that investigators ordinarily study the overdamped regime, where the friction γ is so large that the term containing the mass M in Eq. (1) is neglected. Moreover, this simplification decreases the order of the differential equation and makes it easier to solve.

As a rule, stochastic ratchets are investigated by numerical or approximate analytic methods.[2,3,7] An exact analytic solution can be obtained only in rare cases.[2] For this reason, in addition to numerical experiments, the possibility of electronic simulation of stochastic systems is of interest. We used a system of phase-controlled self-tuning of the frequency to construct an electronic analog of stochastic ratchets[8,9] and conducted a series of experiments for the purpose of determining the dependence of the average velocity of the Brownian motion on the inert mass of the particles.

The experimental results obtained with the electronic analog of stochastic ratchets are displayed in Fig. 2a. Here and below the results will be discussed in the language of particle motion. The experiment was conducted in the low-temperature approximation ($k_BT\to0$). Binary noise, a discrete random process with two equally probable states $-Z$ and $+Z$, was chosen for $z(t)$. In addition, a change in state is possible only at fixed times $t_k=\Delta\pm kT_0$, where $T_0=\text{const}$, $k=0, 1, 2, \ldots$ is a nonnegative integer, and Δ is a random quantity that does not depend on $z(t)$ and is distributed uniformly on the segment $[0,T_0]$. For this choice of the noise statistics $z(t)$, according to Eq. (2) the potential $U(x,t)$ will switch between two profiles, as shown in Figs. 1b and 1c. If the amplitude Z is very small, particle motion will occur only within a well, i.e., it will be confined within one period of the potential. When Z exceeds a threshold value Z_1, a particle will be able to move over a distance greater than L. This situation is illustrated in Figs. 1b and 1c. On account of the asymmetry of the potential $V(x)$ motion is possible only in one direction, rightward. The potential barrier blocks leftward motion. As Z increases, the slope of the profile $U(x,t)$ will increase and this will result in a higher average velocity $\langle\dot{x}\rangle$ of the particle motion. We note that an asymmetric potential $V(x)$ will behave as a rectifying element, converting the energy of the noise $z(t)$ into directed particle motion. Here energy conversion occurs by means of rectification of the random force $z(t)$: Particle motion toward the right occurs under the action of the random force $z(t)$ minus the relatively weak forces due to the potential $V(x)$; particle motion toward the left is impossible, since the forces due to the potential $V(x)$ compensate the random force $z(t)$.

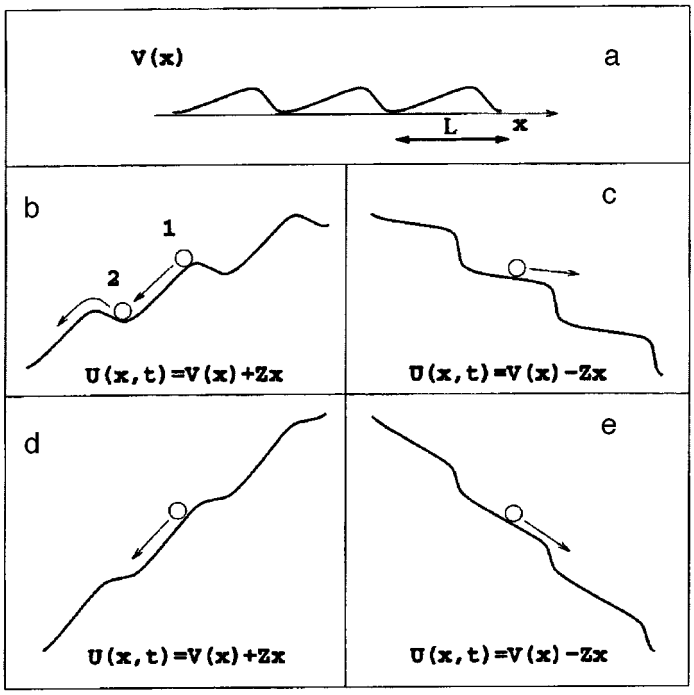

FIG. 1. a) Typical form of a ratchet potential, b) and c) $U(x,t)$ profile for $Z<\sup_x|dV(x)/dx|$, d) and e) $U(x,t)$ profile for $Z>\sup_x|dV(x)/dx|$.

If the amplitude Z of the noise $z(t)$ is very large, then $U(x,t)$ will switch between profiles with no local minima and maxima (Fig. 1d and 1e). This means that there are no potential barriers. Particle motion is possible both rightward and leftward. For very large amplitudes Z the forces due to the potential $V(x)$ are negligibly weak and both directions of motion for a particle become ''equally allowed.'' Then the average velocity of a particle approaches zero ($\langle\dot{x}\rangle\to 0$).

Let us now consider the situation illustrated in Fig. 1b. Let a particle be located near a local maximum of $U(x,t)$ (position 1 in Fig. 1b) some time after the noise $z(t)$ switches from the state $+Z$ into the state $-Z$ and rolls down to a local minimum of $U(x,t)$ (position 2 in Fig. 1b) with zero initial velocity. If the particle is sufficiently massive (heavy), it will obviously be able to continue its motion by inertia and overcome the potential barrier.

The M dependence of the noise amplitude Z^* for which leftward motion becomes possible is obvious: The larger M, the lower the value of Z^* required for a particle to overcome the potential barrier (Fig. 1b). In the case $M=0$ leftward motion is possible only if Z^* exceeds the value $z_2=\sup_x|dV(x)/dx|$. It is obvious that with increasing amplitude Z leftward motion becomes possible earlier for a heavier particle than for a light particle. A limit on the increase in the average velocity $\langle\dot{x}\rangle$ appears when the amplitude Z exceeds the value Z^* for which particle motion in both directions—leftward and rightward—becomes possible. Hence it follows that as the amplitude Z increases, the limit on the growth and the subsequent dropoff of $\langle\dot{x}\rangle$ appear earlier for heavier particles than for light particles (Fig. 2a).

The behavior indicated above can be used to sort particles by mass under the action of a random force. Figure 2b shows the experimental results obtained when the symmetry of the binary noise acting on the system was artificially broken by shifting the noise by a constant amount σ (in Eq. (2)

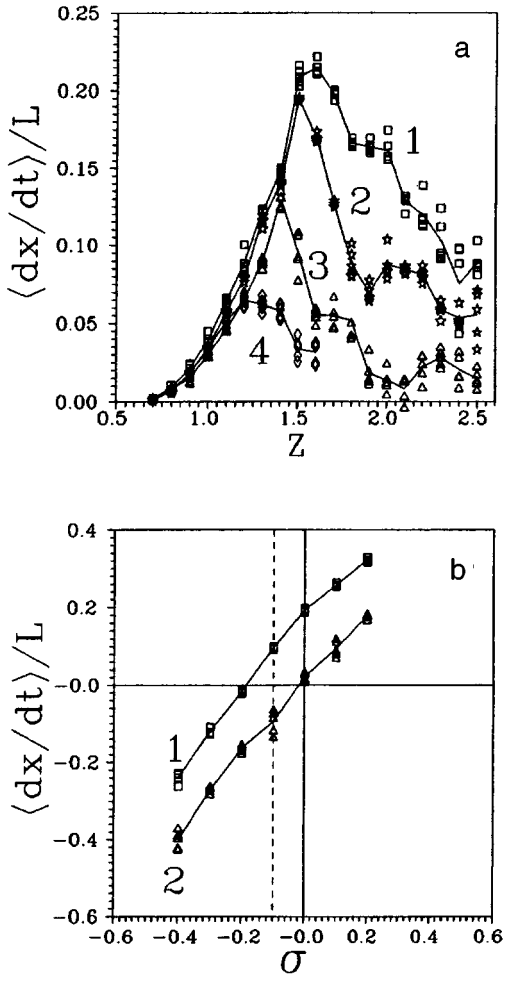

FIG. 2. a) Normalized average velocity $\langle\dot{x}\rangle/L$ versus amplitude Z of the noise $z(t)$. The curves 1–4 correspond to masses $M=0$, 0.022, 0.1, and 0.2, respectively. Remaining parameters: $(\max V(x)-\min V(x))/L=0.365$, $\gamma=1$, $T_0=0.138$. All parameters are given in dimensionless form. b) Normalized average velocity $\langle\dot{x}\rangle/L$ versus the constant shift σ. Curve 1 corresponds to mass $M=0$, curve 2 to $M=0.1$; $Z=1.6$.

$z(t)$ was replaced by $z(t)+\sigma$, where $\sigma=\text{const}$). This corresponds to introducing a small constant slope in the potential $V(x)$. As one can see from the plot, the sign of $\langle \dot{x} \rangle$ then depends on the mass of the particle! This means that particles with mass greater or less than some critical value will move left- or rightward, respectively.

It should be noted that by letting $k_B T \to 0$ we freed the particle from thermal fluctuations. Strictly speaking, such a particle is not Brownian, since there is no thermal motion. If $k_B T$ is assumed to be different from zero but sufficiently small, then, evidently, there will be no nonlinear interaction between the noises and the dependence of $\langle \dot{x} \rangle$ on M will be preserved. Effects due to the nonlinear interaction of the noises should be expected to appear for large values of $k_B T$. This is an important problem and requires further investigation.

We thank Professor Lutz Shimanskiĭ-Gaĭer at Humboldt University for his interest in the results of this work and for a fruitful discussion of the problem. This work was supported in part by the Russian State Committee of Institutions of Higher Learning on Natural Science (grant 95–0–8.3–66) and the Russian-German grant DFG and RFFI 436 RUS 113/334/0(R).

[1] M. Magnasco, Phys. Rev. Lett. **72**, 2656 (1994).
[2] C. R. Doering, W. Horsthemke, and J. Riordan, Phys. Rev. Lett. **72**, 2984 (1994).
[3] R. D. Astumian and M. Bier, Phys. Rev. Lett. **72**, 1766 (1994).
[4] J. Prost, J.-F. Chauwin, L. Peliti, and A. Ajdari, Phys. Rev. Lett. **72**, 2652 (1994).
[5] R. Bartussek, P. Hänggi, and J. G. Kissner, Europhys. Lett. **28**, 459 (1994).
[6] L. P. Faucheux, L. S. Bourdieu, P. D. Kaplan, and A. J. Libchaber, Phys. Rev. Lett. **74**, 1504 (1995).
[7] M. Bier, Phys. Lett. A **211**, 12 (1996).
[8] D. É. Postnov, A. P. Nikitin, and V. S. Anishchenko, Pis'ma Zh. Tekh. Fiz. **22**, 24 (1996) [Tech. Phys. Lett. **22**, 352 (1996)].
[9] A. P. Nikitin, D. E. Postnov, and V. S. Anishchenko, submitted to IEEE Trans. on Circuits and Systems I.

Translated by M. E. Alferieff
Edited by David L. Book

Simultaneous measurement of temperature and pressure

A. S. Kim

Perm' State University
(Submitted June 19, 1997)
Pis'ma Zh. Tekh. Fiz. **24**, 54–57 (January 26, 1998)

It is shown theoretically and experimentally that nuclear quadrupole resonance can be used to measure temperature and pressure simultaneously. [S1063-7850(98)02801-8]

The discovery of the temperature dependence[1] and pressure dependence[2] of the nuclear quadrupole resonance (NQR) frequency has made it possible to develop one-frequency methods for measuring temperature[3] and pressure[4] using NQR. In this method one parameter, the temperature or the pressure, is measured and the other is fixed.

This Letter examines theoretically and experimentally the possibility of measuring temperature and pressure simultaneously. A pulsed program of two-frequency excitation of spin-echo signals (see Fig. 1) is used to measure these parameters. The program makes it possible to detect signals from two excited transitions, for which the NQR frequencies depend on the temperature and pressure, of a multilevel spin system. The choice of a transition of a multilevel spin system used for measuring temperature or pressure is determined by the ratio of the temperature and pressure coefficients of the NQR frequency. To measure temperature the temperature coefficient of the NQR frequency must be large and the pressure coefficient small (compared with the temperature coefficient) on one of the excited transitions. To measure pressure the pressure coefficient of the NQR frequency must be large and the temperature coefficient small on the other excited transition.

The signal amplitudes were calculated by the density-matrix method, similarly to the method described in Refs. 5 and 6 . The expressions for the amplitudes of the responses on the two excited transitions of a multilevel spin system are as follows:

$$E_{m,m-1}=2(I'_x)_{m,m-1}\left\{-A(x,y)\omega_{m+1,m}\ \sin\ \omega_{m,m-1}\left\{t-\left[\left(1+\frac{\omega_{m+1,m}}{\omega_{m,m-1}}\right)\tau_1+\tau_2\right]\right\}\right\} \quad (1)$$

at the frequency $\omega_{m.m-1}$ and

$$E_{m+1,m}=2(I'_x)_{m+1,m}\{B(x,y)\omega_{m+1,m}\ \sin\ \omega_{m+1,m}\{t-2\tau_1\}\} \quad (2)$$

at the frequency $\omega_{m+1,m}$. Here $(I'_x)_{m,m-1}$ and $(I'_x)_{m+1,m}$ are elements of the operator I_x in the quadrupole Hamiltonian $\mathscr{H}_Q$ representation; the functions $A(x,y)$ and $B(x,y)$ are trigonometric functions of the angular durations of the acting pulses; $\omega_{m,m-1}$ and $\omega_{m+1,m}$ are the frequencies of the two excited transitions with a common energy level; τ_1 and τ_2 are the time intervals between the pulses; and m is the magnetic quantum number.

Signals at frequency $\omega_{m,m-1}$ are observed at the time

$$t=\left(1+\frac{\omega_{m+1,m}}{\omega_{m,m-1}}\right)\tau_1+\tau_2$$

and signals at the frequency $\omega_{m+1,m}$ are observed at the time

$$t=2\tau_1.$$

As one can see from Eqs. (1) and (2), the signal amplitudes are proportional to $\omega_{m+1,m}$, i.e., the carrier frequency of the first pulse.

The temperature and pressure indicator materials must satisfy the following general requirements.

1. The transverse and longitudinal relaxation times on the observed transitions must be long over wide temperature and pressure ranges to observe the echo signals.

2. The signal/noise ratio must be good over wide temperature and pressure ranges.

3. The frequency range of the resonant nuclei must be convenient.

4. The two excited lines must not overlap as the temperature and pressure are varied.

5. The equivalent Qs of the observed lines, $Q_{\text{eqv}}=\nu_i/\Delta\nu_i$, where ν_i is the resonance frequency of the observed transition and $\Delta\nu_i$ is the linewidth, must be large.

The experiment was performed on a two-frequency pulsed NQR spectrometer.[7] The sample consisted of polycrystalline $SbCl_3$ (resonance of ^{123}Sb nuclei, $J=7/2$). The temperature dependence of the NQR frequency on the transition 3/2–5/2 was used for temperature measurements and the pressure dependence of the NQR frequency for the transition 1/2–3/2 was used for pressure measurements. The temperature coefficient of the NQR frequency in the temperature range 77–300 K and pressure range 1–400 kg/cm^2 for the transition 3/2–5/2 equals -6.3 kHz/grad and the

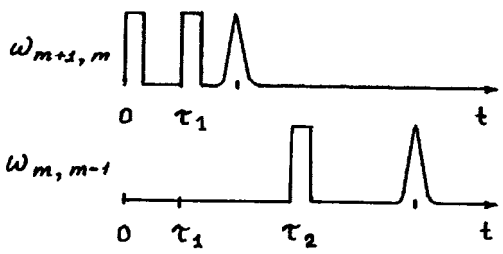

FIG. 1. Pulsed program of two-frequency excitation of echo signals used for simultaneous measurement of temperature and pressure.

 1063-7850/98/010064-02$15.00

pressure coefficient of the NQR frequency on the transition 1/2–3/2 equals 75 Hz/kg/cm^2. The NQR signal frequencies measured on these two transitions under standard conditions are $\nu_1 = 37.478$ MHz and $\nu_2 = 67.754$ MHz. They correspond to $T = 300$ K and $P = 1$ kg/cm^2. Other values of the temperature and pressure can be measured similarly.

In summary, the two-frequency pulsed NQR method makes it possible to measure pressure and temperature simultaneously. The accuracy of the measurements of these parameters depends on the excitation frequencies of the multilevel spin system, the temperature and pressure coefficients of the frequencies, the widths of the observed signals, and the conditions of excitation of the spin system.

[1] H. G. Dehmelt and H. Kruger, Z. Physik **129**, 401 (1951).
[2] T. Kushida, G. B. Benedek, and N. Bloembergen, Phys. Rev. **104**, 1364 (1956).
[3] J. Vanier, Metrologia **1**, 135 (1965).
[4] D. B. Balashov and D. A. Ikhenov, Fiz. Tverd. Tela (Leningrad) **16**, 1213 (1974) [Sov. Phys. Solid State **16**, 780 (1974)].
[5] N. E. Aĭnbinder and V. S. Grechishkin, Izv. Vyssh. Uchebn. Zaved. Radiofiz. **10**, 186 (1967).
[6] A. S. Kim, Radiospektrosk. (Perm'), No. 19, 153 (1989).
[7] A. S. Kim, Inventor's Certificate No. 1132207 (1984).

Translated by M. E. Alferieff
Edited by David L. Book

Determination of fluctuations of the electron temperature and density in an ionization-unstable inert-gas plasma in a magnetogasdynamic channel

T. A. Lapushkina, E. A. D'yakonova, and R. V. Vasil'eva

A. F. Ioffe Physicotechnical Institute
Russian Academy of Sciences, St. Petersburg
(Submitted June 16, 1997)
Pis'ma Zh. Tekh. Fiz. **24**, 58–62 (January 26, 1998)

Electron temperature and density fluctuations arising as a result of the development of ionization instability in nonequilibrium magnetogasdynamic channels, where a pure inert gas without alkali-metal seeding is used as the working gas, are studied in greater detail. An experiment was performed in a disk-shaped Hall-type magnetogasdynamic channel combined with a shock tube, with magnetic inductions greater than the inductance $B_c=0.57$ T at which ionization inhomogeneities first appear in the experiment. The electron temperature and density were measured from the drop in the intensity of the continuous radiation in the UV region according to the Unsöld–Kramers and Biberman–Norman theories. On the average, the electron temperature in inhomogeneities varies from 7000 to 10000 K and reaches its highest values in small-scale fluctuations. As a result of the absence of ionization equilibrium in the inhomogeneities, relatively small fluctuations of n_e and a phase shift between the fluctuations of n_e and T_e are observed. At the same time, the average values of the electron density increase with the degree of supercriticality of the magnetic field. This evidently results in a higher effective conductivity. [S1063-7850(98)02901-2]

In our previous work[1–6] it was found that the development of ionization instability in pure inert gases without alkali-metal seeding results in growth of the effective conductivity and extracted power. Our purpose in the present work is to study the characteristic features of ionization instability in greater depth and to determine the mechanisms responsible for the observed effects. Our main objective is to determine the magnitude of the electron temperature and density fluctuations and to establish the correlation between them.

The experiment was performed in a disk-shaped Hall magnetogasdynamic channel combined with a shock tube where a flow of an ionized gas was produced. The apparatus, the measurement method, and the method for calculating the parameters for a stable plasma are described in Refs. 1 and 2. Xenon was used as the working gas. The pressure in the low-pressure chamber was equal to 26 torr. The Mach number of the shock front in the shock tube was $M_I=6.9$. The values of the flow parameters in the disk-shaped magnetogasdynamic channel are presented in Refs. 4 and 5. The present experiment was performed with a load coefficient $K=0.7$. In the experiment, instability starts to develop in magnetic fields $B_c\geqslant 0.57$ T.

The measurement of n_e and T_e is based on recording the absolute and relative intensities of the continuous radiation. The general mechanisms of the continuous emission were established by Unsöld and Kramers.[7] Refinements due to the nonhydrogen-like nature of the complex atoms were taken into account in the Biberman–Norman theory.[8]

The energy distribution in the continuous spectrum of xenon was investigated in detail in Ref. 9. It was shown that windows are present in the dense sequence of Xe terms. As a result, in some spectral regions the intensity I_ν of the continuous radiation is frequency-dependent:

$$I_\nu=\begin{cases} 4.3\xi(\nu)\dfrac{2h}{c^2}\dfrac{N_eN_i}{(kT_e)^{1/2}}=A, & \nu\leqslant\nu_I \\ A\alpha\,\exp(-h\nu/kT_e), & \nu_I<\nu<\nu_{II} \\ A(1-\beta\,\exp(-h\nu/kT_e)), & \nu>\nu_{III} \end{cases}$$

$$\alpha=\exp(h\nu_I/kT_e),$$

$$\beta=\exp(h\nu_{II}/kT_e)-\exp(h\nu_I/kT_e),$$

$$\gamma=\exp(h\nu_I/kT_e)-\exp(h\nu_{II}/kT_e)+\exp(h\nu_{III}/kT_e);$$

$$\nu_I=3\times10^{14}\text{s}^{-1},\quad \nu_{II}=4.5\times10^{14}\text{s}^{-1},$$

$$\nu_{III}=6\times10^{14}\text{s}^{-1}.$$

In the Xe radiation spectrum in the frequency range $\nu>10^{14}$ s^{-1} there is a substantial wavelength interval (470–300 nm) where the radiation intensity drops off exponentially. In Ref. 9 it is shown that in this case the electron temperature can be determined using the relation

$$T=\frac{h}{k}\frac{\nu_2-\nu_1}{\ln(I_1/I_2)}$$

by comparing I_ν for two frequencies.

The experiment was organized as follows. A quartz window was inserted in plexiglass disks in the gas-dynamic channel at the radius $r=9$ cm. Rotating mirrors and quartz lenses directed radiation from the disk-shaped channel onto a diffraction grating. Two regions of the spectrum were extracted: $\lambda_1=423\pm1.5$ nm and $\lambda_2=313\pm1.5$ nm. The radiation was detected with photomultipliers. The signals from the photomultipliers were fed into a digital oscillograph and processed in a computer. A shock-compressed gas plug with the

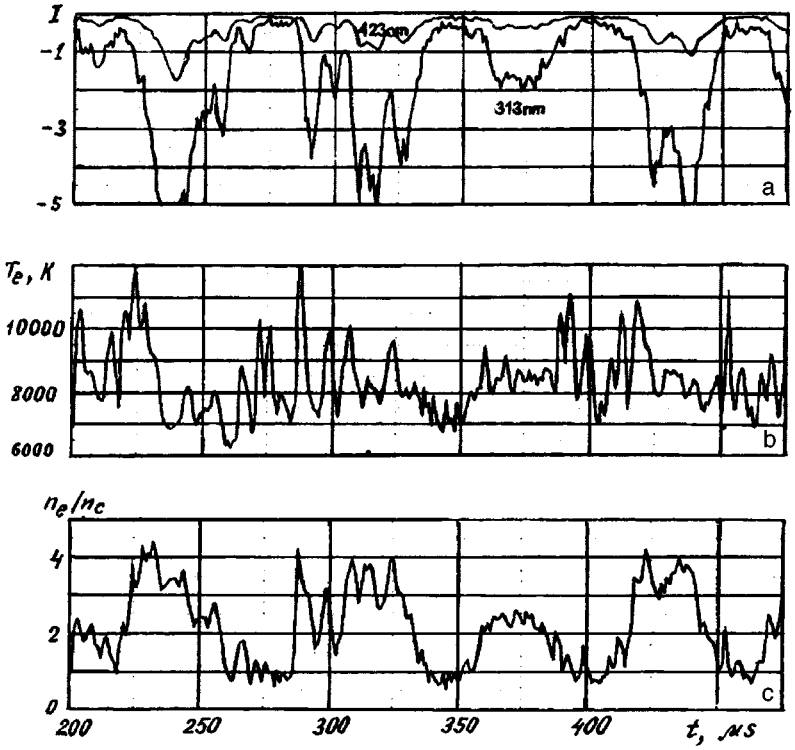

FIG. 1. a) Oscillogram of signals from photomultipliers detecting radiation in two spectral regions (the numbers on the curves are wavelengths); b) values of the temperature in the fluctuations; c) electron density fluctuations.

Mach number of the shock front $M_I = 10.5$ served as the standard for the radiation and electron temperature. In Ref. 10 it was shown that for $M \geqslant 10$ the measured parameters of the shock-compressed gas plug agree well with the computed values.

The absolute values of the temperature were determined to within approximately 10%. The relative temperature in the fluctuations was measured to within 5%. The absolute values of the electron density were determined to within 30% and the relative values to within 10%.

Analysis of the oscillograms of the radiation for different magnetic field strengths showed that fluctuations with a duration of 3 μs and shorter are due mainly to photomultiplier noise, while the lower-frequency fluctuations characterize the ionization-unstable plasma.

Figure 1 shows fragments of oscillograms from the photomultipliers. The fragments correspond to radiation from the center of the hot plug for a regime with developed ionization instability at $B = 1$ T. The figure also shows the electron temperature and density fluctuations. Relatively low-frequency oscillations with period 70–80 μs and higher-frequency oscillations with a period of about 10 μs can be distinguished in the oscillograms. This corresponds to the passage of large inhomogeneities, forming a background against which smaller formations can be distinguished, by the photomultipliers. The highest values of T_e occur in the small-scale fluctuations. On the average, the electron temperature in the inhomogeneities varies from 7000 to 10000 K. In the case of ionization equilibrium the electron density should vary approximately by a factor of 20, but the observed fluctuations of n_e are much smaller, indicating that the inhomogeneities are not in an ionization equilibrium. The fact that the relation between n_e and T_e is described not by the Saha formula but rather by the laws of kinetics explains in part the fact that a phase shift is observed between the fluctuations of n_e and T_e, though regions with high electron density correspond largely to regions with high temperature. It is obvious that in regions with high electron temperature there was enough time for the electron density to increase as the electrons moved along the channel, while in regions with a low temperature there was not enough time for the electron density to decrease much because the recombination mechanism is comparatively slow. The average electron density approximately doubles as the field increases from the critical value $B_c = 0.57$ T up to $B = 1.0$ T. Evidently, the increase of the effective conductivity of the plasma as the magnetic field becomes more supercritical, as observed in previous studies, explains why the average electron density increases with increasing supercriticality, despite the formation of inhomogeneities.

[1] R. V. Vasil'eva, A. L. Genkin, V. L. Goryachev *et al.*, A. F. Ioffe Physicotechnical Institute, Russian Academy of Sciences, St. Petersburg, 1991, p. 206.
[2] R. V. Vasil'eva, A. V. Erofeev, D. N. Mirshanov, and T. A. Alekseeva, Zh. Tekh. Fiz. **59**, 27 (1989) [Sov. Phys. Tech. Phys. **34**, 728 (1989)].
[3] R. V. Vasil'eva, A. V. Erofeev, A. D. Zuev *et al.*, Pis'ma Zh. Tekh. Fiz. **20**, 27 (1994) [Tech. Phys. Lett. **20**, 734 (1994)].
[4] A. V. Erofeev, R. V. Vasil'eva, A. D. Zuev *et al.*, in *Proceedings of the 12th Int. Conf. on MHD Electrical Power Generation*, Yokohama, Japan, 1996, p. 74–82.
[5] R. V. Vasil'eva, E. A. D'yakonova, A. V. Erofeev *et al.*, Zh. Tekh. Fiz. **67**(12), 6 (1997) [Tech. Phys. **42**, 1376 (1997)].
[6] T. A. Lapushkina, R. V. Vasil'eva, A. V. Erofeev, and A. D. Zuev, Zh. Tekh. Fiz. **67**, No. 12 (1997) [Tech. Phys. , (1997)].
[7] A. Unsöld, *Physik der Sternatomsphären*, Springer-Verlag, Berlin, 1955 [Russian translation, Inostr. lit., Moscow, 1949, p. 630].

[8] L. M. Biberman and G. É. Norman, Usp. Fiz. Nauk **91**, 193 (1967) [Sov. Phys. Usp. **10**, 52 (1967)].
[9] A. P. Dronov, A. G. Sviridov, and N. N. Sobolev, Opt. Spektrosk. **12**, 677 (1962) [Opt. Spectrosc. **12**, 383 (1962)].
[10] G. K. Tumakaev and V. R. Lazovskaya in *Aerophysical Investigations of Supersonic Flows* [in Russian], Nauka, Moscow, 1967, p. 304.

Translated by M. E. Alferieff
Edited by David L. Book

Thermionic emission galvanomagnetic effect

Kh. N. Vezirov

Scientific Research Institute of Photoelectronics, Baku
(Submitted May 16, 1997)
Pis'ma Zh. Tekh. Fiz. **24**, 63–67 (January 26, 1998)

Experiments are described which permit the existence of an appreciable thermionic emission current from a photocathode to be established and the dependence of the thermionic emission current density of the cathode on the temperature, magnetic field, and current passed through the photocathode to be measured. © *1998 American Institute of Physics.* [S1063-7850(98)03001-8]

As has already been reported, the combined effect of an electric current and a magnetic field on a photoemitter gives rise to the photoemission galvanomagnetic effect.[1]

Further investigations have led to the discovery of a second emission galvanomagnetic effect. In this effect, the thermionic emission current density of a photocathode carrying a current changes in response to a magnetic field.

This effect has not been observed in photoelectronic devices (PEDs) exhibiting a photoemission galvanomagnetic effect,[1] because in these devices the magnetic field was perpendicular to the photocathode plane.

Samples of special PEDs with a distinctive design were prepared for the experiments (Fig. 1). Without going into the technological details of the fabrication of such a sample, which are quite complicated, we note only that in this PED the substrate 1 for the photocathode (and therefore the photocathode itself) is not aligned perpendicular to the cylindrical shell *2* but rather is oriented at an angle ($\sim 70°$). A rectangular Ag–O–Cs cathode 3 approximately 150 nm thick, 3 cm wide, and 6 cm long was produced on the substrate 1.[2] Two opposite edges of the photocathode were positioned on two separate silver film contacts (packing), 4 and 5.[3] The two other edges of the photocathode were free of packing. The part of the photocathode located between the packing lay on a glass substrate *1*. The vacuum in the volume of the sample was equal to 10^{-6} Pa.

The sample was placed in a special powerful solenoid. The solenoid was also equipped with a special furnace, which was used to control the temperature of the photocathode (sample) in a range from room temperature and higher. The solenoid was constructed in a manner so that it could be used in different regimes, i.e., a magnetic field could be switched on both with and without the furnace and the furnace could switched on both with and without a magnetic field. When the solenoid was switched on, a magnetic field was generated with induction **B** oriented perpendicular to the current flowing through the photocathode film and simultaneously at an angle to the photocathode plane (i.e., **B** was oriented parallel to the axis 6 of the sample). The structural features of the sample are now obvious: 1) In the interior of the sample the magnetic induction arising in the solenoid is parallel to the electric field between the anode *7* and the photocathode, so this magnetic field does not disturb the motion of the electrons in the vacuum from the photocathode to the anode; 2) electrons drifting in the volume of the photocathode are deflected by the magnetic field in a direction perpendicular to the longitudinal axis *6* of the sample, since the magnetic induction is perpendicular to the current flowing through the photocathode; and 3) since it is directed at an angle to the plane of the photocathode, the magnetic field causes electrons to accumulate not at the edge of the photocathode[1] but rather on its entire area (surface).

The measurements were performed as follows. Voltage was applied from the power supply *8* to the packing *4* and *5* (Fig. 1) without passing current through the solenoid and its furnace and a current, measured by the meter *9*, was passed through the photocathode. Simultaneously, a forward potential difference in the saturation range of the emission current (from tens of volts and higher) was produced between the anode *7* and the photocathode by the power supply 10, and the thermionic emission current was measured with the meters *11* or *12*. The thermionic emission current did not depend on the strength of the current passed through the photocathode, i.e., the voltage on the packing. Also, we note that on account of the good thermal conductivity of the substrate the Joule heat from the current flowing through the photocathode produced virtually no heating of the photocathode (the temperature increased by a fraction of a degree). Next, a current was passed through the furnace, the temperature of the photocathode increased and the thermionic emission current of the photocathode was remeasured. The measurements of the latter current at different temperatures allowed a curve of the thermionic emission current density of the photocathode versus temperature to be constructed (Fig. 2, straight line *1*).

Next, a current was passed through the solenoid. This produced in the sample a magnetic field parallel to the axis *6* of the sample. The measurements described above were performed in the magnetic field by the same method. Measurements performed in different magnetic fields with different strengths of the current through the photocathode made it possible to construct a series of curves of the thermionic emission current density of the photocathode versus temperature, magnetic field, and current through the photocathode (Fig. 2).

It was observed that the thermionic emission current density of a photocathode carrying a current changes in response to the magnetic field. The changes were proportional to the strength of the current through the photocathode and to the magnetic induction (Fig. 2).

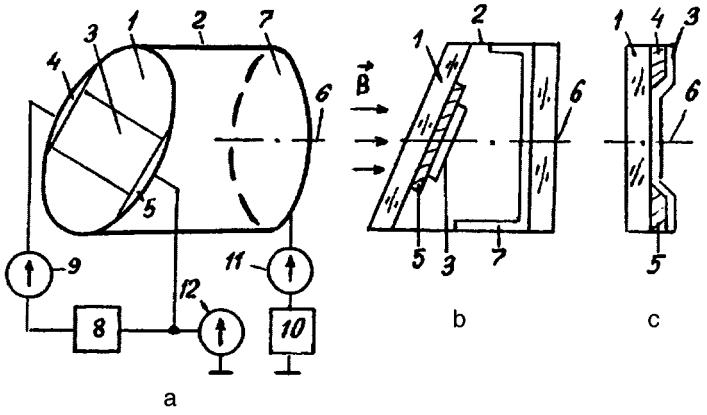

FIG. 1. Design of the sample: a) Overall view and connection scheme, b) longitudinal section along the axis, c) substrate of the sample.

The effect exhibited odd parity, i.e., when the direction of the current through the photocathode or the magnetic field was reversed (by changing the direction of the current in the solenoid winding), the effect likewise changed sign, specifically, instead of decreasing (Fig. 2, straight lines *2* and *3*) the thermionic emission current density increased (straight lines *4* and *5*), though it did not increase to the same degree that it decreased.

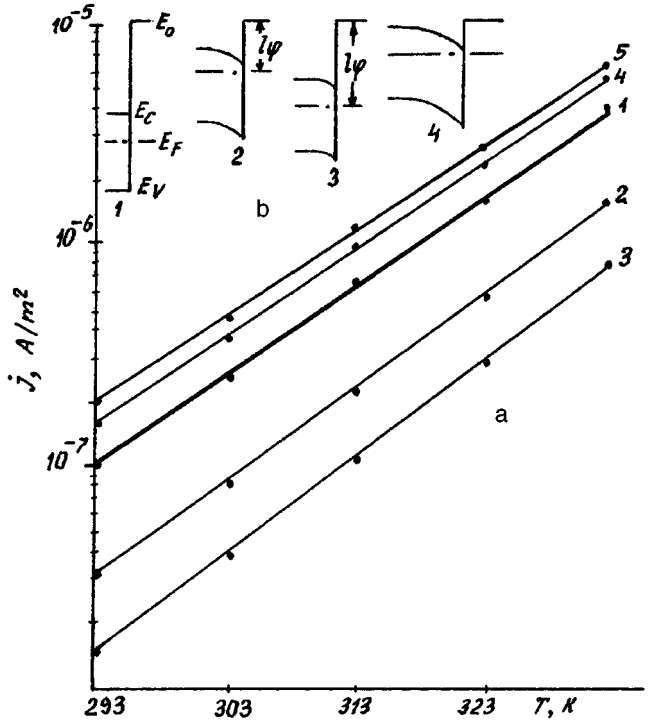

FIG. 2. a) Thermionic emission current density j versus the current passed through the photocathode, the magnetic field, and the temperature: *1* — Initial, no magnetic field, currents from 0 to 10 mA; *2* — magnetic field 500 Oe, current 3 mA (both by convention in the forward direction); *3* — magnetic field 1000 Oe, current 10 mA (both in the forward direction); *4* — magnetic field 500 Oe (opposite direction), current 3 mA (forward direction), *5* — magnetic field 1000 Oe (forward direction), current 10 mA (reverse direction). b) Qualitative band diagram of the photocathode: *1* — photocathode without a film of an electropositive material on the surface bordering on the vacuum; *2* — photocathode with an optimal cesium oxide film on the surface (corresponds to the straight line *1*); *3* — photocathode with an excess of electrons on the surface bordering the vacuum (corresponds to the straight lines *2* and *3*); *4* — photocathode in the case of outflow of electrons from the surface bordering on the vacuum (corresponds to the straight lines *4* and *5*).

As is well known,[1] when the surface of an Ag–O–Cs photocathode is coated with a cesium oxide film, a dipole layer with a mobile charge appears on the surface bordering on the vacuum (Fig. 2b). The reason why Ag–O–Cs photocathodes have the lowest work function $e\varphi$ of all known materials and therefore the highest thermionic emission current density is that the composition and structure of the surface layer of Ag–O–Cs photocathodes is optimal.[3,4]

It is thought that when a current flows through the film of the photocathode, as a result of the deflection of the electrons by the magnetic field, negative charge will accumulate on the photocathode surface next to the vacuum (compare with Ref. 1). This is analogous to the appearance of a field that retards the thermionic electrons. For this reason, the energy levels in the volume of the photocathode must sink below their levels at the surface and below the vacuum level (Fig. 2b). The work function $e\varphi$ in this case increases and the thermionic emision current density decreases (Fig. 2a, straight lines *2* and *3*).

Conversely, for a current or magnetic field with the opposite orientation, on account of the outflow of electrons the potential of the photocathode surface increases, the work function $e\varphi$ decreases, and the thermionic emission current density increases (straight lines *4* and *5* in Fig. 2a).

The effect observed could be helpful in the investigation of the vaccuum emission properties of films.

[1] Kh. N. Vesirov, É. Yu. Salaev, and D. Sh. Abdinov, Zh. Tekh. Fiz. **66**, 203 (1996) [Tech. Phys. **41**, 1197 (1996)].
[2] A. H. Sommer, *Photoemissive Materials: Preparation, Properties , and Uses*, Wiley, N. Y., 1968 [Russian translation, Énergiya, Moscow, 1973].
[3] W. Hartmann and F. Bernhard, *Photomultipliers* [Russian translation, Gosénergoizdat, Moscow, 1961.
[4] V. S. Fomenko, *Reference Data on the Emission Properties of Materials* [in Russian], Nauk. Dumka, Kiev, 1981; transl. of earlier edition *Handbook of Thermionic Properties*, Consultants Bureau, New York, 1966.

Translated by M. E. Alferieff
Edited by David L. Book

Diffusion of erbium in silicon

S. Zaĭnabidinov, D. É. Nazirov, A. Zh. Akbarov, A. A. Iminov, and T. M. Toshtemirov

Tashkent State University
(Submitted December 16, 1996)
Pis'ma Zh. Tekh. Fiz. **24**, 68–71 (January 26, 1998)

Diffusion of erbium in silicon has been investigated by the electric method. The erbium diffusion coefficient in the temperature range 1150–1250 °C increases from 1.4×10^{-13} to 6.2×10^{-13} $cm^2\cdot s^{-1}$. The values obtained for the diffusion coefficient of erbium in silicon are in good agreement with data obtained by the method of tagged atoms. © *1998 American Institute of Physics.* [S1063-7850(98)03101-2]

A problem of current concern in the physics of semiconductor materials science and instrument engineering is increasing the heat and radiation resistance of silicon. This has led to interest in doping silicon with rare-earth elements.[1–4] In this connection, the diffusion of rare-earth elements in silicon merits investigation. However, few such investigations have been performed and the results obtained by different authors are ambiguous or else doubtful.

Prior to the present investigation, the diffusion of erbium in silicon, as noted in Ref. 3, was investigated in Ref. 5, where an indirect method, the electrical conduction method, was employed. The activation energy found there $\Delta E=4.96$ eV is undoubtedly questionable, since it is virtually identical to or even somewhat higher than the activation energy of self-diffusion of silicon.[6] In this connection, in Ref. 7 erbium diffusion in silicon was investigated in detail by a direct method, the method of radioactive isotopes.

This Letter reports the results of an investigation of the diffusion of erbium in silicon by successive removal of thin layers and measurement of the resistivity by a four-probe method.

The diffusion source was produced by depositing erbium chloride on samples of *n*-type silicon ($\rho=15$ Ω cm, area ~1.5 cm^2, thickness ~350 μm). Diffusion annealing was conducted in air in the temperature interval 1150–1250 °C for 5–24 h. After diffusion annealing the samples were washed in HF, boiled in aqua regia ($3HCl:HNO_3$) for 10 min, and washed in distilled water. The resistivity profile was determined by the method of sectioning: etching off thin layers (in a solution $1HF:4OHNO_3$ with washing in $3HCl:1HNO_3$) and measuring the resistivity of the sample by the four-probe method. The thickness of the removed layers (0.1–0.5 μm) was determined by weighing the sample. Measurements performed at several points on the surface showed a uniform impurity distribution over the section of the sample.

We determined the diffusion coefficient of erbium in silicon under the assumption that Fick's law holds and that the surface density of the impurity does not change in time (diffusion from a constant source into a semi-infinite body) and using the fact that the profile of electrically active charge carriers is identical to that of the residual quantity of the diffusant, since the resistivity of the sample is a function of the diffusant density ($\rho=f(n)$, where $n=f[Q(x)]$). Here $Q(x)$ is the residual amount of the diffusant and n is the density of the electrically active charge carriers. To find the diffusion coefficient $\mathcal{D}$ the experimental curve of the residual

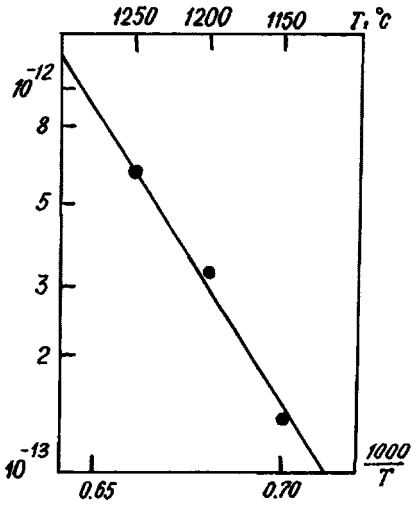

FIG. 1. Temperature dependence of the diffusion coefficient of erbium in silicon.

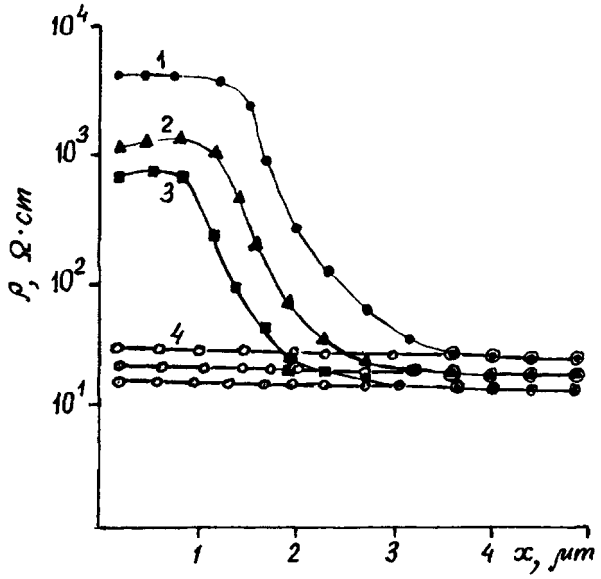

FIG. 2. Resistivity profile of doped and control samples: *1* — Si⟨Er⟩ 1250 °C — 5 h, *2* — Si⟨Er⟩ 1200 °C — 5 h, *3* — Si⟨Er⟩ 1150 °C — 8 h, *4* — control samples.

resistivity was compared with the theoretical curve for diffusion from a constant source.[8]

As the results obtained show, the residual resistivity curves can be described by the function *iezfc*, corresponding to the solution of Fick's equations for diffusion from a constant source. Figure 1 shows the temperature dependence of the diffusion coefficient of erbium in silicon. As follows from the data obtained, the diffusion coefficient of erbium in silicon calculated from the curves increases from $\sim 10^{-13}$ to 6×10^{-13} $\mathrm{cm}^2\cdot\mathrm{s}^{-1}$. The temperature dependence of the diffusion coefficient is described satisfactorily by an Arrhenius relation

$$\mathcal{D}=5\times 10^{-3}\ \exp\left[-\frac{3\ \mathrm{eV}}{KT}\right]\mathrm{cm}^2\cdot\mathrm{s}^{-1}(1150-1250\ ^\circ\mathrm{C}).$$

Note that the penetration depth of erbium in silicon, determined by the quantity $2\sqrt{\mathcal{D}t}$, is at most a few microns over the entire experimental interval. It was also found, using a thermoprobe, that after diffusion annealing erbium on the surface of *n*-type silicon manifests *p*-type conductivity.

Together with doped samples, we employed *n*-type control samples to determine the diffusion parameters. The results obtained with the control samples show that the resistivity profile of the control samples is a straight line and the resistivity profile of the doped samples has a high-resistivity part near the surface. This confirms that erbium is the diffusant (Fig. 2).

Our values of the erbium diffusion coefficient agree well with the data of Ref. 7. Since, as we determined, erbium is an acceptor in silicon, our values of the diffusion coefficients and activation energy of erbium attest to the fact that in silicon this impurity, just as praseodymium,[8] scandium,[9] and thulium,[7] like other group-III elements,[6] diffuses over the lattice sites.

[1] J. Mandelkorn, L. Schwartz, J. Broder, H. Kautz, and R. Ulman, J. Appl. Phys. **35**, 2258 (1964).
[2] N. T. Bagraev, L. S. Vlasenko, V. M. Volle, V. B. Voronkov, I. V. Grekhov, V. V. Dobrovenskiĭ, and A. I. Shagun, Zh. Tekh. Fiz. **54**, 917 (1984) [Sov. Phys. Tech. Phys. **29**, 547 (1984)].
[3] D. É. Nazyrov, A. R. Regel', and G. S. Kulikov, Preprint No. 1122, A. F. Ioffe Physicotechnical Institute, Soviet Academy of Sciences, Leningrad, 1987.
[4] R. Sh. Malkovich and D. É. Nazyrov, Pis'ma Zh. Tekh. Fiz. **15**, 38 (1988) [Sov. Tech. Phys. Lett. **15**, 136 (1988)].
[5] V. V. Ageev, N. S. Aksenov, and V. N. Kokovina, Izv. LÉTI, 80 (1977).
[6] W. Frank, U. Gosele, H. Mehrer, and A. Seeger, in *Diffusion in Crystalline Solids*, edited by G. E. Murch and A. S. Nowick, N. Y., 1984, p. 76.
[7] D. É Nazyrov, G. S. Kulikov, and R. Sh. Malkovich, Fiz. Tekh. Poluprovodn. **25**, 1653 (1991) [Sov. Phys. Semicond. **25**, 997 (1991)].
[8] D. É. Nazyrov, V. P. Usacheva, G. S. Kulikov, and R. Sh. Malkovich, Pis'ma Zh. Tekh. Fiz. **14**, 1102 (1988) [Sov. Tech. Phys. Lett. **14**, 483 (1988)].
[9] G. K. Azimov, S. Z. Zaĭnabidinov, and D. É. Nazyrov, Fiz. Tekh. Poluprovodn. **23**, 556 (1989) [Sov. Phys. Semicond. **23**, 347 (1989)].

Translated by M. E. Alferieff
Edited by David L. Book

2.35 μm LEDs for measuring methane

A. A. Popov, V. V. Sherstnev, and Yu. P. Yakovlev

A. F. Ioffe Physicotechnical Institute Russian Academy of Sciences, St. Petersburg
(Submitted June 30, 1997)
Pis'ma Zh. Tekh. Fiz. **24**, 72–79 (January 26, 1998)

GaAlAsSb/GaInAsSb/GaAlAsSb double-heterostructure LEDs emitting in the region of the 2.35 μm absorption band of methane have been developed for fast gas analyzers. Different designs of double heterostructures based on the solid solution GaInAsSb were studied. Continuous-wave optical power of 1.2 mW was achieved. The methane absorption spectrum for the LED radiation is presented. [S1063-7850(98)03201-7]

The range of wavelengths near 2.35 μm is characterized by the presence of many vibrational–rotational C–H absorption bands of hydrocarbons[1] and is promising for spectroscopic applications, specifically, for ecological and technological monitoring of the environment.[2] Attractive semiconductor emitters for this spectral region are light-emitting diodes based on multicomponent GaInAsSb solid solutions.[3,4] The development of LEDs based on GaInAsSb solid solutions has been reported previously for a wide spectral range 1.7–2.4 μm; the external quantum yield for LEDs with $\lambda = 2.3-2.4$ μm was equal to $\sim 1.2\%$.[4] A distinguishing feature of the electroluminescence of such structures was the competition between the interband volume and interface recombination in the region of the type-II heterojunction n-GaSb/n-GaInAsSb, determining the spectral power density of the semiconductor emitter. It was shown that the optimal ratio between the radiative and nonradiative recombination channels obtains when the conduction band separation at the type-II heterojunction dis less than 200 meV.[5]

The present study is a continuation of our work on infrared emitting heterostructures based on GaInAsSb. It is devoted to LEDs that do not contain a type-II GaSb/GaInAsSb heterojunction and are intended for spectroscopic detection of hydrocarbons in the wavelength range near 2.3 μm.

The LEDs consisted of a GaAlAsSb/GaInAsSb/GaAlAsSb symmetric double heterostructure grown by liquid-phase epitaxy (LPE) on a GaSb (100) substrate. The epitaxy technology for the heterostructures was reported previously in Ref. 6. The structures consisted of four epitaxial layers: an active GaInAsSb layer was sandwiched between two N- and P-GaAlAsSb wide-gap emitters (2.5 μm thick); a narrow-gap heavily doped GaSb layer (0.5 μm thick) was grown for the purpose of producing a low-resistance contact. All layers were lattice-matched with the GaSb substrate. The active GaInAsSb layer was characterized by an indium content of 0.21 ($E_g = 0.53$ eV). The wide-gap GaAlAsSb confining layers were doped with Te and Ge to density $(2-4)\cdot 10^{18}$ cm^{-3} and $(6-8)\cdot 10^{18}$ cm^{-3} for N- and P-type layers, respectively. The active GaInAsSb layer was doped with Te to electron density $(1-2)\cdot 10^{17}$ cm^{-3}. The LED heterostructures were investigated as a function of the active layer thickness in the interval from 0.5 to 1.6 μm. It was found that the maximum radiative recombination efficiency occurs for active layer thicknesses of order 0.6 μm. We note that the optimal thickness was much less than the carrier diffusion length (~ 2 μm). When the thickness was increased or decreased, the output power dropped.

Three types of LED heterostructures were grown and investigated: type I — $p-P-n-N-n$, type II — $n-N-n-P-p$, and type III — $n-N-n-P-p$. Epitaxial structures of the first two types were grown with Al content 0.50 ($E_g = 1.1$ eV) and differed from one another by the type of doping. The type-I heterostructure was grown on a p-type substrate doped with Ge to hole density $p \sim (7-9)\cdot 10^{18}$ cm^{-3}. The type-II structure was produced on a n-type substrate with $n \sim (1-3)\cdot 10^{17}$ cm^{-3}. The type-III heterostructure was similar to the type-II structure, but the Al content in the emitter regions was decreased to 34% ($E_g = 1.0$ eV). Note that in all three types of LEDs the active region was doped with Te to carrier density $n \sim (1-2)\cdot 10^{17}$ cm^{-3}. The energy band diagrams and schematics of the three types of heterostructures produced are presented in Fig. 1. This made it possible to obtain and investigate heterostructures without a type-II heterojunction of the type GaSb/GaInAsSb and differing by the characteristics of the emitter regions.

Round mesa diodes, prepared by photolithography and deep chemical etching into the substrate, were investigated. The total size of a single LED crystal was 500×500 μm. The emitting surface area $S \sim 7\cdot 10^{-4}$ cm^2 was determined by the mesa diameter (300 μm). The semiconductor crystal was mounted on a standard TO-18 case. A parabolic reflector was mounted on the case at the same time, making it possible to collimate the LED radiation in a solid angle of 10–12°. The total dimensions of the LED with the parabolic reflector were 9 mm in diameter and 5.5 mm in length.

The investigations were performed on an apparatus assembled in a synchronous detection scheme on the basis of a MDR-2 monochromator and GaInAsSb photodiode. The output radiation was collected in an IMO-2M optical power meter.

The current–voltage characteristics (IVCs) of the LEDs were of a diode character. The IVCs of the heterostructures differed from one another by the cutoff voltage, equal to 0.26 V for type-I, 0.70 V for type-II, and 0.57 V for type-III structures. For all forward-biased structures the series resistances $\sim 5-6$ Ω, and the type-I and -III IVCs had two sections with an inflection point near 6 mA. For low biases the IVCs can be described by the formula $I = I_0 \exp(eU/\beta kT)$, where e is the electron charge, T is the temperature, I_0 is the saturation current, equal to 0.05, 0.012, and 0.18 μA for the

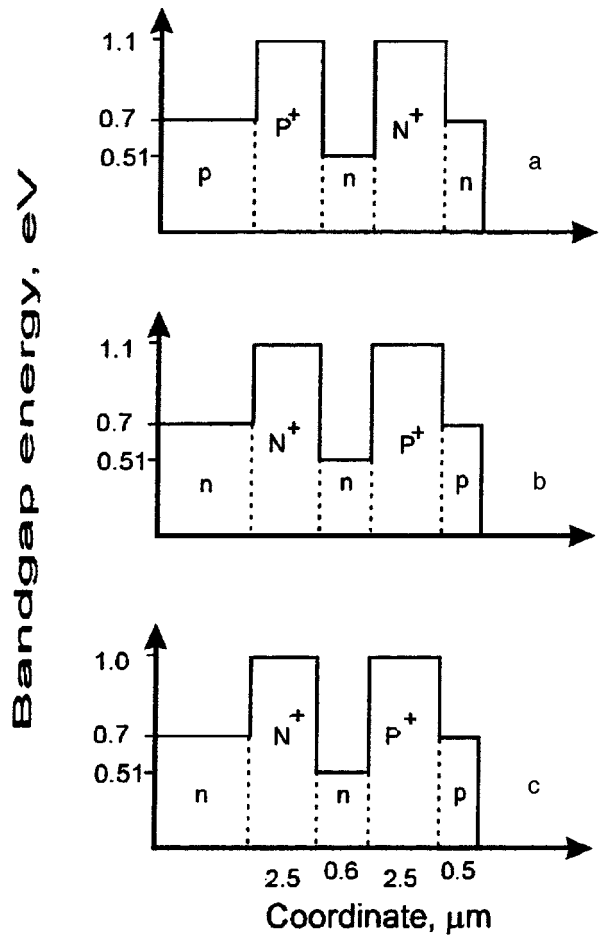

FIG. 1. Energy band diagrams of LED heterostructures: type-I — $p-P-n-N-n$ (a), type-II — $n-N-n-P-p$ (b), type-III — $n-N-n-P-p$ (c). The type-I and -II structures (a and b) contain 0.50% Al in the emitter layers and differ from one another by the type of doping. The type-III heterostructure (c) contains 34% Al in the emitter layers.

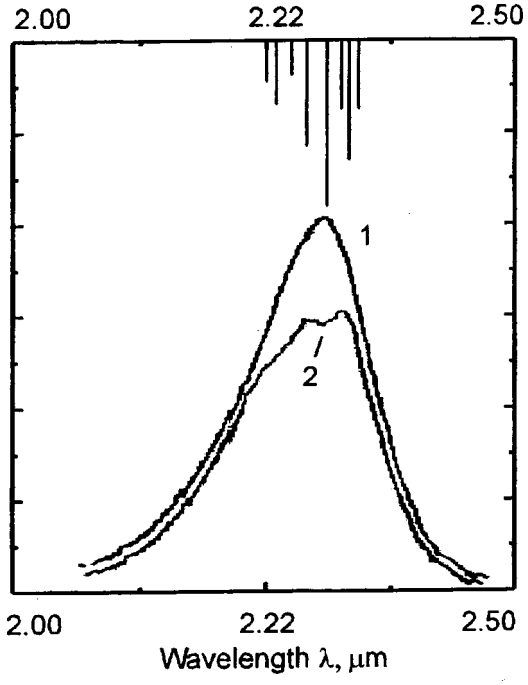

FIG. 2. V22718 LED emission spectrum (curve 1) recorded at room temperature ($T=300$ K) in a continuous-wave powering regime. The injection current was equal to 50 mA DC. The FWHM of the emission spectrum is equal to 0.22 μm. Curve 2 is the methane absorption spectrum recorded under the same conditions at atmospheric pressure for the LED radiation. The cell was 2.5 cm long. For comparison, the position and relative intensity of the methane absorption lines constructed on the basis of the HITRAN92 database[1] are presented at the top of the figure.

type-I, -II, and -III structures, respectively, and the coefficient $\beta=1.4-1.5$.

The spectral and power characteristics of the diodes were tested in the continuous-wave (CW) regime at room temperature. The radiation was observed under forward bias with the current amplitude above 2 mA. A rapid power increase was observed up to injection currents of 20 mA.

For all structures the spontaneous-emission spectrum consisted of a single emission band with the typical profile for infrared LEDs (Fig. 2). At 50 mA the maxima of the type-I, -II, and -III spectra were observed at wavelengths $\lambda=2.327$, 2.332, and 2.305 μm, respectively. The corresponding widths of the spectra (FWHM) were equal to 0.27, 0.22, and 0.25 μm. The LED radiation absorption spectrum (Fig. 2) of a methane-filled cell at atmospheric pressure confirms that the LEDs investigated are promising for detection of hydrocarbons by absorption spectroscopy at room temperature. After cooling to liquid-nitrogen temperature ($T=77$ K) the maxima shifted in the short-wavelength direction to $\lambda=2.1$ μm for the the type-I and -II structures and 2.06 μm for the type-III structure. The FWHM of the emission spectrum decreased to 0.085–0.095 μm for all LEDs. We note the following observed features of the spontaneous recombination spectra. The position of maximum emission was virtually independent of the magnitude of the injected current and a shift at an average rate of 0.05 nm/m in the long-wavelength direction was observed. The total temperature shift of the maximum was equal to 54–55 meV. All values were 8–15 meV smaller than the computed temperature broadening ΔE_g of the band gap. The emission spectrum was characterized by large broadening at both room temperature (45–60 meV FWHM) and liquid-nitrogen temperature (24–27 meV FWHM).

The current dependences of the output optical power are presented in Fig. 3. The optical power P increased up to currents of the order of $I=120$ mA and contained three sections with different exponents. Up to 40 mA the dependence was characterized by superlinear growth. In the current range up to 120 mA the slope decreased and above 120 mA the characteristic saturated. On cooling to liquid-nitrogen temperature the output power increased by a factor ranging from 8 (for type-I structure) up to 25 (for type-II structure). However, the curve constructed for type-II structures was characterized by a high output power over the entire range of currents. The maximum continuous power of 1.2 mW was achieved with an injection current of 120 mA for type-II structures. The external quantum yield at a current of 50 mA was equal to 2.25 and 1.7% for type-I, -II, and -III structures, respectively.

The characteristics presented showed that the spectral and electrical properties of GaInAsSb/GaAlAsSb double heterostructures agree for total recombination in the interior of

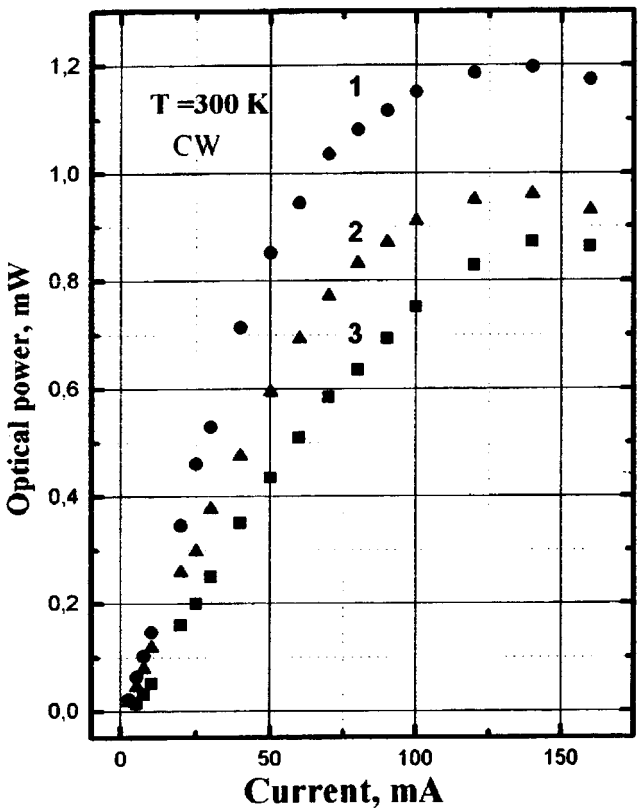

FIG. 3. Power characteristics of the LEDs. The dependences were obtained with a dc feed current at room temperature. 1 — Type-I , 2 — type-II, and 3 — type-III structures.

the active region. The measurements revealed how the spectral and power characteristics depend on the parameters of the emitter layers. The introduction of the additional emitter GaAlAsSb allowed an increase in the quantum yield of radiation from 1.25% (asymmetric heterostructure with a type-II interface[4]) to 1.75% (type-III structure). A further increase of the height of the heterobarriers (type-I and -II structures) increased the efficiency of the radiative recombination channel up to 2–2.5%. However, for all structures, the change of the superlinear current dependence of optical power ($n>1$) to a sublinear dependence ($n<1$) indicated a substantial increase in nonradiative losses with increasing injection current. The decrease in the radiative recombination efficiency should be attributed above all to the overheating of the active region with increasing continuous injection current[7] on account of both the increased thermal resistance of heat outflow into the substrate through the four-component solid solution and an increase in the injection of hot carriers. In addition, heavy doping of emitters and a high interfacial height intensify the tunneling leakage currents, but they decrease the forward-current density in the emitters. For type-I structures the weak temperature dependence and the low power of the radiation indicated the presence of tunneling carrier leakage, most likely occurring at the N/n heteroboundary with an active region. Nonetheless, the GaAlAsSb/GaInAsSb/GaAlAsSb type-II symmetric semiconductor heterostructure is best for achieving maximum spectral power density at low feed currents. Most important for producing infrared LEDs adapted from the standpoint of practical spectroscopic applications is the presence of large conduction band offsets, whose magnitude exceeds the band gap of the active region.

In summary, in the present Letter we report the development of LEDs for detection of C–H hydrocarbons at wavelengths near 2.3 μm. The investigations showed the advantage of a symmetric LED heterostructure constructed without a type-II GaSb/GaInAsSb heterojunction, since radiation from them is characterized by high spectral power density in the entire region of continuous pump currents. For room temperature, a maximum continuous-wave optical power of 1.2 mW ($3.7\cdot 10^{-13}$ W/m^{2}srHz) was achieved at wavelengths near 2.3 μm. It was shown that the LEDs are promising for detection of hydrocarbon molecules by the methods of absorption spectroscopy using the LEDs investigated.

[1] L. S. Rothman, R. R. Gamache, R. H. Tipping, C. P. Rinsland, M. A. Smith, D. Cris Benner, V. Malathy-Devi, J.-M. Flaud, C. Camy-Peyret, A. Goldman, S. T. Massie, L. R. Brown, R. A. Toth, J. Quant. Spectrosc. Radiat. Transf. **48**, 469 (1992).
[2] A. Mabbit and A. Parker, Sens. Rev. **16,** 38 (1996).
[3] A. A. Andaspaeva, A. N. Baranov, A. A. Guseĭnov, A. N. Imenkov, N. M. Kolchanova, and Yu. P. Yakovlev, Fiz. Tekh. Poluprovodn. **24**, 1708 (1990) [Sov. Phys. Semicond. **24**, 1067 (1990)].
[4] A. A. Andaspaeva, A. N. Baranov, A. A. Guseĭnov, A. N. Imenkov, N. M. Kolchanova, E. A. Sidorenkova, and Yu. P. Yakovlev, Pis'ma Zh. Tekh. Fiz. **15**, 71 (1989) [Sov. Tech. Phys. Lett. **15**, 734 (1989)].
[5] A. A. Andaspaeva, A. N. Imenkov, N. M. Kolchanova, A. A. Popov, and Yu. P. Yakovlev, Pis'ma Zh. Tekh. Fiz. **19**, 5 (1993) [Tech. Phys. Lett. **19**, 776 (1993)].
[6] A. M. Grebenyuk, A. M. Litvak, A. A. Popov, S. V. Syavris, and N. A. Charykov, J. Appl. Chem. (GB) **64**, Pt. 1, 2421 (1991).
[7] N. M. Kolchanova, A. A. Popov, A. B. Bogoslovskaya, and G. A. Sukach, Pis'ma Zh. Tekh. Fiz. **19**, 61 (1993) [Tech. Phys. Lett. **19**, 690 (1993)].

Translated by M. E. Alferieff
Edited by David L. Book

Instability of periodic stationary waves in an active nonlinear medium with high-frequency losses

A. A. Koronovskiĭ and I. S. Rempen

Educational–Scientific Center ''Kolledzh'', N. G. Chernyshevskiĭ Saratov State University
(Submitted May 29, 1997)
Pis'ma Zh. Tekh. Fiz. **24**, 80–87 (January 26, 1998)

The stability of stationary waves in nondispersive nonlinear active media with high-frequency losses is studied. It is shown that waves with wavelength greater than some minimum value $\lambda_{\min}$ can exist in such a medium. All stationary waves are unstable with respect to small perturbations of their profile, but as the wavelength increases, the lifetime of the wave increases and for waves with long wavelengths λ the lifetime can be long enough that these waves can in some sense be regarded as stable.
[S1063-7850(98)03301-1]

It has long been known that stationary waves (i.e., waves whose profile does not change with time) can exist in nonlinear active media. Moreover, the stationary solutions of the corresponding nonlinear partial differential equations are probably the simplest solutions to obtain, since the time-independence of the solutions makes it is possible to switch (for one-dimensional problems) from partial differential equations to ordinary differential equations (see, for example, Refs. 1–4).

At the same time, one of the most important questions concerning stationary waves, their stability, cannot be solved on the basis of a stationary solution. Indeed, cases when the initial differential equations admit stationary solutions but the solutions can be unstable with respect to small disturbances, and therefore stationary waves will not exist in real systems, are entirely possible. Thus, additional investigation is required in order to draw a conclusion about the stability (or instability) of stationary waves.[5,6]

In the present Letter one of the simplest nondispersive nonlinear active media with high-frequency losses is studied. A long transmission line, illustrated in Fig. 1, can serve as a model of such a medium. If it is assumed that the nonlinearity in the line is weak, then the equation describing the processes occurring in such a medium in a one-wave approximation[7] will have the form[8]

$$\frac{\partial u}{\partial t}+V_0\frac{\partial u}{\partial x}-\nu\frac{\partial^2 u}{\partial x^2}=\mu f(u), \tag{1}$$

where u is the dimensionless voltage, t is the dimensionless time, V_0 is the propagation velocity of waves in a linear lossless medium, ν is a high-frequency dissipation parameter, μ is the nonlinearity parameter, and $f(u)$ is the nonlinearity function (a dimensionless characteristic of the active nonlinear element), which must limit the growth of the oscillations and which, as a rule, is chosen in the form $f(u)=(1-u^2)u$. Introducing the new variables $\xi=(x-V_0t)\sqrt{\mu/\nu}$, $\tau=\mu t$, and assuming $u=u(\xi,\tau)$, we go over from Eq. (1) to the equation

$$\frac{\partial u}{\partial \tau}-\frac{\partial^2 u}{\partial \xi^2}=\mu f(u). \tag{2}$$

It is known that Eq. (1) admits a solution in the form of periodic stationary traveling waves propagating with velocity $V=V_0$.[8] However, the question of whether such periodic stationary waves are stable remains open. An answer to this question can be obtained, for example, by solving Eq. (2) numerically with the appropriate boundary and initial conditions:

$$u(0,\tau)=u(D,\tau),\quad u_\xi(0,\tau)=u_\xi(D,\tau),\quad u(\xi,0)=\varphi(\xi), \tag{3}$$

where D is the dimensionless wavelength and $\varphi(\xi)$ is the initial distribution. Actually, we study instead the dynamics of a system that closes on itself in a ring and is described by Eq. (2) with wavelength D.[9]

There exists, however, another method that can be used to determine the character of the stability of periodic stationary waves. Let us replace the function $f(u)=(1-u^2)u$ by the piecewise-linear function $f(u)=-u+|u+\frac{1}{2}|-|u-\frac{1}{2}|$. Of course, in this case the nonlinear medium with high-frequency losses will be a somewhat different from the one described above but, on the face of it, there should be no large sharp differences in this case. The piecewise linear form of the function $f(u)$ makes it possible, in turn, to make use of the circumstance that the system becomes linear on the corresponding segments, which can be helpful in analyzing the processes occurring in it (see, for example, Ref. 10).

The profile of a stationary wave propagating in a medium described by Eq. (2) with the boundary and initial conditions (3) will be determined as

$$u^0(\xi)=\begin{cases}\frac{1}{2}\left(\cot\frac{L}{2}\sin\xi-\cos\xi\right), & \xi\leqslant L,\\ \frac{1}{2}\left(2+\tanh\frac{S}{2}\sinh(\xi-L)-\cosh(\xi-L)\right), & L<\xi\leqslant L+S,\\ \frac{1}{2}\left(\cos(\xi-L-S)-\cot\frac{L}{2}\sin(\xi-L-S)\right), & L+S<\xi\leqslant 2L+S,\\ \frac{1}{2}\left(\cosh(\xi-2L-S)-\tanh\frac{S}{2}\sinh(\xi-2L-S)-2\right), & 2L+S<\xi\leqslant 2L+S,\end{cases} \tag{4}$$

where L and S are related by the relations[1)]

$$\cot\frac{L}{2}=\tanh\frac{S}{2} \tag{5}$$

and

$$2(L+S)=D. \tag{6}$$

One can see from Eqs. (4) and (5) that stationary waves with wavelength $\lambda\geqslant 2\pi$ can exist in the medium described by Eq. (2). (Correspondingly, in a medium described by Eq. (1) the minimum wavelength of a stationary wave will be $\lambda_{\min}=2\pi\sqrt{\nu/\mu}$ with $S=0$, when $|u(x,t)\leqslant 1/2|$ for any x.) It is easy to see that L decreases monotonically from π as S increases from 0.

It can be shown that stationary waves in our system are unstable: If $|u(\xi,\tau)|<1/2$ holds for any ξ, then there exists an analytic expression describing the evolution of the system:

$$u(\xi,\tau)=a_0\exp(\tau)+\sum_{n=1}^{\infty}a_n\cos\left(\frac{2\pi n}{D}\xi\right)\times\exp\left(\left(1-\frac{4\pi^2n^2}{D^2}\right)\tau\right)+\sum_{n=1}^{\infty}b_n\sin\left(\frac{2\pi n}{D}\xi\right)\times\exp\left(\left(1-\frac{4\pi^2n^2}{D^2}\right)\tau\right), \tag{7}$$

where the coefficients a_n and b_n are determined by the initial distribution $\varphi(\xi)$. It is obvious from the solution (7) obtained above that all such waves are unstable as a result of the existing components a_0 and a_k, b_k, $0<k<n$. On the other hand, for waves whose profile contains characteristic points $\xi^i_{1/2}(\tau)$ where $u(\xi^i_{1/2}(\tau),\tau)=\pm 1/2$ the question of the stability of these waves reduces to the question of the stability of these characteristic points. It can be shown that for such points

$$\frac{d}{d\tau}(\Delta\xi^i_{1/2}(\tau))\approx\Delta\xi^i_{1/2}(\tau), \tag{8}$$

where $\delta\xi^i_{1/2}(\tau)=\xi^i_{1/2}(\tau)-\xi^i_{1/2}$ is the displacement of the characteristic point $\xi^i_{1/2}(\tau)$ relative to the characteristic point $\xi^i_{1/2}$ of the stationary wave at time τ. It is obvious that the deviation will grow and therefore such stationary waves also are unstable.

We note that local disturbances of a stationary wave grow in time for sections of the wave profile where $|u(\xi,\tau)|<1/2$. At the same time, it is easy to see that local disturbances decay for sections of the wave profile where $|u(\xi,\tau)|>1/2$. Thus, the rate of growth of disturbances in the profile of a stationary wave will be determined by the ratio of the lengths of the ''stable'' and ''unstable'' sections of the wave profile. Since on the basis of the relations (5) and (6) the ratio S/L of the lengths of the stable and unstable sections increases with no limit as the wavelength λ of a stationary wave increases, the profile of a stationary wave can be expected to collapse all the more slowly the longer the wavelength of the wave. For a quantitative description of this circumstance, we introduce the quantity τ_l, which we shall call the ''lifetime'' of a stationary wave. The lifetime of a stationary wave of wavelength λ is to be understood as the time interval over which a specific disturbance of the profile of a stationary wave

$$\delta(\tau)=\frac{1}{\lambda}\int_{\xi^*}^{\xi^*+\lambda}|u(\xi,\tau)-u^0(\xi)|d\xi \tag{9}$$

doubles in size, i.e., $\delta(\tau_l)=2\delta(0)$, as $\delta(0)\to 0$ and $u(\xi,\tau)-u^0(\xi)=\text{const}$. It is obvious that the lifetime τ_l of a stationary wave increases with the wavelength of the wave, and theoretically the lifetime can be long enough so that, to within a prescribed accuracy, the profile of the stationary wave remains for a finite time interval. In this sense, stationary waves with long wavelengths λ can be regarded as stable.

Numerical simulation results[2)] confirm the conclusions obtained on the basis of an analysis of Eq. (2) with a piecewise-linear function $f(u)$. Waves that are close in terms of the profile of the stationary waves can exist for some time in a ring of length greater than 2π. Figure 2 displays curves

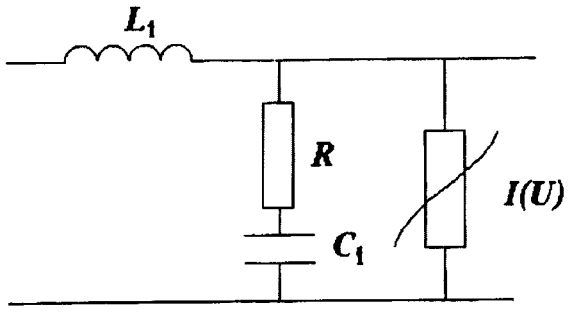

FIG. 1. Long transmission line: model of a nondispersive nonlinear active medium.

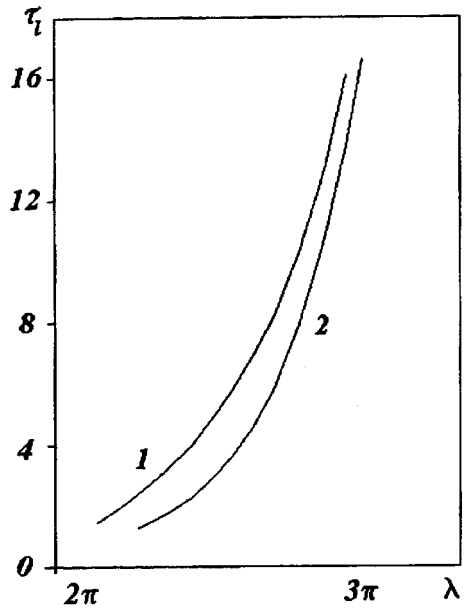

FIG. 2. Lifetime τ_l of a stationary wave versus the wavelength λ of the wave: *1* — Medium with a piecewise-linear function $f(u)$, *2* — medium with a cubic function $f(u)$.

of the lifetime of stationary waves, calculated from Eq. (9), versus the wavelength λ of the waves for the profile (4) with piecewise-linear and cubic functions $f(u)$. The curves presented clearly show that in both cases the lifetime of the waves increases with no limit as the wavelength increases, so that in some sense waves with large λ are stable. Since the lifetime increases with wavelength, a transition from stationary waves with short wavelengths to waves with long wavelengths occurs, as shown in Figs. 3 and 4, in a ring where several waves with different wavelengths λ can exist.

In closing, I wish to express my deep appreciation to Professor D. I. Trubetskov, Corresponding Member of the Russian Academy of Sciences, for his unfailing kindness and assistance and also to V. G. Anfinogentov, Candidate of Physicomathematical Sciences, and to postgraduate student A. E. Khramov for a number of valuable suggestions and critical remarks.

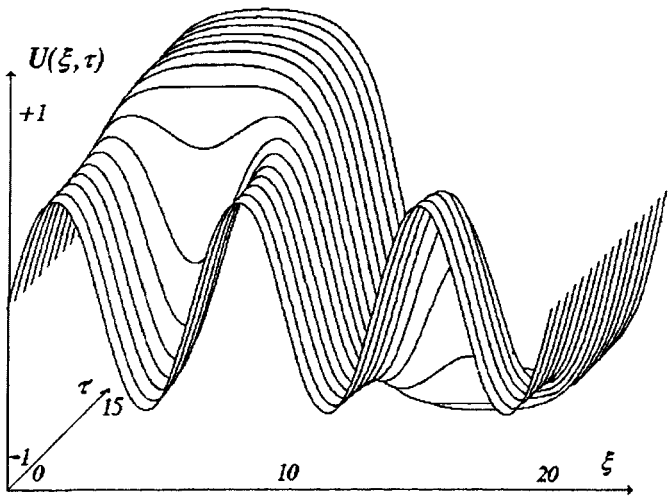

FIG. 3. Collapse of a stationary wave with wavelength $D/3$ and establishment of a stationary wave with wavelength D and longer lifetime τ_l in a medium with a piecewise-linear function $f(u)$.

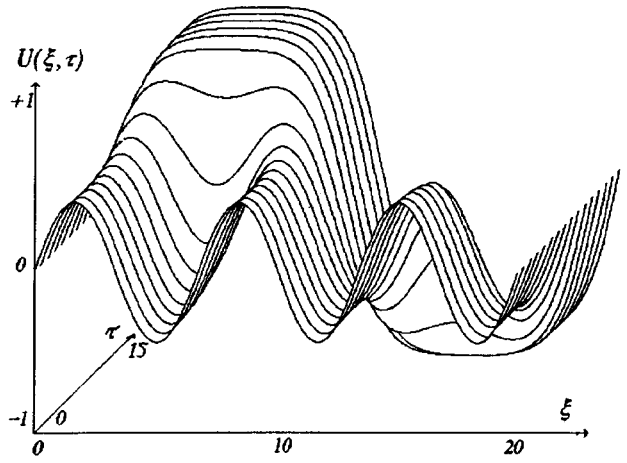

FIG. 4. Collapse of a stationary wave with wavelength $D/3$ and establishment of a stationary wave with wavelength D in a medium with a cubic function $f(u)$.

[1)]More accurately, $2(L+S)=D/n$, where $n=1, 2, \ldots, n_{\max}$, such that $D/n \geqslant 2\pi$, should be used instead of Eq. (6). However, we shall study only the cases where exactly one wavelength of a stationary wave fits within the ring. It is obvious that the case where several wavelengths fit within the ring can be reduced to the preceding case by decreasing the length of the ring by the appropriate factor.

[2)]Direct numerical simulation of Eq. (2) with the boundary and initial conditions (3) was performed for the functions $f(u)=-u+|u+\frac{1}{2}|-|u-\frac{1}{2}|$ and $f(u)=(1-u^2)u$. A six-point classical Crank–Nicholson scheme[11] with weight $w=1/2$ was chosen as the difference scheme. The system of nonlinear equations was solved by a hybrid method: The exterior iterations were performed using the Seidel method and the interior iterations were performed by Newton's method.[12] The coordinate step $h_\xi=0.01$ and time step $h_\tau=0.0025$ were chosen as the parameters of the scheme.

[1] M. I. Rabinovich, Izv. Vyssh. Uchebn. Zaved. Radiofiz. **17**, 477 (1974).
[2] L. A. Ostrovskiĭ, *Nonlinear Waves: Dynamics and Evolution* [in Russian], Nauka, Moscow, 1989, p. 29–50.
[3] Yu. I. Neĭmark and P. S. Landa, *Stochastic and Chaotic Oscillations*, Kluwer, Dordrecht, 1992 [Russian original, Nauka, Moscow, 1987].
[4] A. C. Scott, Trans. IRE CT-9, 192 (1962).
[5] A. Scott, *Active and Nonlinear Wave Propagation in Electronics*, Wiley, N. Y., 1970 [Russian translation, Sov. Radio, Moscow, 1977].
[6] W. Eckhaus, *Studies in Nonlinear Stability Theory*, Springer, New York, 1965.
[7] G. B. Whitham, *Linear and Nonlinear Waves*, Wiley, N. Y., 1974 [Russian translation, Mir, Moscow, 1977].
[8] M. I. Rabinovich and D. I. Trubetskov, *Introduction to the Theory of Oscillations and Waves* [in Russian], Nauka, Moscow, 1984.
[9] M. Kholodniok, A. Klich, M. Kubichek, and M. Marek, *Methods for Analysis of Nonlinear Dynamical Models* [in Russian], Mir, Moscow, 1991.
[10] R. J. Buratti and A. G. Lindgren, Proc. IEEE **56**, 1392 (1968).
[11] P. J. Roache, *Computational and Fluid Dynamics*, Hermosa Publishers, Albuquerque, N. M., 1976 [Russian translation, Mir, Moscow, 1980].
[12] A. A. Samarskiĭ and A. V. Gulin, *Numerical Methods* [in Russian], Nauka, Moscow, 1989.

Translated by M. E. Alferieff
Edited by David L. Book

Production of high-current electron beams in an explosive-emission diode at gas pressures $\sim 10^{-2}$–10^{-1} torr

É. N. Abdullin, G. P. Bazhenov, E. F. Balbonenko, and S. É. Kunts

Institute of High-Current Electronics, Siberian Branch of the Russian Academy of Sciences, Tomsk; Institute of Electrophysics, Ural Branch of the Russian Academy of Sciences, Ekaterinburg

(Submitted April 18, 1997)
Pis'ma Zh. Tekh. Fiz. **24**, 88–92 (January 26, 1998)

Data on production of electron beams with ~200 keV electrons and above ~100 A beam current in a diode with an explosive-emission cathode at background gas pressures $\sim 10^{-2}$–10^{-1} torr are presented. Discharge regimes with high-voltage stage duration up to 500–800 ns at 10^{-2} torr and 80 ns at 10^{-1} torr have been obtained. The duration of the electron beam behind a 50 μm thick titanium foil was equal to 200 and 400 ns, respectively, and was limited by the transmittance of the foil. © *1998 American Institute of Physics.* [S1063-7850(98)03401-6]

The production of high-current electron beams with background gas pressures $p \sim 10^{-2}$–10^{-1} torr is of interest in connection with efforts to expand the working pressure range of vacuum diodes and with the possibilities for substantial simplification of the vacuum system and the design of the electron accelerator.

Electron beams obtained in this pressure range have a relatively short current pulse duration $\sim 10^{-8}$ s as a rule.[1] The beam duration is limited because of breakdown of the diode, which causes a low-voltage arc discharge to be struck in the interelectrode gap. Breakdowns are attributed to the appearance of plasma in the interelectrode gas as a result of ionization of the background gas by the electron beam and to ignition of a gas discharge in the vacuum chamber of the accelerator.[2–4] The limitation of the duration of electron beams restricts their use and complicates the design of the pulse generator.

In the present Letter we report the results of an investigation of the possibility of protracting the high-voltage stage of a discharge in an explosive-emission diode at background gas pressures $p \sim 10^{-2}$–10^{-1} torr and thereby increasing the duration of the electron beams generated. It is obvious that the appearance of a plasma in the interelectrode gap does not signify that an arc discharge is struck and beam generation ceases. Estimates show that the conductivity of the interelectrode gap does not increase much after plasma appears. As a result, there is a possibility that the voltage on the diode can be kept at a level much higher than the arc-burning voltage, thereby blocking the transition of the discharge to the arc stage. Our plan was to increase the duration of the high-voltage stage of the discharge and correspondingly the duration of the generated electron beams by using electrodes consisting of materials characterized by a low plasma production rate and adopting measures to decrease the dropoff rate of the voltage on the interelectrode gap (limiting the emission surface area, decreasing current losses, and ensuring that the the power supply has adequate power and capacity).[5,6]

The experiments were performed using two Arkad'ev–Marx generators with output voltage of up to 300 kV, capacitance $C = 17$ nF and 330 pF per pulse, and characteristic impedance of the discharge circuit $\rho = 20$ and 140 Ω, respectively. Cathodes with a flat emitting surface area $S_e = 0.2$ and 9.6 cm^2, made of carbotekstim, brass coated with a lead solder, and tungsten were used. Ceramic tubes were used to protect the nonemitting sections of the cathode and cathode holder from ignition of a gas discharge and to decrease current leakage. Graphite and duraluminum were used for the anode. The interelectrode gap width d varied from 8 to 170 mm. The electron energy spectrum of the diode was judged from measurements of the fraction of the electronic current reaching the collector in vacuum through a window in the anode with cross section $S_w = 350$ cm^2, geometric transmittance $k = 100\%$, and a 50 μm thick titanium foil cover. In a number of experiments a window with $S_w = 64$ cm^2 and $k = 38\%$ was used; in this case the electron beam was extracted into the atmosphere.

Figure 1a shows oscillograms of the voltage U on the diode, the current I_c of the electron-beam collector, the current I_w reaching the $S_w = 350$ cm^2 window, which were all obtained by applying a pulse from a a $C = 17$ nF generator at pressure $p = 10^{-2}$ torr. One can see that the duration τ of the high-voltage stage of the discharge is much longer than 10^{-7} s, and electron beam generation continues even as the current in the diode increases. The maximum duration of the high-voltage stage is 500–800 ns at $p = 10^{-2}$ torr and ~80 ns at $p = 10^{-1}$ torr (Fig. 1b). At pressures $p \sim 10^{-2}$ torr and higher τ is virtually independent of the interelectrode gap width, the emission surface area of the cathode, and the electrode material. Conditioning of the discharge gap occurs: The duration of the high-voltage stage increases by 10–20% after ~50–100 pulses from the $C = 17$ nF generator are applied to the diode. Switching on a $C = 330$ pF generator in the repetitive-pulse mode with frequency 240 Hz approximately doubles τ.

It was established that electron-beam generation in the diode occurs in the entire pressure range from 5×10^{-5} up to 5×10^{-1} torr. The duration of the current pulse I_c of the beam at the collector reached 200 ns at pressure $p = 10^{-2}$ torr, 40 ns at $p = 10^{-1}$ torr, and 20 ns at $p = 5 \times 10^{-1}$ torr. The collector current is observed to cut off at a voltage ~130–140 kV across the cathode–anode gap, when electrons can no longer pass through the foil.

Figure 2 shows the values of the ratio of the collector

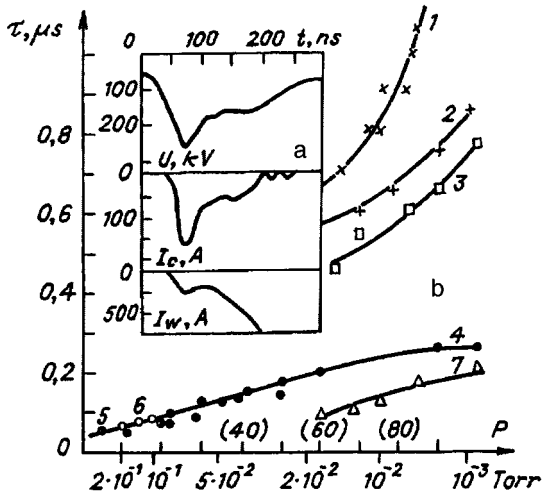

FIG. 1. Oscillograms of U, I_c, and I_w with $S_e=0.2$ cm^2 and $d=125$ mm (a) and curves (b) of the duration τ of the high-voltage stage versus pressure p (the values in parentheses correspond to the scale divisions of a thermocouple vacuum meter); $C=17$ nF (*1–3*) and 330 pF in the repetitive-pulse (*4–6*) and single-pulse (*7*) regimes; $S_e=9.6$ cm^2 (*3*) and 0.2 cm^2 in all other cases; $d=170$ (*1*, *5*, *6*) 15 (*4*), 12 (*2*, *7*) and 8 (*3*) mm; cathode material: brass (*1*, *5*), carbotekstim (*2–4*, *7*), and tungsten (*6*).

current I_c to the current kI_w at the foil of the $S_w=350$ cm^2 (*1*) and 65 cm^2 (*2*) windows calculated from oscillograms recorded at different background-gas pressures. Oscillograms obtained at pressures $p=5\times10^{-5}-10^{-2}$ torr were used in the case of the $S_w=350$ cm^2 window and $p=5\times10^{-5}-3\times10^{-2}$ torr in the case of the other window. To estimate the changes occurring in the energy spectrum during the pulse in the case of the $S_w=350$ cm^2 window, the values of the ratio I_c/kI_w were calculated at different times during collector current, and in the case of the $S_w=-350$ cm^2 window they were calculated only for the instant corresponding to maximum voltage on the diode. One can see that in both cases the fraction of the beam current passing through the foil onto the collector is determined only by the voltage on the diode. Changes in the background-gas pressure as well as the current flow time have no effect on the fraction of the beam current reaching the collector. It can therefore be assumed that the electronic current at the high-voltage stage of the discharge with gas pressure increasing at least up to $p=3\times10^{-2}$ torr, just as in a vacuum diode with $p\sim10^{-4}-10^{-5}$ torr, is transported by a beam of electrons with energy corresponding to the voltage applied to the diode. The values obtained for I_c/kI_w (*1*) agree well with the theoretical curve (*3*) of the transmission coefficient of the foil in terms of the number of particles.[7] The observed deviations of I_c/kI_w from the theoretical values in the case of the $S_w=65$ cm^2 window arise because the transmittance of the window is in reality lower than the geometric value, the electrons in the beam propagating in the gas scatter, and part of the beam and secondary emission reflect from the collector surface.

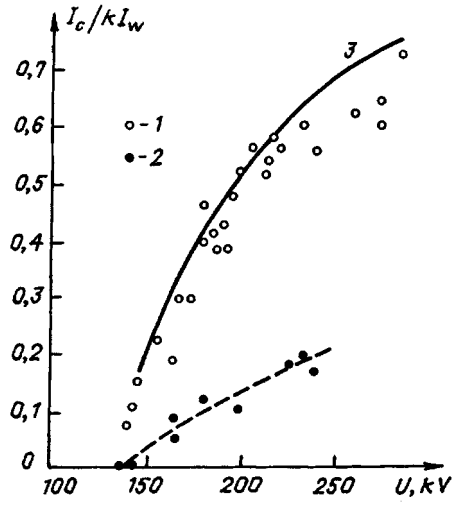

FIG. 2. Values of I_c/kI_w, obtained with 350 cm^2 (*1*) and 65 cm^2 (*2*) windows, and transmittance of a 50 μm thick titanium foil in terms of the number of particles (*3*) as a function of voltage applied to the diode according to the data of Ref. 7.

In summary, it has been demonstrated that the high-voltage stage of a discharge in an explosive-emission diode at gas pressures $\sim10^{-2}-10^{-1}$ torr can be protracted. It was shown that in the high-voltage stage the electron current is transported by an electron beam. The energy of the electrons in the beam is determined by the voltage applied to the diode, just as in the case of background-gas pressure $\sim10^{-4}-10^{-5}$ torr.

[1] Y. A. Kotov, G. A. Mesyats, S. R. Korzhenevskii, V. A. Motovilov, S. N. Rukin, V. A. Scotnikov, and A. L. Filatov, in *Abstract Book of the 10th IEEE Intern. Pulsed Power Conf.*, Albuquerque, New Mexico, 1995, pp. 2–70.

[2] N. S. Ivanova and K. N. Ul'yanov, Radiotekh. i élektron., No. 9, 1920 (1972).

[3] I. N. Shevtsova and Yu. E. Kreĭndel', Izv. Vyssh. Uchebn. Zaved. Fiz. **11**, 65 (1976).

[4] M. A. Zav'yalov, Élektronnaya obrabotka materialov, No. 4(46), 56 (1972).

[5] E. N. Abdullin, G. P. Bazhenov, S. M. Chesnokov *et al.*, in *Proc. 16th Intern. Symp. on Discharges and Electrical Insulation in Vacuum*, Moscow, St. Petersburg, 1994, p. 239–242.

[6] É. N. Abdullin, G. P. Bazhenov, S. M. Chesnokov, G. P. Erokhin *et al.*, Izv. Vyssh. Uchebn. Zaved. Fiz. **3**, 83 (1994).

[7] V. B. Nikolaev, Zh. Tekh. Fiz. **46**, 1555 (1976) [Sov. Phys. Tech. Phys. **21**, 891 (1976)].

Translated by M. E. Alferieff
Edited by David L. Book